Hauptreferent:
Prof. Dr.-Ing. U. Nackenhorst

Korreferent:

Prof. Dr.-Ing. Rolf Lammering
Prof. Dr. F. Renz

Doktorand:
M.Sc. Seyedalireza Shirazibeheshtiha

Computational simulation of piezo-electrically stimulated bone adaption surrounding activated teeth implants

Von der Fakultät für
Bauingenieurwesen
und Geodäsie der
Gottfried Wilhelm Leibniz
Universität Hannover

zur Erlangung des Grades
eines

Doktor-Ingenieurs

genehmigte Dissertation von

M.Sc. Seyedalireza Shirazibeheshtiha

Hannover 2016

Tag der Einreichung:
04.10.2016
Tag der mündl. Prüfung:
16.12.2016

**Institut für
Baumechanik
und Numerische
Mechanik**

Herausgeber:
Prof. Dr.-Ing. U. Nackenhorst

Verwaltung:
Institut für Baumechanik
und Numerische Mechanik
Gottfried Wilhelm Leibniz
Universität Hannover
Appelstr. 9A
30167 Hannover
Tel.: +49 (0)511 / 762-3219
Fax.: +49 (0)511 / 762-19053

Institut für Baumechanik
und Numerische Mechanik
Gottfried Wilhelm Leibniz
Universität Hannover
Appelstr. 9A
30167 Hannover

ISBN 978-3-935732-43-7

Abstract

With artificial teeth implants the mechanical stimulation of the jawbone is reversed because the natural ligament fixation of teeth is destroyed. This study aims for the development of active implants which provide additional electrical stimulation for bone adaption. A computational framework is presented in order to optimize new developments for activating dental implants with piezoelectric coatings. An electromechanical driven bone remodeling theory is developed and implemented into a finite element program. The osseointegration of bone implants is simulated by means of bio-active interface theory. Detailed numerical studies are performed based on a 3D model of lower mandible which has been reconstructed from high resolution CT-data. Initial relative motion, called micromotion, is limited as an important parameter for the osseointegration because excessive micromotion causes apposition of fibrous tissue.

A modeling approach is introduced considering both electrically and mechanically stimulated time dependent ingrowths with regard to simultaneous assessment of the micromotion threshold violation under dynamic chewing loads. In this context, the combined Drucker-Prager with von Mises yield criterion is introduced for the simulation of osseointegration process based on robust and established methods of plasticity theory. The linear theory of piezoelasticity is implemented into the finite element program for coupled electro-mechanical modeling.

Furthermore, the influence of an additional piezoelectric coating of the implant is investigated. In this case, the electric field strength produced by piezoelectric coating due to normal chewing conditions is of significant importance, as rather low field intensity doesn't affect on bone cell proliferation while quite excessive fields might cause cell necrosis. Therefore, a parametric study has been carried out in order to achieve suitable material properties of piezoelectric coating to provide an electric field in tolerable domain. With these results conclusions can be made on the goal oriented electromechanical stimulation to accelerate bone formation and enhance faster healing after surgery.

Keywords Osseointegration, Electromechanical stimulation, Micromotion, Dental implants, Finite element simulation.

Kurzfassung

Beim Einsatz künstlicher Zahnimplantate wird die mechanische Stimulation des Kieferknochens invertiert, weil die natürliche Ligamentfixierung der Zähne zerstört ist. Diese Studie zielt auf die Entwicklung aktiver Implantate ab, die zusätzliche elektrische Stimulation für den Knochenaufbau bieten. Es wird eine theoritische Ausarbeitung präsentiert, um neue Entwicklungen für aktivierende Zahnimplantate mit einer piezoelektrischen Beschichtung vorzustellen. Eine elektomechanisch getriebene Knochenumbau-Therorie wurde entwickelt und in ein Finite Element Programm implementiert. Die Osseointegration von Knochenimplantaten wird in einer bioaktiven Interface-Schicht simuliert. Detaillierte Studien werden auf der Basis eines 3D-Modells des Unterkiefers durchgeführt, das aus hochaufgelösten CT-Bilddaten rekonstruiert wurde. Relative Bewegungen, auch Micromotion genannt, sind in begrenzender Faktor für den Osseointegration, denn übermäßige Micromotion verursacht Apposition von Knochengewebe.

Es wird ein Modell vorstellt, das mit elektrischer und mechanischer Stimulation zeitabhängiges Einwachsen unter Berücksichtigung einer gleichzeitige Bewertung der Micromotions-Schwellenwert unter dynamischen Kaubewegungen simuliert. Für die Osseointegration wird in Anlehnung an die Plastizitätstheorie ein Drucker-Prager-Modell für das bioaktive Interface angenommen, das in Abhängigkeit vom Ossifikationsgrad in ein von Mises Modell übergeht. Somit wird ausgehend von reibungsbehafteten Normalkontakt eine feste Verbindung zwischen Implantat und Knochen hergestellt.

Weiterführende Studien werden zum Einfluss der piezoelektrischen Beschichtung des Implantats durchgeführt. Ist die elektrische Feldstärke, die durch piezoelektrische Beschichtung beim normalen Kauprozess erzeugt wird, zu geringe, haben diese keinen Effekt auf den Knochenaufbau, während zu hohe Feldstärken Zellnekrose verursachen könnten. Dafür wurde eine parametrische Studie durchgeführt, um geeignete Materialeigenschaften von piezoelektrischen Materialien zu finden, die ein elektrisches Feld in tolerierbaren Größenordnungen zu erzeugen. Mit diesen Resultaten können Schlussforderungen für zielorientierte elektomechanische Stimulation gezogen werden, um die Knochenbildung zu beschleunigen und einen Heilungsprozess nach Operationen zu verbessern.

Stichworte: Finite-Elemente-Methode; Knochenumbau; Osseointegration; Zahnimplantate; Elektromechanische Stimulation; Knochen-Implantat-Interface.

To my lovely parents.

Acknowledgments

This research was performed at the Institute of Mechanics and Computational Mechanics (Institut für Baumechanik und Numerische Mechanik - IBNM) at Leibniz Universität Hannover (LUH). I was also member of MARIO (Multifunctional Active and Reactive Interfaces and Surfaces) group which is a doctoral program at Leibniz Universität Hannover in close cooperation with the Hannover Medical School (Medizinische Hochschule Hannover) and the University of Applied Sciences in Hannover (Hochschule Hannover).

First of all, I would like to express my special appreciation and sincere gratitude to my advisor Prof. Dr.-Ing. Udo Nackenhorst for the continuous support, helpful guidance and for allowing me to grow as a research scientist by giving me this opportunity to participate in the MARIO doctoral program. It has been an honorable and educational experience working under his supervision during my research.

I would like to thank my second advisor Prof. Dr. Franz Renz for their insightful comments and briliant suggestions, which encourage me to widen my research from various perspectives.

Thanks are also extended to all the members of the MARIO who starring in so many memories about the inspiring workshops in Dresden and International House Sonnenberg located in Harz Mountains. I thank Meisam for scientific discussing when I struggled with my work who gave me required solution. I like to thank the IBNM-team for the scientific collaboration during my research. Appreciation is also expressed to IKM-team, which I was a unofficial member of IKM family, particularly IKM soccer players who make a great memory that I can have forever. I really appreciate Daniel and Antje for supporting me in all technical problems. The biggest gratitude goes to Alena and Dorit for all kindly support with administrative issues.

In the end, special recognition goes out to my family, for all their love, support and encouragement during my pursuit of the Doctorate in Educational Leadership.

Hannover, January 2017 Alireza Shirazi Beheshtiha

Contents

List of Figures III

List of Tables V

List of Symbols and Abbreviations IX

1 Introduction 1
- 1.1 Motivation . . . 1
- 1.2 State of the Art . . . 2
- 1.3 Aims and Scope . . . 4

2 Basic and Applied Bone Biology 7
- 2.1 Jawbone Anatomy . . . 7
- 2.2 Bone Biology . . . 8
  - 2.2.1 Electrical Properties of Bone . . . 10
- 2.3 Bone Remodeling . . . 13
- 2.4 Dental Implant Osseointegration . . . 14

3 Fundamentals of Continuum Mechanics and Electrostatics 19
- 3.1 Kinematics . . . 20
- 3.2 Electrostatics . . . 23
- 3.3 Stresses and Electric Displacements . . . 25
  - 3.3.1 Stress Measures . . . 25
  - 3.3.2 The Electric Displacement . . . 25
- 3.4 Balance Laws . . . 26
  - 3.4.1 Conservation of Mass . . . 27
  - 3.4.2 Conservation of Linear and Angular Momentum . . . 28
  - 3.4.3 Conservation of Electric Charge . . . 29
  - 3.4.4 Conservation of Energy . . . 29
  - 3.4.5 The Second Law of Thermodynamics . . . 30
- 3.5 Constitutive Theory . . . 31
  - 3.5.1 Constitutive Description of Bone Remodeling . . . 32
  - 3.5.2 Osseointegration at the Bone-dental Implant Interface . 38

3.6 Phenomenological Behavior of Piezoelectric Materials 42
3.6.1 Piezoelectric Effects 44
3.7 Piezoelectric Constitutive Equations 46

4 Finite Element Modeling of Electro-Mechanical Coupling 51
4.1 Variational Principles 51
4.2 Finite Element Discretization 52
4.3 Finite Element Solution 55
4.4 The Case of Nonlinear Constitutive Relations 56
4.5 Verification of Coupled Electro-Mechanical Model 57
4.5.1 Sensor 57
4.5.2 Actuator 59

5 Finite Element Modeling of Teeth Implants 61
5.1 Segmentation 61
5.2 Reconstruction of Surface and CAD Models 62
5.3 Finite Element Models 63
5.4 Projection of CT Intensities to the Finite Element Model . . . 64
5.5 Boundary Conditions and Simulation Approach 65

6 Numerical Studies on Implant Osseointegration 67
6.1 Electromechanically Stimulated Osseointegration 67
6.1.1 Electrical Properties of Bone tissue 67
6.1.2 Micromotion Limit 68
6.1.3 Additional Piezoelectric Coating 70
6.2 Parametric Study 71

7 Conclusion and Future Research 77

References 79

Curriculum Vitae 89

Forschungs- und Seminarberichte 91

List of Figures

2.1 Basic anatomy of the mandible, adapted from Medscape Mandibular Fracture Imaging [1]. 8
2.2 Schematic diagram from a portion of long bone, de Pepp [2011]. 9
2.3 Schematic diagram from the structural concept, Rho et al. [1998]. 10
2.4 Strain generated potential (SGP) phenomenon on a femur under mechanical loading, Olsson [2005]. 11
2.5 Schematics of different electrical stimulation techniques: a) Direct current (DC), b) Capacitive coupling (CC) and c) Inductive coupling (IC), Aaron RK. [1991]. 12
2.6 The main parts of dental implant, adapted from The Dental Implant Experts [2]. 15

3.1 Reference and current configuration of a continuum body. . . . 20
3.2 Transformation of line, area and volume elements. 22
3.3 Charged particle in an electrical field of two point charges. . . . 24
3.4 Comparison of different constitutive models E_M, E_{CH}, E_A and E_L for bone modulus of elasticity with respect to the density, Lutz and Nackenhorst [2011]. 35
3.5 Bone density as a function of the relative permittivity (a), relative permittivity (dimensionless) as a function of frequency for various densities of bone tissue (b) (FC: Femoral head; FMC: femoral medial condyle, FLC: femoral lateral condyle and FTM: femoral greater trochanter.), Sierpowska et al. [2003]. 37
3.6 Illustration of Drucker-Prager yield surface converts into von Mises model: (a) principal stress space and (b) deviatoric planes. 40
3.7 Crystal structure of perovskite: no piezoelectric effect ($T > T_C$), piezoelectric effect ($T < T_C$). 43
3.8 (a) Random polar domain, (b) aligned polarization direction under DC electric field, (c) removed electric field and locked dipoles. 44
3.9 Reaction of a poled piezoelectric element under compression and tension. 45

3.10 Butterfly-shaped curves of the strain-electric-field diagram of piezoelectric material 45

4.1 Sensor: a) Constant strain field $\boldsymbol{\varepsilon}_{11}$ b) Constant electric field E_3 c) Linear displacement d) Linear electrical potential difference. 58
4.2 Actuator: a) Constant strain field $\boldsymbol{\varepsilon}_{11}$, b) Constant electric field E_3, c) Linear displacement d) Linear electrical potential difference. 60

5.1 Model generation from CT-data (a), 3D thresholding a skull data set (b). 62
5.2 a) View of the total mandible, green color part represents the left half of mandible, b) CAD model of mandible, c) CAD model of the implant, d) The implant is placed virtually into the mandible model 63
5.3 Finite element model: implant (a), piezoelectric coating (b), bio-active interface layer (c) and mandible (d). 64
5.4 a) Time dependent loading for normal chewing b) loading components in coronal-apical, lingual-buccal and mesial-distal directions. 66

6.1 Electromechanical stimulation on the osseointegration prediction in the interface with 100 μm micromotion threshold from timesteps 1 (a), 3 (b), 5 (c), 7 (d) and (e) 10. 69
6.2 Comparison of a) electromechanical and b) mechanical stimulation on the osseointegration prediction in the interface with 100 μm micromotion threshold from timesteps 1, 5 and 10 (left to right). 69
6.3 Final state of the osseointegration prediction considering electromechanical stimulation with 50, 75 and 100 μm micromotion threshold (left to right). 70
6.4 The osseointegration prediction considering additional piezoelectric layer with 100 μm micromotion threshold from timesteps 1 (a), 3 (b), 5 (c), 7 (d) and (e) 10. 71
6.5 Dimensionless induced electrical field in dependecy of e_{33} ($E_{ref} = 10^{-8}\ V/mm$) 72
6.6 Comparison of evolution of density in bio-active interface with pure mechanical stimulation, electrical properties of bone tissue and additional PVDF layer from timesteps 1 to 10. 73
6.7 Mean (a) and maximum (b) value of Von Mises stress for Bio-active interface, mandible bone and PVDF layer from timesteps 1 to 10. 74
6.8 The mean value of strain and electric energy density of bio-active interface layer from timesteps 1 to 10. 75

6.9 Electric potential distribution in PVDF layer from timesteps 1 to 10. 75
6.10 Mean value of electrical field in PVDF layer from timesteps 1 to 10. 76

List of Tables

3.1 Mean square error between the simulation and experimental results, Lutz and Nackenhorst [2011]. 36

4.1 Mechanical and electrical properties of piezoelectric body . . . 57
4.2 Sensor: Comparison of analytical and numerical results. 59
4.3 Actuator: Comparison of analytical and numerical results. . . . 59

5.1 Material parameters for different parts of the jawbone-implant intractive system 65

6.1 Electrical characteristics of Bio-active interface and PVDF film 68

List of Symbols and Abbreviations

$\mathcal{B}$	Continuum body
t	Time
B_0	Continuum body in reference configuration
B_t	Continuum body in current configuration
$\boldsymbol{U}$	Displacement fields
$\boldsymbol{F}$	Deformation gradient
J	Volume ratio
$\boldsymbol{E}$	Green-Lagrange strain tensor
$\boldsymbol{C}$	Cauchy-Green deformation tensor
$\boldsymbol{\varepsilon}$	Linear strain tensor
$\boldsymbol{F}_c$	Electrostatic force
E	Electrical field strength
Q	Electric charge
ϕ	Electric potential
ϕ_t	Electric potential in the current configuration
$\boldsymbol{t}$	Cauchy stress vector
$\mathrm{d}\boldsymbol{f}$	Traction vector
$\boldsymbol{n}$	Normal vector
$\boldsymbol{T}$	First Piola-Kirchhoff traction vector
$\mathrm{d}\boldsymbol{A}$	Infinitesimal surface element of reference configuration

$\mathrm{d}\boldsymbol{V}$	Infinitesimal volume element of reference configuration
$\mathrm{d}\boldsymbol{a}$	Infinitesimal surface element of current configuration
$\boldsymbol{P}$	Nominal stress
$\boldsymbol{\sigma}$	True stress
$\boldsymbol{D}$	Electric displacement field
P	Polarization density
χ	Electric susceptibility
ε	Electric permittivity
$\boldsymbol{\Psi}$	Electric flux
$\boldsymbol{Z}$	Physical field
Ξ_f	Volumetric flow
Ξ_p	Volumetric production
Λ	Surface flow
ρ	Density
ρ_0^{el}	Electric charge density
m	Mass
$\boldsymbol{L}$	Linear momentum vector
$\boldsymbol{f}^{el}$	Electromagnetically induced volume forces
$\boldsymbol{t}$	Stress vector
$\boldsymbol{x}$	Position vector
$\dot{\boldsymbol{x}}$	Velocity vector
$\ddot{\boldsymbol{x}}$	Acceleration vector
$\boldsymbol{b}$	Body force
$\boldsymbol{J}$	Angular momentum
$\boldsymbol{\sigma}$	Cauchy stress tensor
$\boldsymbol{I}$	Electric current
$\boldsymbol{J}_0^{el}$	Current density

$\mathcal{U}$	Internal energy
$\mathcal{K}$	Kinetic energy
$\mathcal{W}$	External forces
$\mathcal{Q}$	Heat supply
u	Specific internal energy
r	Specific internal heat source
q	Heat flux over the boundaries
$\mathcal{S}$	Entropy
ψ	Free Helmholtz energy
ψ_{mech}	Strain energy density
ψ_{elec}	Electric energy density
ψ_{ref_m}	Physiological target values for the strain energy density
ψ_{ref_e}	Physiological target values for the electric energy density
D^{bio}	Dissipation of biomechanics
$\mathbb{C}(\rho)$	Isotropic linear elastic tensor depends on local bone mineral density
$\mathbb{C}_0$	Linear elastic tensor
$\tilde{\sigma}$	Deviatoric part of stress tensor
c	Adhesion parameter
α	Friction coefficient
p	Hydrostatic pressure
σ_F	Solids yield strength
ξ	Osseointegration variable
ρ_{min}	Minimum value of bone mineral density
ρ_{max}	Maximum value of bone mineral density
ν	Poisson's ratio
λ	Plastic multiplier
n	Flow direction

μ	Shear modulus
$\tilde{\mathbb{C}}_{vM}^{ep}$	Von Mises elasto-plastic tangent
T_c	Curie temperature
e	Piezoelectric stress constant
N_I	Shape functions
$\boldsymbol{B}_u$	Derivatives of the shape functions for the mechanical displacements
$\boldsymbol{B}_\phi$	Derivatives of the shape functions for the electric potentials
$\boldsymbol{K}_{uu}$	Global elastic stiffness matrix
$\boldsymbol{K}_{u\phi}$	Direct piezoelectric stiffness matrix
$\boldsymbol{K}_{\phi u}$	Converse piezoelectric stiffness matrix
$\boldsymbol{K}_{\phi\phi}$	Global dielectric stiffness matrix
$\boldsymbol{F}_{ext}$	Global nodal force loading vector
$\boldsymbol{Q}_{ext}$	Surface density charge vector
PVDF	Polyvinylidene fluoride
ECM	Extracellular matrix
BMU	Basic multicellular units
HA	Hydroxyapatite
SGP	Stress generated potential
SED	Strain energy density
CDM	Continuum damage mechanics
NURBS	Non-Unifom Rational B-Splines
FEA	Finite Element Analysis

1 Introduction

1.1 Motivation

In orthodontology, dental implants are introduced as artificial replacements of natural teeth which are surgically placed into the jawbone. Since the 1960s, titanium prostheses are commonly used for many biomechanical applications including dentistry because of its biocompatible properties. Aseptic loosening of implant can occur 10 to 20 years after replacement surgery because of poor quantity and quality of bone surrounding dental prosthesis. In order to prevent implant failure, finding out the answer of these two questions is crucial: (1) how is the bone connected to implant?, and (2) how is the structure of the bone remodeled?. Therefore, surgeons and implant manufacturers are researching to develop an effective assessment and prediction protocol in order to reach more compatible implant systems.

For the first time, Fukada and Yasuda [1957] have demonstrated that bone exhibits piezoelectric behavior. Bone tissues are nanocomposites of collagen fibrils reinforced by the mineral crystals (mainly hydroxyapatite) that exhibit bioelectrogenic properties such as piezoelectricity and electrokinetic potentials. These electrical properties depend on age, gender and anatomical location. This phenomenon occurs by producing gradients in electrical potentials called stress generated potential (SGP) along the collagen fibrils following the mechanical deformation of the tissue, which provides a local stimulus for bone-generating cell proliferation.

In recent years, the advantage of using electrostimulation techniques, particularly for the healing of bone fracture, cartilage and ligament diseases, have been investigated in order to identify the electrical attributes of biological tissue. Despite the fact that electrical stimulation can enhance bone formation a technical solution on using electricity for bone formation in a controlled manner remains still complicated. Electrical stimulation has been investigated widely in different animal and clinical studies.

This research is based on the hypothesis, that dental implants with piezoelectric coatings could be beneficial for their osseointegration. Useful electrical energy can be produced during normal physiological activity using piezoelec-

tric materials within orthopedic implants. In order to achieve an optimized implant design, the role of primal osseointegration is under discussion. After insertion of an implant, stromal bone marrow stem cells initiate a stable and long-lasting connection between the bone and the implant, a process called osseointegration. Initial relative motion, called micromotion, must be limited as an important parameter for the stimulation of osseointegration, because excessive micromotion causes apposition of fibrous tissue.

Finite element analysis (FEA) is used extensively in various fields of medical applications such as predicting bone loss and ingrowth surrounding dental implants. Most FEA models assume a perfect bonding between bone and implant, while this does not take place identically in clinical conditions. Thus, an imperfect interface layer between bone and implant need to be modelled. Therefore, mathematical and computational modeling approaches for the prediction of osseointegration process are necessary. The numerical studies allow to quantify the improvement of bone formation in the presence of electrical stimulation.

1.2 State of the Art

Computational modeling approach and simulation of dental prosthesis in order to achieve better biocompatibility of the material and stability inside of the jawbone have been increasingly addressed by research groups in the past decades. Bones are living tissues that are capable to adapt their internal structure to the mechanical demand. This statement is known as the Wolff's law, Wolff [1892]. Bone remodeling theories have been developed to predict bone growth from internal mechanical loads in terms of stress and strain, e.g. Frost [1988]; Pauwels [1965]; Kummer [1972]; Cowin [1986]; Cowin and Hegedus [1976]; Cowin and Nachlinger [1978]; Hegedus and Cowin [1975]. Since a couple of years sophisticated studies have been carried out for the constitutive modeling of stress adaptive bone remodeling phenomena considering anisotropic behavior of bone as well as large deformation theory which can be found in e.g. Jacobs et al. [1997]; Krstin et al. [2000]; Doblaré and García [2002]. Furthermore, the effects of initial cellular remodeling units (BMU, Basic multicellular units) during tissue replacement was investigated by Martin [2007] and Hernandez et al. [1999].

With this significant advances in bone remodeling theories, investigations of other biophysical stimuli which can affect this process remains under controversy discussions. Most mathematical models have not taken account of the multiphysics phenomena of bone tissue. Ramtani [2008] established a new mathematical model considering piezoelectric and electrokinetic behavior of the bone. Qu and Yu [2011] developed a mathematical model (one spatial dimension) of the remodeling process under the influence of both mechanical

loads and electric charges.

Clinical studies demonstrated that the piezoelectric behavior of bone tissues produce electric potentials, see Aschero et al. [1996]; Beck et al. [1997]; Gross and Williams [1982]; Johnson et al. [1982]. Piezoelectricity is a fundamental characteristic of bone which can raise great interest in understanding bone physiology. In the following, electrical stimulation has been studied to improve fast and stable bony ingrowth and to reduce the time of healing process after bone surgery which can be found in Park and Kenner [1975]; Park et al. [1978]; Salman et al. [1978]; Weinstein et al. [1976]. Giannunzio et al. [2008] and Shayesteh et al. [2007] investigated the effect of electrical stimulation on healing processes specifically for bone-dental implants. However, an open question still remains on how exactly an electrical stimulus affects the biological entities.

To date, three main theories have been suggested for electrical stimulation of bone tissue using: i) electric current ii) electromagnetic field and iii) electric field. In electric current stimulation through direct contact the magnitude of constant current is important for the osteogenesis effect. Brighton et al. [1981] reported that currents less than 5 μA and greater than 20 μA indicated no effect and cell necrosis, respectively. In addition, electric current with direct contact electrodes is not a viable method, since electrodes inside the body are a source for infections and other long term problems. Therefore, the weakness of this method lead to the investigation of alternative, non-invasive methods. The study of Brighton et al. [1992] revealed that the electric field intensity is a considerable parameter in bone cells proliferation. They observed that an electric field strength of 0.1-10 mV/cm enhances the cell proliferation while fields less than 0.1 mV/cm did not affect the proliferation.

Some studies have focused on using electrically charged materials and piezoelectric materials as artificial bone grafts. Callegari and Belangero [2004] demonstrated that the piezoelectric polyvinylidene fluoride (PVDF) tube can improve new bone formation when it was implanted into an artificial defect of a rat femur. Basic knowledge on that subject has been obtained from experimental investigations, mathematical models and computational simulations, see Ambard and Swider [2006] and Moreo et al. [2009]. However, mathematical models that justify bone remodeling based on bone piezoelectricity are rather sparse, Qin and Ye [2004a]; Qu et al. [2006]; Ramtani [2008].

Bone healing at the interface of bone and implant is a complex biological process which is roughly partitioned in four subsequent steps. The process initiates with bleeding as a consequence of the implant insertion for couple of hours (stage 1). Bleeding is reduced by formation of fibrillated structures which detains blood loss during several days (stage 2), Polimeni et al. [2006]; Davies [2003]. Bone cells start to move towards the injured zone over a period

of some weeks (stage 3), Davies [2003]. Finally, bone cells start the formation of a new bone matrix for several months (stage 4). The process of osseointegration and stress shielding have to be distinguished, as they happen at different time scales. Stress shielding refers to the reduction in bone density because of the strong implant the surrounding bone is not stressed in a physiological manner, see Weinans et al. [1992]. The stress shielding process takes place in the late stage 4, while the process of osseointegration happens at stage 3.

A sufficient osseointegration describes the acceptance of the prosthesis by bone tissue which depends on several parameters, as mentioned in Albrektsson and Johansson [2001]. One of the most important issues is the initial relative motion in the gap between the bone and implant, referred to as micromotion. Pilliar et al. [1986] reported that bony ingrowth has been attained at 28 μm micromotion, whereas a formation of strong fibrous tissue was achieved at micromotions of 150 μm one year after. To this date a specific threshold on micromotion for the osseointegration remains unknown. Szmukler-Moncler et al. [1998] concluded that the micromotion threshold for osseointegration can be somewhere between 50 and 150 μm.

Since a couple of years computational simulation of mechanical conditions in the bone-implant interface is an open field of research. Papavasiliou et al. [1997] investigated the stability of dental implant and determined degrees of osseointegration using an interface layer approach. A multi-scale computational approach has been introduced for the optimization of teeth implant coatings by Rungsiyakull et al. [2010]. They compared osseointegration and bone remodeling on the micro-scale using a model with discrete coating pores. Lutz and Nackenhorst [2011] introduced a new model refinement in terms of bioactive interface theory in order to simulate osseointegration in rough coated non-cemented hip-joint implants. In the aforementioned work, the initial constitutive behavior of bone-implant interface layer was introduced by a Drucker-Prager like plasticity model and the osseointegration process has been considered by an artificial hardening rule.

In conclusion of this quite brief review, besides introducing electrical properties of bone tissue and electrostimulation techniques, computational modeling approaches for the prediction of osseointegration processes of bone-implants have been summarized. In the majority of previous publications mainly static loading and mechanically stimulated ingrowth behavior have been studied. This gives rise to much further research on electro-mechanical stimulation of bone matrix under dynamic loads.

1.3 Aims and Scope

In this work, an effective approach for the numerical simulation of dental implants is presented, which can be applied to other types of medical implants.

The simplicity of the isotropic model bone remodeling is intentionally considered in order to reduce the parameters which are under investigation. Many advanced models have the disadvantage that they require a lot of unknown parameters which are neither measurable nor somehow clinically applicable. The finite element studies show that the differences between isotropic and orthotropic modeling differ significantly only in few number of bones models from one system in the continuum mechanics.

This by begins with the geometric modeling. Here methods are presented which patient-specific finite element models can be created from computer tomography data. The boundary conditions for the finite element simulation are discussed in detail. This aspect plays an important role for practical applications which is neglected in many work in this area. In this context, the adaptive bone remodeling is investigated under the influence of both electrical and mechanical stimulation. The method presented for the calculation of the equivalent dynamic load collectives is computationally efficient. Along with the highly efficient implementation a considerable computational speed advantage is gained thereby. The osseointegration simulation approach is developed which can describe and predict the effect of electrical stimulation on bone-implant interface. The proposed methods can be applied to clinical problems based on clinical trial data.

In this work, computational simulation has been carried out in order to evaluate the influence of electro-mechanical stimulation on the ingrowth behaviour in bio-active interface layer. Thus, electro-mechanical bone remodeling theory has been combined with a Drucker-Prager interface model considering electro-mechanical behavior of the interface. A soft, thin bone-implant interface layer has been modeled in order to simulate osseointegration, consisting of a mixture of liquid phase and bony fragments which appears immediately after the surgery. This layer has the ability to adopt electrical properties of bone cells for electro-mechanical stimulation. Furthermore, additional piezoelectric coating was modeled surrounding dental implants which provide a surface electrical charge in order to electrical interactions with the physiological environment.

The main objective of this work is to evaluate the feasibility of using piezoelectric coating (PVDF) to generate in vivo electrical energy surrounding dental implants. In this study, a modeling approach considering both electrically and mechanically stimulated time dependent ingrowth with regard to simultaneous assessment of the micromotion threshold violation under dynamic chewing loads is investigated. A solid interface element with bio-active constitutive properties is utilized for modeling the bone-implant interface incorporating piezoelastic characteristics. The derived equations of piezoelectric material are solved using finite element methods in order to simulate a thin piezoelectric layer surrounding a dental implant. A three dimensional finite element model of the lower mandible is reconstructed from a CT data set of a 63 years

old male patient using segmentation techniques.

The present thesis is composed of six chapters, including this introduction and a further chapter dedicated to conclusions and future work.

The bone biology and medical applications are provided in chapter two, which are necessary to understand this work. This chapter provides a brief description about biomechanics of bone tissue, electrical properties of bone cells, bone remodeling and osseointegration process.

Chapter three contains the theoretical foundations that are necessary for modeling in the context of continuum mechanics. A brief review of the fundamental concepts of continuum mechanics is given in this chapter. Starting with the kinematics of an arbitrary deformation process and electrostatics laws. A description of stress measures and the electric displacement follows. Then the balance equations within each kinematic framework are introduced. The developed interface model for the description of the mechanically regulated osseointegration is presented based on established methods of continuum plasticity theory. Afterwards, a brief and basic information about crystalline structure of piezoelectric materials such as piezoelectric effects are given based on mechanical loading and polarization direction. The constitutive equations for isotropic materials are outlined. In the end, linear theory of piezoelectricity used for coupled electromechanical modeling is presented.

Chapter four contains the numerical implementation in the finite element modeling. First, the basic concept of the finite element method is reviewed which is used in this work. Then the finite element discretization for the electrostatic and mechanical fields are introduced. In the following a piezoelastic patch test is investigated in order to verify numerical results.

A brief review on the procedure for the reconstruction of geometrical models from CT data is outlined in chapter five. In the following, projection of CT data to finite element model is reviewed. Finally, boundary conditions and simulation approach are presented.

The results of a comparative study are presented in chapter six, to evaluate the effect of electromechanical stimulation on implant osseointegration based on electrical properties of bone cells. In addition, the variation of micromotion limit is investigated as a remarkable factor which can affect on osseointegration. This is followed by a parametric study in order to achieve the best value of piezoelastic constants to provide the electric field in a tolerable domain.

2 Basic and Applied Bone Biology

Bone is a rigid connective tissue with complex anatomy that forms the skeleton of the body. From the structural aspect, bone is a dynamic structure which has ability for self-repair and responding to external mechanical forces with continuous remodeling. The bone remodeling is a natural life-long process that bone is renewed through the bone resorption and formation in interaction with mechanical environment.

In addition, bone is a source of electric potential when it is mechanically stressed or injured, which it has been demonstrated by Salzstein and Pollack [1987]; Friedenberg and Brighton [1966]; Friedenberg and Smith [1969]. Furthermore, bone formation and repair can be affected by electrical stimulation, see Basset and Becker [1964]; Brighton [1981]; Yonemori et al. [1996].

Hence, an understanding of biomechanical behavior of bone tissue in response to electrical and mechanical stimulations is necessary. The following chapter covers biology, anatomy and remodeling of bone.

2.1 Jawbone Anatomy

The mandible and maxilla are the largest and strongest bones in the face which hold the lower and upper teeth in place. The masticatory muscles provide the loads for chewing of food with repetitive cycles of opening and closing the space between the mandible and maxilla. The basic anatomy and function of the mandible is indicated in Fig. 2.1 for the purpose of the present research. The structure of mandible consists of the following area:

- Body, curved horizontal portion
- Ramus, positioned vertically at the rear of the mandible
- Angel formed at the junction of body and ramus
- Mental foramen, allows the entrance of the mental nerve and blood vessels into the mandibular canal

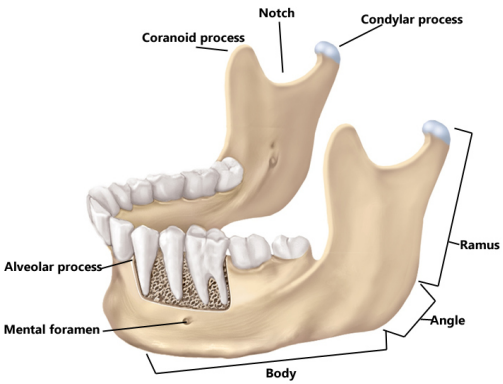

Figure 2.1: Basic anatomy of the mandible, adapted from Medscape Mandibular Fracture Imaging [1].

- Alveolar process, the tooth bearing area of the mandible which is located at the upper part of the body;
- Condyle, the upper part of the ramus which articulates with the temporomandibular joint in the temporal bone;
- Coronoid process, located above the ramus and the temporalis muscle attaches at this location.

2.2 Bone Biology

The major functions of bones are structural support for the body, transmission of muscle forces, protection of vital organs, to provide an environment for marrow (where blood cells are produced) and a storage area for minerals (such as calcium). Bone tissue consists of the bone cells, extracellular fluid and the solid extracellular material which is called the bone matrix. This bone matrix, which is surrounded by the extracellular fluid, is in contact with blood plasma. The plasma contains bone cells to regulate the chemical reactions which cause a change in the porosity of bone matrix. These cells, which are described in the following, are osteoblasts, osteoclasts and osteocytes.

Bones are generally classified in two types of tissue, cortical (compact) and cancellous (spongy). Cortical bone is a strong, dense and tough outer layer, which contributes to about 80% of the weight of a human skeleton. Cortical

[1] http://emedicine.medscape.com/article/391549-overview

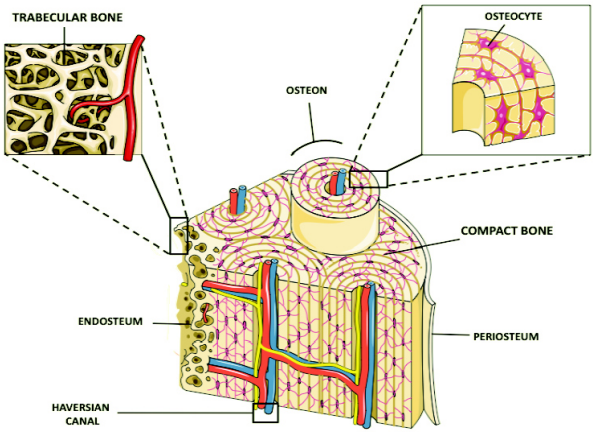

Figure 2.2: Schematic diagram from a portion of long bone, de Pepp [2011].

bone is made by cylindrical structures, the so called osteons, as illustrated in Fig. 2.2.

Haversian canals are located in the center of each osteon which contain blood and nerve vessels. Osteocytes are placed in between the lamellae which are responsible for nutrient supply and communication. Cancellous bone is a internal spongy layer which is lighter and less dense than compact bone, the so called trabecular. The spaces between the trabecular is occupied by bone marrow and blood vessels. The external and internal surfaces are coverd by periosteum and endosteum, respectively, Shore et al. [1998].

Three different types of bone cells can be categorized as osteoblasts, osteocytes and osteoclasts. These cells play fundamental roles in bone formation, maintenance, and remodelling. Bone extracellular matrix (ECM) is secreted and deposited by osteoblasts which are responsible for bone formation and manufacture of hormones. The ECM of mature bone tissue contain 30-40 % of organic matrix and 60-70 % (dry weight) of mineral substances. The organic material mainly includes collagen fibrils 85-90 % (type I) and inorganic material consists mainly of calcium phosphate crystals in the form of hydroxyapatite (HA).

Osteoclasts are responsible in the resorption of mineralized tissue by removing its mineralized matrix and breaking up the organic bone. Osteocytes are mature bone cells, generated from osteoblasts, which have been surrounded by bone matrix, Behari [2009].

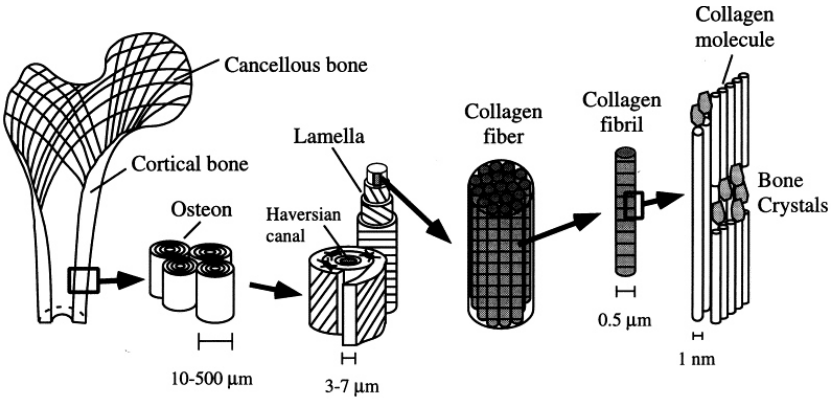

Figure 2.3: Schematic diagram from the structural concept, Rho et al. [1998].

As highlighted in the previous paragraph, bone has a complex and hierarchical structure with different physical and solid-state properties. In order to introduce a computational approach for the explanation of the mechanosensation and related adaption, identification of different length scales of bone is necessary. The hierarchical structure of bone makes the bone a highly anisotropic and inhomogeneous material. Under this circumstance, bone can be classified into five different length scales with particular mechanical properties. Only the macroscale is the focus of this thesis, as indicated in Fig. 2.3 (Rho et al. [1998]; An and Draughn [1999]).

- Macroscale, consisting of trabecular and cortical bone
- Microscale (10-500 μm), containing single osteons or trabeculae
- Sub-microscale (1-10 μm), lamellar level
- Nanoscale, including collagen fibril and mineral components of bone
- Sub-nanoscale, molecular level including collagen and non-collagen protein molecules and mineral crystals

2.2.1 Electrical Properties of Bone

Bone tissues are nanocomposites of collagen fibrils reinforced by the mineral crystals (mainly hydroxyapatite) reveal some special bioelectrogenic events such as piezoelectricity and electrokinetic potential. These electrical properties, which depend on age, gender, anatomical location and hydration (Singh and Saha [1984]), are strongly associated with applied mechanical loading

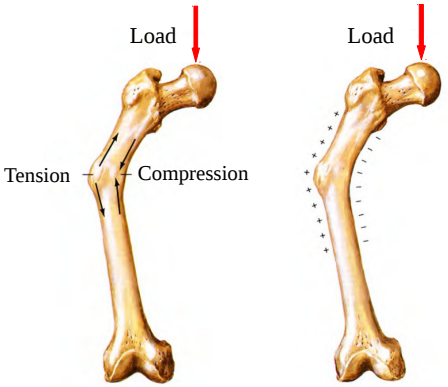

Figure 2.4: Strain generated potential (SGP) phenomenon on a femur under mechanical loading, Olsson [2005].

which can mediate the biological processes like bone remodeling. This leads to the idea that electrical signals can affect bone formation process.

This phenomenon occurs by producing electrical potential differences called stress generated potential (SGP) along the collagen fibrils following the mechanical deformation of the tissue which provides a local stimulus for bone-generating cells proliferation, Ahn and Grodzinsky [2009]. This indicates the close cooperation between bone cells and extracellular constituents. Behari [2009] and Ahn and Grodzinsky [2009] introduced two main mechanisms for stress generated potential in bone: piezoelectricity and streaming potential. However, some other researchers revealed that migration of inorganic ions within the bone cause induced electrical potential in bones, see Mycielska and Djamgoz [2004]; Theodore [1968].

The electric charge production in living and nonliving bone tissue are different and this latter mechanism act as a secondary origin of the electric generated potential in the living tissue, Ciombor and Aaron [2005]. The piezoelectric effect is the production of electric potential in bone while undergoing a mechanical deformation. This process is introduced as main factor for SGP in dry bone because of a displacement of the centre of symmetry in collagen fibrils structures.

The movement of positive and negative charges under mechanical deformation of bone is demonstrated in Fig. 2.4. When mechanical loads are applied on human femurs, electrical potential can be produced. The areas of bone that are compressed generate negative polarity and positive polarity is produced in tensed areas. Ramtani [2008] reported that electrical properties of bone not

only are considered as a hypothesised feedback mechanism for bone remodeling but also external electrical stimulation of bone can accelerate healing and repair process. The interest in using exogenous electrical stimulation to induce bone formation has arisen after observation the effect of endogenous electrical signals on bone growth and healing process. Therefore, understanding the piezoelectric behaviour of bone and its impact in bone remodelling is necessary.

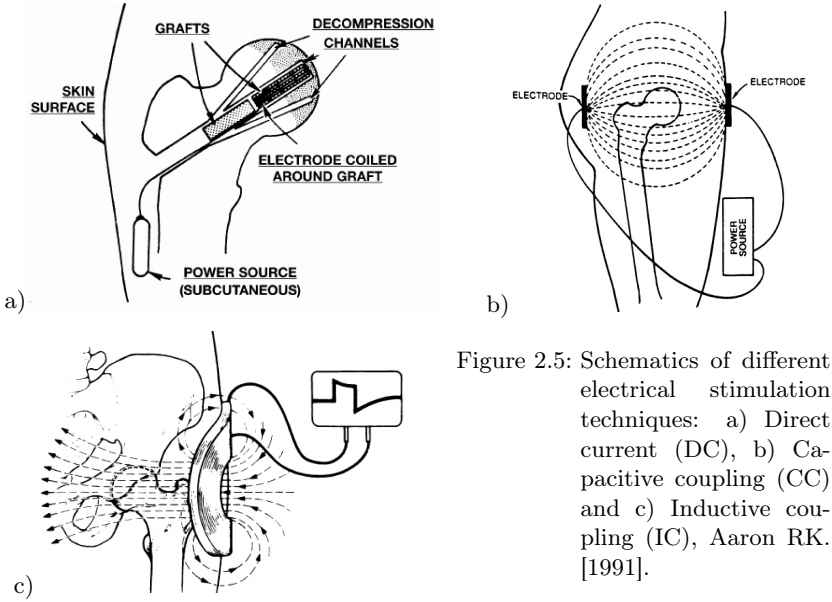

Figure 2.5: Schematics of different electrical stimulation techniques: a) Direct current (DC), b) Capacitive coupling (CC) and c) Inductive coupling (IC), Aaron RK. [1991].

Electrical stimulation techniques can be classified into three main groups. These three different techniques of bone stimulation with electric and electromagnetic fields are depicted in Fig. 2.5. First, an invasive method in where direct current (DC) is applied through surgically implanted electrods into the region of bone repair(Fig. 2.5 (a)). Song et al. [2009] developed such device inside of a dental implant to supply electrical stimulation for a canine mandibular bone. DC current generator can be implantable or external.

In a second method capacitive coupling (CC) is applied by means of electrods which are placed externally on opposite sides of the area to be stimulated (Fig. 2.5 (b)). In this method electric fields are produced noninvasively. Capacitive stimulation is more beneficial in comparison with DC stimulation

because it is non-invasive, and the effect of capacitive stimulation on bone formation is demonstrated for both vitro and vivo in Brighton et al. [2001]; Wang et al. [2001]; Brighton et al. [1985].

In a thirth noninvasive method, electrical fields are produced in bone by inductive coupling (IC) with an external time varying or pulsed electromagnetic field (PEMF), which is illustrated in Fig. 2.5 (c). Taking into account what has been known about electrical stimulation methods, improvements in healing process and bone growth can be obtained through different pathways, such as application of piezoelectric materials surrounding implants.

2.3 Bone Remodeling

Bone undergoes continuous reformation throughout lifetime and demonstrates regeneration properties after injury. Bone remodeling is the consequence of the complex interaction between osteoclasts and osteoblasts in order to bone resorption and deposition which is regulated with biochemical and biophysical stimuli, Fernandez-Tresguerres-Hernandez-Gil et al. [2006]. The process of remodeling not only take place for treatment of bone fractures, but also is essential for the maintenance of a normal healthy bone and adaptation to external stress and loading. Cortical and trabecular bone are renewed 5 and 20 % every year, respectively, Fernandez-Tresguerres-Hernandez-Gil et al. [2006]. The main cause leading to osteoporosis is unbalancing in bone formation/resorption activity. Many authors tried to propose mathematical models of bone remodeling process which is briefly introduced.

Bone remodeling simulations using numerical modeling are aimed on the prediction of the structure of bone and its development after some particular mathematical remodeling rules. Simulation of bone remodeling with phenomenological approaches within a continuum framework cannot model formation and resorption on a cellular level. However, analyzing such models helps to evaluate the stability and an optimising characteristics which affect on the remodelling process.

Cowin and Hegedus [1976] proposed the first continuous mathematical formulation of bone remodeling. The bone matrix was considered as a porous elastic solid surrounded by extracellular fluid. In this model, the theory of adaptive elasticity is introduced in order to describe the remodeling process of cortical bone. In this primarily theory it is assumed that the cortical bone tissue has a homeostatic strain state to which the rate of adaptation is related to the difference between the homeostatic and actual strain rates. This theory tries to explain the adaptive nature of the bone from one loading configuration to another.

The bone remodelling process is simulated by combination of mathematical

descriptions and finite element models (FEM) in order to assess the influence of local tissue response on the overall structure, see Fyhrie and Carter [1986]; Hart and Heiple [1984]. Most of these approaches are focused on local mechanical signal which can stimulate bone adaption process, Carter et al. [1987, 1989]. The influence of mechanical stimulation on bone density distribution has been predicted in a qualitative sense using the models developed so far.

After that, many authors attempt to develop more comprehensive models to reproduce the behavior of bone tissue. In these models, the mechanical behavior of the bone is determined using the aparent density. Huiskes et al. [1967] proposed strain energy density (SED)-based theory as the remodelling objective. The SED is described as strain energy function per unit volume at any region inside a stress field.

In recent years, the simulating of bone piezoelectricity which is related to mechanical environment is a common interest. In the subsequent theories corresponding to bone remodeling, only a limited number of studies have been undertaken to explore the effect of electromechanical stimulation on bone remodeling process. Qu and Yu [2011] and Demiray [1983] developed a mathematical models including the effect of electromagnetic fields on bone remodeling. Gjelsvik [1973a,b] attempts to numerically investigate the effect of electrical charges on bone formation and resorption in bone surfaces. Rebeca [2010] developed a numerical analysis based on a new bone remodeling model considering piezoelectric behavior of bone.

2.4 Dental Implant Osseointegration

The modern dental prosthesis is a biocompatible device, usually made of titanium, which act as a secure anchor for artificial replacement teeth to replace a missing tooth. Dental implants typically consist of three main parts which are depicted in Fig. 2.6. The conical screw shaped part is anchored into the jawbone as an artificial root of teeth, is called implant fixture. Abutment is placed over the conical part in order to connect the implant fixture and the crown. The crown is attached over the abutment which is made to look like a natural tooth.

Worldwide statistics indicate 95% success rate over a 5 years period if the implants are well designed, manufactured and inserted. The successful treatment rate reachs 90% after 15 years if appropriate and professinal care is taken. However, there are still several reasons that can cause implant failure. One of the main reasons is a lack of function of periodontal ligament (PDL). Since periodontal ligament is a soft tissue, it could be a supportive function to absorb the impact force and uniformly transfer the occlusal loads into the surrounding bone. This function is destroyed during the surgery which causes a non-uniform stress transfers in to the bone. This might induce biomechani-

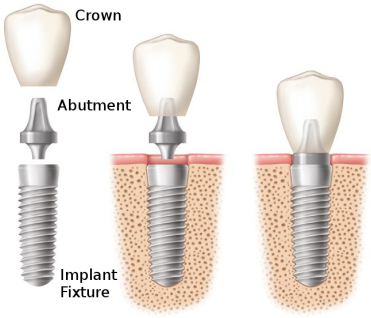

Figure 2.6: The main parts of dental implant, adapted from The Dental Implant Experts [2].

cal overloading failures in implant and bone, Rangert et al. [1995].

Hansson [2003] reported that overloading can cause the microdamage accumulation at bone and results in primary marginal bone loss. Consequently, the infection might occur in that region of bone loss and cause bone resorption. Therefore, the long-term success of a dental prosthesis strongly depends on the reliability and the stability of bone-implant interface. This interaction between bone and implant is initiated immediately after surgery. In order to reduce the number of implants failures, the healing process need to be fully understood.

The biological response in reference to fracture healing can be divided into primary and secondary healing, Einhorn [1998]. Primary healing encompasses a direct structural and functional connection between living bone tissue and implant surface which is called osseointegration. Secondary healing is the most common form of healing and occurs in the absence of optimal conditions needed for primary repair and includes the formation of callus. Bone remodeling phase takes place with proceeding healing process which makes months or years to complete biological reconstruction.

Since the success rate of implant remarkably depends on appropriate development of the bone-implant interface, characteristics of the implant surface play an important role in osseintegration process with early loading. Therefore, development of implant surfaces encouraged new considerations to improve bone formation at the implant surface.

The idea of using bio-active coatings surrounding implants has been developed in order to improve the initial bounding and primary implant stability. Coat-

ings including bioceramics, extracellular matrix proteins, biological peptides or growth factors can affect bioactivity and biocompatibility to the surface of orthopaedic prosthesis that promote bone ingrowth and enhance osseointegration of the implant. In addition, coatings such as silver, nitric oxide, antibiotics, antiseptics and antimicrobial peptides with anti-microbial properties can reduce bacterial adhesion and prosthetic infections. The most common bioactive ceramics are hydroxyapatite and certain compositions of glasses and glass ceramics.

More recently, new generation of biomaterials have been investigated to influence healing by mimicking the electrical properties in bone, Bystrov et al. [2014]. In this case, it is essential to explore the potential of piezoelectric coating for tissue regeneration. Hwang et al. [2002] investigated the effect of piezoelectric ceramics in vitro and in vivo on bone formation. Electrical field which is produced by piezoelectric coating not only might reduce or even eliminate the risk of implant slackening, but also the growth of bacterial biofilms on the tooth surface can be prevented. Jianqing et al. [1997] compared the effects of non-piezoelectric and piezoelectric ceramics on the new bone formation in the jawbone of dogs. Bone growth was observed surrounding implants with piezoelectric coating after one week, while after two weeks there was still no new formation of bone around of the non-piezoelectric implants.

Three most important criteria must be satisfied for designing and manufacturing process of these coatings. A first point which has to be considered is that the coating must be biocompatible. Secondly, it must promote osteoblasts (cells that produce bone) to adhere and grow on the surface of the implant to make a strong bond between bone and implant. Finally, the implant coating should be able to recruit stem cells from surrounding tissue and induce differentiation into osteogenic cells, Albrektsson and Johansson [2001]. In addition, the coating must have strong mechanical stability that can not be detached from the implant surface under physiological stresses.

Accurate and efficient modeling of osseointegration process at the bone-implant interface depends on various parameters such as geometry and surface structure of the implant, biomechanical properties of bone-implant interface and boundary conditions. A few number of mathematical models have been reported to introduce the mechanical environment at bone-implant interface. Büchler et al. [2003] established a computational approach on implant osseintegration considering a frictional interface model. They predicted bone ingrowth for an axisymmetric implant model considering local relative motion. Abdul-Kadir et al. [2008] constructed a finite element model to investigate primal implant stability based on contact mechanics approach considering a physiologically realistic loading.

[2]http://www.aaid-implant.org/about-dental-implants/what-are-dental-implants

A more sophisticated approach is suggested by Moreo et al. [2007]. They proposed a computational model for the living bone-implant interface which has been applied for non-cemented hip implants. Bone-implant interface is modeled following the principles of continuum damage mechanics (CDM). The interface elements are established in terms of the jump of displacements, considering initial relative motion, and the tractions transmitted through the interface.

3 Fundamentals of Continuum Mechanics and Electrostatics

Continuum mechanics is an effective and powerful method to describe physical phenomena without considering the complexity of the microstructure. For this purpose, the description of the macroscopic behavior is essential and sufficient for engineering problems in many cases. Macroscopic length scale is applied in order to use continuum approach. All the materials are assumed as continuous media which are characterized by continuous field quantities such as density, temperature and velocity.

This chapter begins with brief and fundamental concepts in continuum mechanics consisting of movement and deformation for a three-dimensional body which will be applied in numerical analysis using finite element method later on in chapter 4. In section 3.2, the theory of electrostatics is expressed with regard to continuum mechanics for electromechanical problems which is needed in the context of this work. In section 3.3, the concepts of stress and electric displacements are introduced. Then the physical processes are presented based on fundamental balance equations in section 3.4. The constitutive theory of materials, which are considered in this study, are described in section 3.5.

In the following, the characteristics of piezoelectric materials are taken into account for the derivation of constitutive equations in the finite element applications. The chapter concludes with linear theory of piezoelasticity used for coupled electromechanical modeling. Contents provided in this chapter is already derived from literature. Therefore, the reader who need more detailed information on the subject of this chapter is referred to Holzapfel [2000] and Besson et al. [2010].

For further details on electromechanics, piezoelectricity and the derivation of the material law from thermodynamic potentials, interested readers may consult the literature such as Crowley [1986], Maugin [1988], Ikeda [1990] and Yang [2005b].

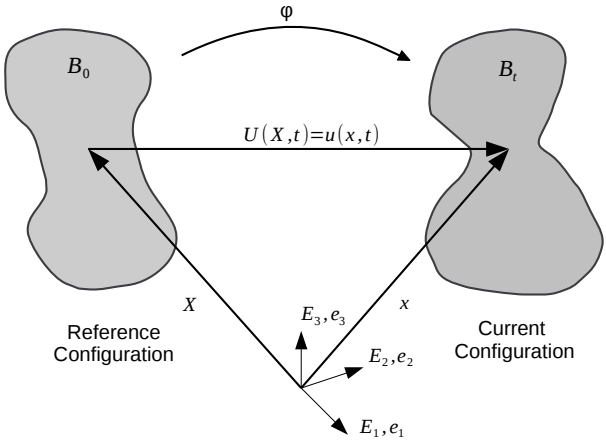

Figure 3.1: Reference and current configuration of a continuum body.

3.1 Kinematics

Kinematics is the branch of classical mechanics which describes the motion of continuous body in time of each material particle without considering the cause of deformation. In the theory of continuum mechanics, a body, denoted by $\mathcal{B}$, is defined as a closed and bounded set of material particles, which are continuously distributed in the domain. The placement of a whole set of material particles in an Euclidean space $\mathbb{R}^3$ at a given instant of time t is called the configuration of the body. The configuration of body at initial time $t = 0$ and subsequent time $t > 0$ are referred to reference $\mathcal{B}_0$ and current B_t configuration, respectively, as indicated in Fig 3.1. The material point of each configuration can be identified by the position vectors $\boldsymbol{X}$ and $\boldsymbol{x}$ relative to the fixed basis $\boldsymbol{E}_i$ and $\boldsymbol{e}_i$ as follows

$$\boldsymbol{X} = X_i \boldsymbol{E}_i \in \mathcal{B}_0, \tag{3.1}$$

$$\boldsymbol{x} = x_i \boldsymbol{e}_i \in \mathcal{B}_t. \tag{3.2}$$

The mapping φ is considered as a one-to-one correspondence of material points in order to describe deformation and motion from the reference configuration $\mathcal{B}_0$ to the current configuration $\mathcal{B}_t$. Then the relationship between $\boldsymbol{X}$ and $\boldsymbol{x}$ can be written as

$$\boldsymbol{x} = \varphi(\boldsymbol{X}, t), \tag{3.3}$$

$$\boldsymbol{X} = \varphi^{-1}(\boldsymbol{x}, t). \tag{3.4}$$

Furthermore, the motion of particles from the reference to the current configuration can be described by the displacement field considering material de-

scription (Lagrangian form)

$$\boldsymbol{U}(\boldsymbol{X},t)=\boldsymbol{x}(\boldsymbol{X},t)-\boldsymbol{X}. \tag{3.5}$$

Subsequently, the displacement field based on spatial description (Eulerian form) is written as

$$\boldsymbol{u}(\boldsymbol{x},t)=\boldsymbol{x}-\boldsymbol{X}(\boldsymbol{x},t). \tag{3.6}$$

These two equations are related with considering the mapping introduced by Eq. (3.4),

$$\boldsymbol{U}(\boldsymbol{X},t)=\boldsymbol{U}((\varphi^{-1}(\boldsymbol{x},t),t))=\boldsymbol{u}(\boldsymbol{x},t). \tag{3.7}$$

Hence, the displacement fields $\boldsymbol{U}$ and $\boldsymbol{u}$ have the same values with different arguments. The deformation of a continuum body takes place with the movement of reference (undeformed) to the current (deformed) configuration. Thus, the deformation gradient is introduced by second order tensor $\boldsymbol{F}$ for the mapping of an infinitesimal line element $\mathrm{d}\boldsymbol{X}$ to an equivalent one $\mathrm{d}\boldsymbol{x}$, as illustrated in Fig. 3.2. The transformation rule is defined by

$$\mathrm{d}\boldsymbol{x}=\boldsymbol{F}(\boldsymbol{X},t)\cdot\mathrm{d}\boldsymbol{X}, \tag{3.8}$$

$$\mathrm{d}\boldsymbol{X}=\boldsymbol{F}^{-1}(\boldsymbol{x},t)\cdot\mathrm{d}\boldsymbol{x}, \tag{3.9}$$

where

$$\boldsymbol{F}(\boldsymbol{X},t)=\frac{\partial\boldsymbol{x}}{\partial\boldsymbol{X}}=\frac{\partial\,\varphi(\boldsymbol{X},t)}{\partial\boldsymbol{X}}=\mathrm{Grad}\boldsymbol{x}(\boldsymbol{X},t), \tag{3.10}$$

$$\boldsymbol{F}^{-1}(\boldsymbol{x},t)=\frac{\partial\boldsymbol{X}}{\partial\boldsymbol{x}}=\frac{\partial\,\varphi^{-1}(\boldsymbol{x},t)}{\partial\boldsymbol{x}}=\mathrm{grad}\boldsymbol{X}(\boldsymbol{x},t). \tag{3.11}$$

In the following, the displacement gradient tensor in the material description is determined with combination of Eq. (3.5) and Eq. (3.10),

$$\begin{aligned}\mathrm{Grad}\boldsymbol{U}&=\mathrm{Grad}\boldsymbol{x}(\boldsymbol{X},t)-\mathrm{Grad}\boldsymbol{X}\\&=\boldsymbol{F}(\boldsymbol{X},t)-\boldsymbol{I}.\end{aligned} \tag{3.12}$$

The displacement gradient tensor in the spatial description is defined with regard to Eq. (3.6) and Eq. (3.11)

$$\begin{aligned}\mathrm{grad}\boldsymbol{u}&=\mathrm{grad}\boldsymbol{x}-\mathrm{grad}\boldsymbol{X}(\boldsymbol{x},t)\\&=\boldsymbol{I}-\boldsymbol{F}^{-1}(\boldsymbol{x},t).\end{aligned} \tag{3.13}$$

It has been already approved that points, curves and tangent vectors can be mapped from the reference to the current configuration by the deformation gradient $\boldsymbol{F}$. In order to map an infinitesimal surface dA and volume dV elements from the reference to the current configuration, two constrains should be considered: in the first place, deformation gradient $\boldsymbol{F}$ has to be nonsingular matrix in order to satisfy the inverse transformation condition

$$J(\boldsymbol{X},t)=\det\boldsymbol{F}(\boldsymbol{X},t)\neq 0\ , \tag{3.14}$$

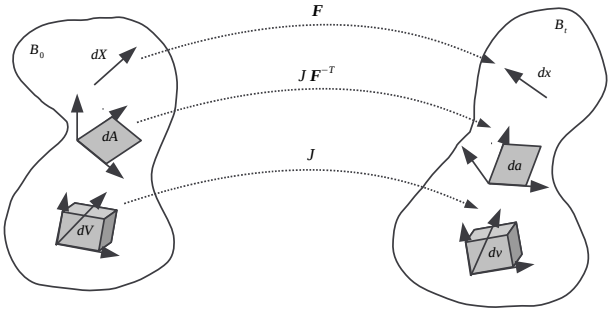

Figure 3.2: Transformation of line, area and volume elements.

and further, the volume ratio should be greater than zero $J(\boldsymbol{X}, t) > 0$. The relationship between reference and current configuration for an infinitesimal area and volume elements are represented as

$$\mathrm{d}\boldsymbol{a} = J\boldsymbol{F}^{-\mathrm{T}}\mathrm{d}\boldsymbol{A}. \tag{3.15}$$

$$\mathrm{d}\boldsymbol{v} = J\mathrm{d}\boldsymbol{V} \tag{3.16}$$

The time derivative of volume ratio $\dot{J}$ is provided using the relation of $J = det\boldsymbol{F}$ (Eq. (3.14)) and the chain rule

$$\dot{J} = \frac{\partial J}{\partial \boldsymbol{F}} : \dot{\boldsymbol{F}}. \tag{3.17}$$

Hence, the term $\frac{\partial J}{\partial \boldsymbol{F}}$ is represented by

$$\frac{\partial J}{\partial \boldsymbol{F}} = J\boldsymbol{F}^{-T}. \tag{3.18}$$

The definitions of velocity gradients in reference and current configuration read

$$\dot{\boldsymbol{F}} = \frac{\partial \boldsymbol{v}}{\partial \boldsymbol{X}} = Grad\dot{\boldsymbol{x}}, \tag{3.19}$$

$$\boldsymbol{l} = \frac{\partial \boldsymbol{v}}{\partial \boldsymbol{x}} = grad\dot{\boldsymbol{x}}, \tag{3.20}$$

which are associated to each other via the relationship

$$\boldsymbol{l} = \dot{\boldsymbol{F}} \cdot \boldsymbol{F}^{-1}. \tag{3.21}$$

Consequently, with equations (3.21) and (3.18), $\dot{J}$ is reformulated as

$$\begin{aligned} \dot{J} &= J\boldsymbol{F}^{-T} : \boldsymbol{l}\boldsymbol{F} \\ &= J\boldsymbol{F}^{-T}\boldsymbol{F}^{T} : \boldsymbol{l} = J\boldsymbol{I} : grad\dot{\boldsymbol{x}} \\ &= Jtr(grad\dot{\boldsymbol{x}}) = J \operatorname{div}\dot{\boldsymbol{x}}. \end{aligned} \tag{3.22}$$

In nonlinear continuum mechanics, numerous definitions have been proposed for strain tensors. A common definition of the strain tensor is described by Green-Lagrange strain tensor $\boldsymbol{E}$. A strain measure can be obtained using the concept of the squared change of length of an infinitesimal line element in reference and current configuration as follows

$$||\mathrm{d}\boldsymbol{x} \cdot \mathrm{d}\boldsymbol{x}|| - ||\mathrm{d}\boldsymbol{X} \cdot \mathrm{d}\boldsymbol{X}|| = \mathrm{d}\boldsymbol{x} \cdot \mathrm{d}\boldsymbol{x} - \mathrm{d}\boldsymbol{X} \cdot \mathrm{d}\boldsymbol{X} \tag{3.23}$$

$$= \mathrm{d}\boldsymbol{X} \cdot \boldsymbol{F}^{\mathrm{T}} \cdot \boldsymbol{F} \cdot \mathrm{d}\boldsymbol{X} - \mathrm{d}\boldsymbol{X} \cdot \mathrm{d}\boldsymbol{X} \tag{3.24}$$

$$= \mathrm{d}\boldsymbol{X} \cdot \left(\boldsymbol{F}^{\mathrm{T}} \cdot \boldsymbol{F} - 1\right) \cdot \mathrm{d}\boldsymbol{X} \tag{3.25}$$

$$= \mathrm{d}\boldsymbol{X} \cdot 2\boldsymbol{E} \cdot \mathrm{d}\boldsymbol{X}, \tag{3.26}$$

where

$$\boldsymbol{E} = \frac{1}{2}(\boldsymbol{F}^{\mathrm{T}} \cdot \boldsymbol{F} - 1), \tag{3.27}$$

is Green-Lagrange strain tensor and the right Cauchy-Green deformation tensor is denoted by

$$\boldsymbol{C} = \boldsymbol{F}^{\mathrm{T}} \cdot \boldsymbol{F}. \tag{3.28}$$

The deformation gradient can be rewritten as

$$\boldsymbol{F} = \frac{\partial \boldsymbol{x}}{\partial \boldsymbol{X}} = \frac{\partial \boldsymbol{X}}{\partial \boldsymbol{X}} + \frac{\partial \boldsymbol{u}}{\partial \boldsymbol{X}} = \boldsymbol{I} + \boldsymbol{H}. \tag{3.29}$$

Hence, the Green-Lagrange strain tensor is expressed in terms of the displacement gradient by

$$\boldsymbol{E} = \frac{1}{2}\left(\boldsymbol{H} + \boldsymbol{H}^{\mathrm{T}} + \boldsymbol{H}^{\mathrm{T}} \cdot \boldsymbol{H}\right). \tag{3.30}$$

For small strains the higher order term can be neglected. By that, the linearised small strain tensor is achieved

$$\boldsymbol{\varepsilon} = \frac{1}{2}\left(\boldsymbol{H} + \boldsymbol{H}^{\mathrm{T}}\right). \tag{3.31}$$

In this study, small deformation theory is considered. Thus, linear theory is applied using linear strain tensor $\boldsymbol{\varepsilon}$.

3.2 Electrostatics

Electrostatics is the branch of physics that encompasses phenomena dealing with the interaction of stationary or moving electrical charges. The mathematical methods of electrostatics are constructed to calculate the distributions of the electric field, electric charge, etc.

Coulomb's law states: the magnitude of the electrostatic force $\boldsymbol{F}_c$ that acts

between two point electric charges Q_a and Q_b depends on the magnitudes of charges and the distance between them,

$$\| \boldsymbol{F}_c \| = \frac{Q_a Q_b}{4\pi\varepsilon_0 \| \boldsymbol{X}_a - \boldsymbol{X}_b \|^2}. \tag{3.32}$$

The constant $\epsilon_0 = 8.854e^{-12}\frac{C^2}{Jm}$ is called the vacuum permittivity. The resulting force for more than two point charges can be determined using superposition principle. The schematic interpretation of Coulomb's law is indicated in Fig. 3.3.

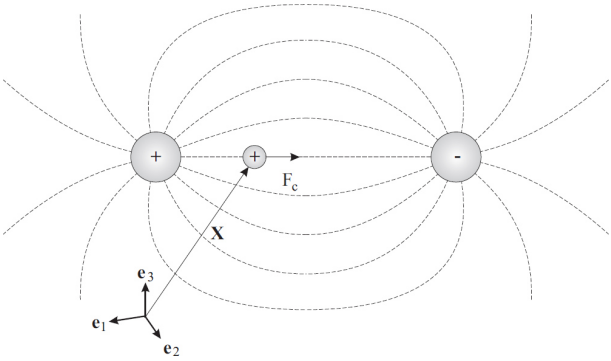

Figure 3.3: Charged particle in an electrical field of two point charges.

The electrical field strength $\boldsymbol{E}$ is defined at a position $\boldsymbol{X}$ from fixed basis $\boldsymbol{e}_i$ as follows

$$\boldsymbol{E}(\boldsymbol{X}) = \frac{\boldsymbol{F}_c}{Q}. \tag{3.33}$$

Furthermore, the relationship between electric potential ϕ and electrical field $\boldsymbol{E}$ is introduced with choosing $\boldsymbol{X}_0$ as reference position

$$\phi = \int_{\boldsymbol{X}_0}^{\boldsymbol{X}_1} \boldsymbol{E} \mathrm{d}\boldsymbol{X}, \tag{3.34}$$

or

$$\boldsymbol{E} = -grad\phi. \tag{3.35}$$

From a physical point of view, an electric potential in the current configuration reads

$$\phi_t = \int_{\boldsymbol{x}_0}^{\boldsymbol{x}_1} \boldsymbol{e} \mathrm{d}\boldsymbol{x} = \int_{\boldsymbol{x}_0}^{\boldsymbol{x}_1} \boldsymbol{E}\boldsymbol{F}^{-1} \mathrm{d}\boldsymbol{x}. \tag{3.36}$$

3.3 Stresses and Electric Displacements

3.3.1 Stress Measures

Stress is a physical quantity which is represented as a measure of internal load within the body. Internal forces can be identified in an arbitrary loaded area of body. Various types of stress measures are defined in different configurations. The most commonly used measure of stress is referred to the Cauchy stress vector $\boldsymbol{t}$ described in current configuration. The Cauchy stress vector can be computed from a traction vector $\mathrm{d}\boldsymbol{f}$ acting on an infinitesimal surface element $\mathrm{d}a$

$$\boldsymbol{t} = \frac{\mathrm{d}\boldsymbol{f}}{\mathrm{d}a}. \tag{3.37}$$

Applying Cauchy theorem that assumes a linear relationship between the traction vector $\boldsymbol{t}$ and the normal vector $\boldsymbol{n}$ of the area $\mathrm{d}a$, the Cauchy stress tensor can be written as

$$\boldsymbol{t}(\boldsymbol{x}, t, \boldsymbol{n}) = \boldsymbol{\sigma}(\boldsymbol{x}, t) \cdot \boldsymbol{n}. \tag{3.38}$$

Other measures of stress with respect to the undeformed state are required for some engineering applications. Hence, the first Piola-Kirchhoff traction vector $\boldsymbol{T}$ can be determined from a traction vector $\mathrm{d}\boldsymbol{f}$ acting on an infinitesimal surface element of reference configuration $\mathrm{d}A$

$$\boldsymbol{T} = \frac{\mathrm{d}\boldsymbol{f}}{\mathrm{d}A}. \tag{3.39}$$

The first Piola-Kirchhoff stress tensor is similarly obtained using Cauchy theorem

$$\boldsymbol{T}(\boldsymbol{X}, t, \boldsymbol{N}) = \boldsymbol{P}(\boldsymbol{X}, t) \cdot \boldsymbol{N}. \tag{3.40}$$

The first Piola-Kirchhoff stress tensor can be obtained in terms of the Cauchy stress by multiplying Eq. (3.38) with $\mathrm{d}a$ and using Eq. (3.15)

$$\boldsymbol{t}\mathrm{d}a = \boldsymbol{\sigma} \cdot \boldsymbol{n}\mathrm{d}a = J\boldsymbol{\sigma} \cdot \boldsymbol{F}^{-T} \cdot \boldsymbol{N}\mathrm{d}A = \boldsymbol{T}\mathrm{d}A, \tag{3.41}$$

$$\boldsymbol{P} = J\boldsymbol{\sigma} \cdot \boldsymbol{F}^{-T}. \tag{3.42}$$

Accordingly, the stress in one material point is described by nominal stress $\boldsymbol{P}$ and the true stress $\boldsymbol{\sigma}$.

3.3.2 The Electric Displacement

In a dielectric material the bound charges are slightly displaced in the presence of an electric field $\boldsymbol{E}$ which induces a local electric dipole moment. The electric displacement field $\boldsymbol{D}$ is defined as

$$\boldsymbol{D} = \varepsilon_0 \boldsymbol{E} + \boldsymbol{P}, \tag{3.43}$$

where $\varepsilon_0 = 8.85 \times 10^{-12} F/m$ is the vacuum permittivity and polarization density $\boldsymbol{P}$ is defined as the macroscopic density of permanent and induced electric dipole moment. In a linear, homogeneous and isotropic dielectric material with quick response to variations in the electric field, P depends linearly on the electric field

$$\boldsymbol{P} = \varepsilon_0 \chi \boldsymbol{E}, \tag{3.44}$$

where the constant of proportionality χ is called the electric susceptibility of the material. Thus, Eq. (3.43) can be reformulated as

$$\boldsymbol{D} = \varepsilon_0 (1 + \chi) \boldsymbol{E} = \varepsilon \boldsymbol{E}, \tag{3.45}$$

with electric permittivity $\varepsilon = \varepsilon_0 \varepsilon_r$ and the relative permittivity $\varepsilon_r = 1 + \chi$. The contribution of the electric displacement field, which is perpendicular to the surface, to the electric flux Ψ is defined by

$$\Psi = \int_\Gamma \boldsymbol{D} \cdot \boldsymbol{N} \mathrm{d}A. \tag{3.46}$$

Finally, the electric flux through a closed surface is equal to the total charge inside of this surface

$$\Psi = \oint_\Gamma \boldsymbol{D} \cdot \boldsymbol{N} \mathrm{d}A = \int_\Omega \rho_0^{el} \mathrm{d}V = Q, \tag{3.47}$$

where ρ_0^{el} represents the electric charge density.

3.4 Balance Laws

Within this chapter, fundamental physical balance laws will be summarized in the context of continuum mechanics and thermodynamics. In the following, these conservation laws contain conservation of mass, the momentum conservation laws, the balance of energy and entropy inequality are outlined. They are valid and applicable for all materials modeled as continuum media and must be satisfied for all times.

The general expression of a balance law for a physical field measure $\boldsymbol{Z}(x,t)$ in spatial coordination is written as follows, Truesdell and Noll [1960],

$$\frac{\mathrm{d}}{\mathrm{d}t} \int_\Omega Z \mathrm{d}v = \int_\Omega \big(\Xi_f + \Xi_p\big) \mathrm{d}v + \int_\Gamma \Lambda \mathrm{d}a, \tag{3.48}$$

where Ξ_f is the volumetric flow (inflow and outflow), Ξ_p is the volumetric production and Λ is the surface flow (inflow and outflow).

3.4.1 Conservation of Mass

In this work, the mass of the system under consideration is not necessarily constant (Krstin et. al. [2000]). The quantity of density ρ varies with time t under mechanical stimulus in the context of bone remodeling and osseointegration. Therefore, the mass of the system under consideration is not preserved in general. The mathematical expression for the mass of a body in the current configurations

$$m(t) = \int_{\mathcal{B}_t} \rho(\boldsymbol{x}, t) dv \neq \text{const.}, \tag{3.49}$$

is determined by the volume integral of mass density ρ over the entire body. Thus, the time derivative of the mass balance is not zero in contrast to a mass invariant system

$$\frac{\mathrm{d}}{\mathrm{d}t} m = \frac{\mathrm{d}}{\mathrm{d}t} \int_{\mathcal{B}_t} \rho \mathrm{d}v \neq 0. \tag{3.50}$$

The mass change rate with respect to equation (3.16) can be expressed as

$$\frac{\mathrm{d}}{\mathrm{d}t} m = \frac{\mathrm{d}}{\mathrm{d}t} \int_{\mathcal{B}_t} \rho \mathrm{d}v = \frac{\mathrm{d}}{\mathrm{d}t} \int_{\mathcal{B}_0} \rho J \mathrm{d}V, \tag{3.51}$$

which can be reformulated as

$$\dot{m} = \frac{\mathrm{d}}{\mathrm{d}t} \int_{\mathcal{B}_0} \varrho \, J \, \mathrm{d}V = \int_{\mathcal{B}_0} \frac{\mathrm{d}}{\mathrm{d}t} \left(\varrho \, J\right) \mathrm{d}V = \int_{\mathcal{B}_0} \dot{\varrho} \, J + \varrho \, \dot{J} \, \mathrm{d}V \ . \tag{3.52}$$

The mass flow rate equation is rewritten using (3.22) as

$$\dot{m} = \int_{\mathcal{B}_0} \left(\dot{\varrho} \, J + \varrho \ \mathrm{div}\left(\boldsymbol{v}\right) \, J\right) \ \mathrm{d}V = \int_{\mathcal{B}_t} (\dot{\rho} + \rho \ \mathrm{div}\, \dot{\boldsymbol{x}}) \mathrm{d}v. \tag{3.53}$$

Moreover, the change of the mass in the system is described by

$$\frac{\mathrm{d}}{\mathrm{d}t} \int_{\mathcal{B}_t} \rho \mathrm{d}v = \int_{\mathcal{B}_t} \hat{\rho} \mathrm{d}v. \tag{3.54}$$

The local form of the balance of mass for an arbitrary volume is obtaind by

$$\dot{\rho} + \rho \ \mathrm{div}\, \dot{\boldsymbol{x}} = \hat{\rho} \ . \tag{3.55}$$

which must be valid at every point of the body. The second term describes the transport of mass within the system, which is not considered here. Under this assumption, the local form of mass balance is specified

$$\dot{\rho} = \hat{\rho} \ . \tag{3.56}$$

3.4.2 Conservation of Linear and Angular Momentum

The linear momentum vector for a material body $\mathcal{B}_t$ is introduced as follows,

$$\boldsymbol{L} = \int_{\mathcal{B}_t} \rho \dot{\boldsymbol{x}} \mathrm{d}v. \tag{3.57}$$

The conservation of linear momentum is derived from Newton's second law of motion. Accordingly, the change of momentum with time is equal to the sum of all body and external forces acting on the body. This can be written as follows from Eq. (3.48)

$$\frac{\mathrm{d}}{\mathrm{d}t} \int_{\mathcal{B}_t} \rho \dot{\boldsymbol{x}} \mathrm{d}v = \int_{\mathcal{B}_t} (\rho \boldsymbol{b} + \boldsymbol{f}^{el}) \mathrm{d}v + \int_{\partial \mathcal{B}_t} \boldsymbol{t} \mathrm{d}a, \tag{3.58}$$

where $\rho \boldsymbol{b}$ denotes the gravitational force per unit volume, $\boldsymbol{f}^{el}$ are the electromagnetically induced volume forces and $\boldsymbol{t}$ the stress vector according to external loads. By applying Cauchy theorem Eq. (3.38) together with the divergence theorem, the last term of Eq. (3.58) can be reformulated

$$\int_{\partial \mathcal{B}_t} \boldsymbol{t} \mathrm{d}a = \int_{\partial \mathcal{B}_t} \boldsymbol{\sigma} \cdot \boldsymbol{n} \mathrm{d}a = \int_{\mathcal{B}} \operatorname{div} \boldsymbol{\sigma} \mathrm{d}v. \tag{3.59}$$

Consequently, the global form of linear momentum balance in spatial configuration using the transport theorem is obtained,

$$\int_{\mathcal{B}_t} (\dot{\rho} \dot{\boldsymbol{x}} + \rho \dot{\boldsymbol{x}} \operatorname{div} \dot{\boldsymbol{x}} + \rho \ddot{\boldsymbol{x}}) \mathrm{d}v = \int_{\mathcal{B}_t} (\rho \boldsymbol{b} + \boldsymbol{f}^{el} + \operatorname{div} \boldsymbol{\sigma}) \mathrm{d}v. \tag{3.60}$$

This can be written in the local form of the momentum balance,

$$\dot{\rho} \dot{\boldsymbol{x}} + \rho \dot{\boldsymbol{x}} \operatorname{div} \dot{\boldsymbol{x}} + \rho \ddot{\boldsymbol{x}} = \rho \boldsymbol{b} + \boldsymbol{f}^{el} + \operatorname{div} \boldsymbol{\sigma}. \tag{3.61}$$

In piezoelasticity, the effect of the electromagnetically induced volume forces $\boldsymbol{f}^{el}$ can be neglected. The local form of the momentum balance with respect to previous assumption of mass transport and Eq. (3.56) reduces to

$$\rho \ddot{\boldsymbol{x}} = \rho \boldsymbol{b} + \operatorname{div} \boldsymbol{\sigma} - \hat{\rho} \dot{\boldsymbol{x}}. \tag{3.62}$$

The angular momentum $\boldsymbol{J}$ can be derived from linear momentum 3.57 with respect to position vector $\boldsymbol{x}$

$$\boldsymbol{J} = \int_{\partial \mathcal{B}} \boldsymbol{x} \times \rho \dot{\boldsymbol{x}} \mathrm{d}v. \tag{3.63}$$

Analogeous to linear momentum, the material time derivative of angular momentum is equal to the sum of all torques which are caused from internal and external forces

$$\frac{\mathrm{d}}{\mathrm{d}t} \int_{\partial \mathcal{B}} \boldsymbol{x} \times \rho \dot{\boldsymbol{x}} \mathrm{d}v = \int_{\mathcal{B}_t} \boldsymbol{x} \times \rho \boldsymbol{b} \mathrm{d}v + \int_{\partial \mathcal{B}_t} \boldsymbol{x} \times \boldsymbol{t} \mathrm{d}a. \tag{3.64}$$

Which leads to the known symmetry of Cauchy stress tensor $\boldsymbol{\sigma} = \boldsymbol{\sigma}^{\mathrm{T}}$, Balke [2010].

3.4.3 Conservation of Electric Charge

The overall electric charge remains constant in a balanced manner in the closed system. The electric charge Q with respect to the electric charge density ρ_0^{el} in the reference configuration can be introduced as follows

$$Q = \int_{\mathcal{B}_0} \rho_0^{el} \, \mathrm{d}V. \tag{3.65}$$

The electric current can be described by

$$\boldsymbol{I} = \int_{A} \boldsymbol{J}_0^{el} \, \mathrm{d}A, \tag{3.66}$$

with a quantity known as the current density $\boldsymbol{J}_0^{el}$. The temporal change of electric charge is caused from electric current $\boldsymbol{I}$. Accordingly, electric charge conservation law using divergence theorem can be written

$$\int_{\mathcal{B}_0} \operatorname{div} \boldsymbol{J}_0^{el} \, \mathrm{d}V = -\frac{\mathrm{d}}{\mathrm{d}t} \int_{\mathcal{B}_0} \rho_0^{el} \, \mathrm{d}V. \tag{3.67}$$

The local form is

$$\dot{\rho}_0^{el} + \operatorname{div} \boldsymbol{J}_0^{el} = 0. \tag{3.68}$$

3.4.4 Conservation of Energy

In the context of thermodynamics, the transformation of different types of energy (e.g. mechanical, thermal, chemical or electrical energy) from one form to another is considered during a deformation processes of a continuum body. Following the first law of thermodynamics, the total energy of a body has to be preserved during the whole process which means that energy can be transformed from one to the other form, but cannot be created or destroyed. Accordingly, the time derivatives of internal energy $\mathcal{U}$ and kinetic energy $\mathcal{K}$ have to be equal to the sum of work of external forces $\mathcal{W}$ and heat supply $\mathcal{Q}$

$$\dot{\mathcal{U}} + \dot{\mathcal{K}} = \mathcal{W} + \mathcal{Q}. \tag{3.69}$$

These quantities can be introduced in current configuration by

$$\mathcal{U} = \int_{\mathcal{B}_t} \rho u \, \mathrm{d}v, \tag{3.70}$$

$$\mathcal{K} = \int_{\mathcal{B}_t} \frac{1}{2} \rho \dot{\boldsymbol{x}} \cdot \dot{\boldsymbol{x}} \, \mathrm{d}v, \tag{3.71}$$

$$\mathcal{W} = \int_{\mathcal{B}_t} \rho \boldsymbol{b} \cdot \dot{\boldsymbol{x}} \, \mathrm{d}v + \int_{\partial \mathcal{B}_t} \boldsymbol{t} \cdot \dot{\boldsymbol{x}} \, \mathrm{d}a, \tag{3.72}$$

$$\mathcal{Q} = \int_{\mathcal{B}_t} \rho r \, \mathrm{d}v - \int_{\partial \mathcal{B}_t} \boldsymbol{q} \cdot \boldsymbol{n} \, \mathrm{d}a, \tag{3.73}$$

where $\boldsymbol{u}$ denotes the specific internal energy, r is specific internal heat source and $\boldsymbol{q}$ the heat flux over the boundaries. The global form of the energy conservation using above definitions can be written as

$$\frac{\mathrm{d}}{\mathrm{d}t}\int_{\mathcal{B}_t}\rho\left(u+\frac{1}{2}\rho\dot{\boldsymbol{x}}\cdot\dot{\boldsymbol{x}}\right)\mathrm{d}v=\int_{\mathcal{B}_t}\rho\left(\boldsymbol{b}\cdot\dot{\boldsymbol{x}}+r\right)\mathrm{d}v+\int_{\partial\mathcal{B}_t}\left(\boldsymbol{t}\cdot\dot{\boldsymbol{x}}-\boldsymbol{q}\cdot\boldsymbol{n}\right)\mathrm{d}a. \tag{3.74}$$

Above equation using Cauchy and divergence theorem can be reformulated as

$$\frac{\mathrm{d}}{\mathrm{d}t}\int_{\mathcal{B}_t}\rho\left(u+\frac{1}{2}\rho\dot{\boldsymbol{x}}\cdot\dot{\boldsymbol{x}}\right)\mathrm{d}v=\int_{\mathcal{B}_t}\left[\rho\left(\boldsymbol{b}\cdot\dot{\boldsymbol{x}}+r\right)+\ \mathrm{div}\left(\boldsymbol{\sigma}\right)\cdot\dot{\boldsymbol{x}}-\ \mathrm{div}\,\boldsymbol{q}\right]\mathrm{d}v. \tag{3.75}$$

The local form of the balance of energy with respect to transport theorem leads to

$$\begin{aligned}&\dot{\rho}u+\rho\dot{u}+\rho u\,\mathrm{div}\,\dot{\boldsymbol{x}}+\frac{1}{2}\dot{\rho}\dot{\boldsymbol{x}}\cdot\dot{\boldsymbol{x}}+\rho\ddot{\boldsymbol{x}}\cdot\dot{\boldsymbol{x}}+\rho\dot{\boldsymbol{x}}\cdot\dot{\boldsymbol{x}}\,\mathrm{div}\,\dot{\boldsymbol{x}}=\\&\rho\boldsymbol{b}\cdot\dot{\boldsymbol{x}}+\rho r+\mathrm{grad}(\dot{\boldsymbol{x}})\cdot\cdot\boldsymbol{\sigma}+\dot{\boldsymbol{x}}\cdot\ \mathrm{div}\,\boldsymbol{\sigma}-\ \mathrm{div}\,\boldsymbol{q}.\end{aligned} \tag{3.76}$$

Based on previous assumptions for momentum balance Eq. (3.61) and using Eq. (3.56), the local form reduces to

$$\rho\dot{u}=\mathrm{grad}(\dot{\boldsymbol{x}})\cdot\cdot\boldsymbol{\sigma}+\rho r-\ \mathrm{div}\left(\boldsymbol{q}\right)-\hat{\rho}\left(u+\frac{1}{2}\dot{\boldsymbol{x}}\cdot\dot{\boldsymbol{x}}\right), \tag{3.77}$$

which is simplified for small deformations and isothermal processes in

$$\rho\dot{u}=\boldsymbol{\sigma}\cdot\cdot\dot{\boldsymbol{\varepsilon}}-\hat{\rho}\left(u+\frac{1}{2}\dot{\boldsymbol{x}}\cdot\dot{\boldsymbol{x}}\right). \tag{3.78}$$

3.4.5 The Second Law of Thermodynamics

Before explaining the second law of thermodynamics the concept of entropy should be introduced. Entropy is defined as a measure of microscopic disorder within a thermodynamic system. The entropy $\mathcal{S}$ is measured per unit mass η in the region of interest, denoted by

$$\mathcal{S}=\int_{\mathcal{B}_t}\rho\eta\mathrm{d}v. \tag{3.79}$$

The second law of thermodynamics describes the direction of energy transfer process. It states that the rate of change of entropy is always larger or equal than input entropy of system

$$\frac{\mathrm{d}}{\mathrm{d}t}\int_{\mathcal{B}_t}\rho\eta\mathrm{d}v\geq\int_{\mathcal{B}_t}\frac{1}{T}\rho r\mathrm{d}v-\int_{\partial\mathcal{B}_t}\frac{1}{T}\boldsymbol{q}\cdot\boldsymbol{n}\mathrm{d}a. \tag{3.80}$$

The surface integral is converted into the volume integral using divergence theorem

$$\int_{\partial\mathcal{B}_t} \frac{1}{T}\boldsymbol{q}\cdot\boldsymbol{n}\mathrm{d}a = \int_{\partial\mathcal{B}_t} \mathrm{div}\left(\frac{1}{T}\boldsymbol{q}\right)\mathrm{d}v = \int_{\partial\mathcal{B}_t}\left(\frac{1}{T}\,\mathrm{div}\,\boldsymbol{q} - \frac{1}{T^2}\boldsymbol{q}\cdot\mathrm{grad}\,T\right)\mathrm{d}v. \tag{3.81}$$

Then, the local form can be derived as

$$T\frac{\mathrm{d}}{\mathrm{d}t}(\rho\eta) \geq \rho r - \mathrm{div}\,\boldsymbol{q} + \boldsymbol{q}\cdot\mathrm{grad}\,T. \tag{3.82}$$

Applying the time derivative and using the energy balance, above equation is simplified after a few transformations

$$T\Big(\rho\dot{\eta}+\hat{\rho}\eta\Big) - \hat{\rho}\left(u+\frac{1}{2}\dot{\boldsymbol{x}}\cdot\dot{\boldsymbol{x}}\right) - \rho\dot{u} + \boldsymbol{\sigma}\cdot\cdot\dot{\boldsymbol{\varepsilon}} - \boldsymbol{q}\cdot\mathrm{grad}T \geq 0. \tag{3.83}$$

Using the definition of free Helmholtz energy ψ

$$\psi = u - T\eta, \tag{3.84}$$

gives an alternative form of the second law of thermodynamics, referred to as Clausius-Duhem inequality

$$T\big(\rho\dot{\eta}+\hat{\rho}\eta\big) - \hat{\rho}\left(\psi+T\eta+\frac{1}{2}\dot{\boldsymbol{x}}\cdot\dot{\boldsymbol{x}}\right) - \rho\big(\dot{\psi}+\dot{T}\eta+T\dot{\eta}\big) + \boldsymbol{\sigma}\cdot\cdot\dot{\boldsymbol{\varepsilon}} - \boldsymbol{q}\cdot\mathrm{grad}(T)\frac{1}{T} \geq 0 \tag{3.85}$$

For isothermal process and static case $\dot{\boldsymbol{x}} = 0$, Clausius-Duhem equation reduces to

$$\mathcal{D} = -\rho\dot{\psi} - \hat{\rho}\psi + \boldsymbol{\sigma}\cdot\cdot\dot{\boldsymbol{\varepsilon}} \geq 0. \tag{3.86}$$

3.5 Constitutive Theory

The kinematic and kinetic relations of continuum mechanics presented in the previous section are valid for all continuous system regardless of the types of materials. However, the number of unknowns in the thermodynamical problem is higher than the number of equations which are provided by the balance laws. Furthermore, the specific characteristic of material can not be explained by the balance principles. Therefore, constitutive equations are formulated based on fundamental principles of the theory of materials.

Some of the most important principles that must be fulfilled for any constitutive model are outlined below.

Physical consistency: The constitutive equations have to be satisfied by the thermodynamic balance laws summarized in section 3.4.

Causality: Dependent and independent variables are classified in the concept of cause and effect. For instant, motion and temperature are placed in the independent variables category, However, stress, heat flow, entropy and free energy are dependent variables.

Determinism: The current state of independent variables is determined from its kinematic and temperature history.

Equipresence: The independent variables have the same presence in all constitutive equations, unless this presence has a paradox with general rules of physics.

Local effects and fading memory: The current state of particles is affected only by its close surroundings and the history of near past, long-term effects can be neglected.

Objective: The constitutive equations must be independent of the selected reference system. In particular they must be invariant with respect to rigid body motions.

Material symmetry: The materials have the same behavior under rotations so-called groups of the material symmetry

3.5.1 Constitutive Description of Bone Remodeling

Despite the fact that the biological process for electromechanically stimulating ingrowth of bone implants is different from long term bone remodeling, it can be described in a similar phenomenological manner at the macroscopic length-scale. Since bone tissue behaves as a piezoelectric material as discussed in the literature, a difference in the electrical potential can affect a variation of bone density. Therefore, the development of a bone remodeling theory for the investigation of piezoelectric reaction of bones due to mechanical demands appears straight forward.

Accordingly a novel electromechanical stimulation of bone remodeling at a continuum level has been proposed by Garzón-Alvarado et al. [2012] using a first order modeling approach introduced by Nackenhorst [2006] as a starting point. Evolution equations for the bone mineral density ρ in dependency of the mechanical and electrical stimulus can be formulated, hypothetically, as

$$\frac{\mathrm{d}\rho}{\mathrm{d}t} = k_1\left(\frac{\psi_{mech}}{\psi_{ref_m}} - 1\right) + k_2\left(\frac{\psi_{elec}}{\psi_{ref_e}} - 1\right) , \tag{3.87}$$

where ψ_{mech} denotes the strain energy density, ψ_{elec} is the electric energy density, k_1 and k_2 are time constants which have been chosen equally for simplicity $k_1 = k_2 = 1$ and ψ_{ref_m} and ψ_{ref_e} are defined as physiological target values for the strain and electric energy density, respectively.

From the computational point of view, the bone mineral density is considered as an internal variable which is specified in each integration point in the finite element analysis. The related evolution equations are integrated with implicit Euler scheme in analogy to computational inelasticity. In this study, the aforementioned mathematical theory is adapted for the simulation of bony ingrowth of dental prosthesis for the investigation of their primal stability.

Since the osseointegration process and bone remodeling happen at different time scales, only the time constants will be distinguished. However, a scaling of the time constants is not considered in this contribution, as related clinical experience is missing. In the following, the mathematical model of the proposed phenomenonological continuum is outlined.

Mechanical Stimulus

A constitutive model for the biomechanical interaction is introduced in the framework of continuum theory of materials. The free energy density function is defined in dependency of strain tensor and a scalar valued internal variable, namely the bone mineral density ρ,

$$\psi_{mech} = \psi_{mech}(\varepsilon, \rho) \; . \tag{3.88}$$

The time derivative of free energy,

$$\dot{\psi}_{mech} = \frac{\partial \psi_{mech}}{\partial \boldsymbol{\varepsilon}} \cdot \cdot \dot{\boldsymbol{\varepsilon}} + \frac{\partial \psi_{mech}}{\partial \rho} \dot{\rho}, \tag{3.89}$$

is substituted into the Clausius-Duhem inequality 3.86

$$-\rho \left(\frac{\partial \psi_{mech}}{\partial \boldsymbol{\varepsilon}} \cdot \cdot \dot{\boldsymbol{\varepsilon}} + \frac{\partial \psi_{mech}}{\partial \rho} \; \dot{\rho} \right) - \dot{\rho} \; \psi_{mech} + \dot{\boldsymbol{\varepsilon}} \cdot \cdot \boldsymbol{\sigma} \geq 0, \tag{3.90}$$

which can be converted to

$$\left(\boldsymbol{\sigma} - \rho \frac{\partial \psi_{mech}}{\partial \boldsymbol{\varepsilon}} \right) \cdot \cdot \dot{\boldsymbol{\varepsilon}} - \rho \frac{\partial \psi_{mech}}{\partial \rho} \dot{\rho} - \dot{\rho} \psi_{mech} \geq 0. \tag{3.91}$$

Globally we solve the mechanical equilibrium equation considering body and inertia forces to be negligible, i.e.

$$div(\boldsymbol{\sigma}) = 0, \tag{3.92}$$

with the symmetric Cauchy stress tensor $\boldsymbol{\sigma} = \boldsymbol{\sigma}^T$. Small deformation theory is assumed which justifies a kinematic description by the linear strain tensor

$$\boldsymbol{\varepsilon} = \frac{1}{2} \left(\nabla u + (\nabla u)^T \right) \; , \tag{3.93}$$

where u is the displacement field. The constitutive relationship is expressed by a free energy density, i.e.

$$\boldsymbol{\sigma} = \rho \frac{\partial \psi_{mech}}{\partial \boldsymbol{\varepsilon}}, \tag{3.94}$$

the stress tensor is derived from a free energy density function ψ_{mech}. By substituting stress Eq. 3.94 into Eq. 3.91, it can be found

$$-\varrho \, \frac{\partial \, \psi_{mech}}{\partial \, \varrho} \, \dot{\varrho} - \dot{\varrho} \, \psi_{mech} \geq 0, \tag{3.95}$$

from which the dissipation of biomechanics is determined by

$$D^{bio} = -\rho \, \frac{\partial \, \psi_{mech}}{\partial \, \rho} \dot{\rho}. \tag{3.96}$$

The strain energy density function is introduced in the framework of linear elasticity as

$$\psi_{mech} = \frac{1}{2\rho} \varepsilon \cdot \cdot \mathbb{C}(\rho) \cdot \cdot \varepsilon \, , \tag{3.97}$$

where $\mathbb{C}(\rho)$ is the isotropic linear elastic tensor which depends on local bone mineral density. Within the framework of an isotropic first order theory, Young's modulus and elastic constitutive tensor can be written in dependency of bone mineral density as

$$E(\rho) = E_0 (\frac{\rho}{\rho_0})^n \, , \quad \text{i.e.} \quad \mathbb{C}(\rho) = \frac{E(\rho)}{E_0} \mathbb{C}_0, \tag{3.98}$$

where $\mathbb{C}_0$ is the linear elastic tensor with constant coefficients E_0, i.e.

$$\mathbb{C}_0 \; = \; \frac{E_0}{(1+\nu)(1-2\nu)} \begin{pmatrix} 1-\nu & \nu & \nu & 0 & 0 & 0 \\ \nu & 1-\nu & \nu & 0 & 0 & 0 \\ \nu & \nu & 1-\nu & 0 & 0 & 0 \\ 0 & 0 & 0 & \frac{1-2\nu}{2} & 0 & 0 \\ 0 & 0 & 0 & 0 & \frac{1-2\nu}{2} & 0 \\ 0 & 0 & 0 & 0 & 0 & \frac{1-2\nu}{2} \end{pmatrix}. \tag{3.99}$$

The constitutive relationship between bone mass density and modulus of elasticity in bones is still a subject of research. This relationship experimentally derived by Carter and Hayes [1977]

$$E_{CH}(\rho) = 3790 \, \dot{\boldsymbol{\varepsilon}}^{0.06} \, \rho^3, \tag{3.100}$$

is presented in the literature. Moreover, there are several other experimentally determined equations, e.g. Linde et al. [1991]; Keyak and Falkinstein [2003]; Snyder and Schneider [1991]; Wirtz et al. [2000]; Rho et al. [1995]. Morgan et al. [2003] proposed the following expression, i.e.

$$E_M(\rho) = 8920 \, \rho^{1.83}, \tag{3.101}$$

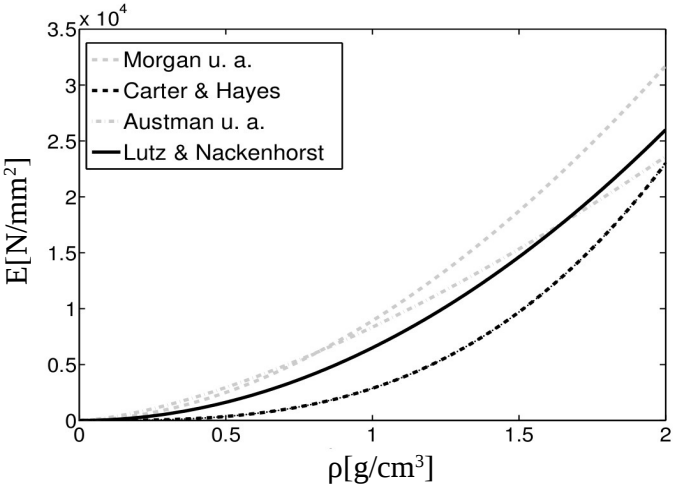

Figure 3.4: Comparison of different constitutive models E_M, E_{CH}, E_A and E_L for bone modulus of elasticity with respect to the density, Lutz and Nackenhorst [2011].

where the magnitude of measured strain is underestimated. In contrast, the magnitude of strain estimated by the expression proposed by Carter and Hayes is overstimated. Therefore, the estimation must be between these two equations. This constitutive model suggested by Austman et al. [2008] as follows

$$E_A(\rho) = 8346\ \rho^{1.5}. \tag{3.102}$$

In the following, Lutz and Nackenhorst [2011] developed the constitutive model

$$E_L(\rho) = 6500\ \frac{N}{mm^2}\ \left(\frac{\rho}{\rho_0}\right)^2, \tag{3.103}$$

with $\rho_0 = 1g/cm^3$. These constitutive relationships are compared in Fig.3.4. Furthermore, the finite element simulation results with regard to aforementioned constitutive laws have been compared with the experimental results. The results are illustrated by means of mean square error in table 3.1. It can be found that the equations 3.100 and 3.101 have relatively large deviations from the experimental results.

The equation proposed by Austman is much better, but there is still higher error compared with material law developed by Lutz and Nackenhorst. By these assumptions the strain energy density takes the form

$$\psi_{mech} = \frac{1}{2\rho_0}\varepsilon\left(\frac{\rho}{\rho_0}\right)^{(n-1)} C_0\varepsilon\ . \tag{3.104}$$

Sample test	Carter & Hayes	Morgan u.a.	Austman u.a.	Lutz & Nackenhorst
4	119.7	43.4	36.3	30.5
6	48.3	73.4	26.5	32.3
8	55.1	46.5	20.3	13.7
∅	74.4	54.4	27.7	25.5

Table 3.1: Mean square error between the simulation and experimental results, Lutz and Nackenhorst [2011].

From thermodynamic continuum constitutive theory it is concluded that equation (3.104) should be linear in ρ, hence the exponent value has to be n=2, c.p. Krstin et al. [2000].

Electrical Stimulus

In addition to the mechanical stimulus a constitutive description has to be provided to express the bioelectrical properties of bone tissues. Gauss and Faraday laws for the electrostatic field are written as

$$div(\boldsymbol{D}) = 0, \tag{3.105}$$

$$\boldsymbol{E} = -grad\ \phi, \tag{3.106}$$

where the electric displacement, the electric field and the electric potential are denoted by $\boldsymbol{D}$, $\boldsymbol{E}$ and ϕ, respectively. The electric displacement D is associated to a free energy density function with regard to the electric field E

$$\boldsymbol{D} = \rho \frac{\partial \psi_{elec}}{\partial \boldsymbol{E}} \ . \tag{3.107}$$

The free energy density function depends on the electric field and an internal variable associated to bone mineral density

$$\psi_{elec} = \psi_{elec}(\boldsymbol{E}, \rho) \ . \tag{3.108}$$

The electrical energy density is determined in terms of an electrical stimulus in the process of bone remodeling which can be written in dependency of dielectric constant ϵ and the electric field E,

$$\psi_{elec} = \frac{1}{2\rho} \epsilon(\rho, f) \boldsymbol{E}^2 \ . \tag{3.109}$$

Dielectric constants are quantities which indicate how much charge distribution can be polarized in the presence of an electric field. Dielectric properties

of bone tissue are described in dependency of frequency f and bone mineral density, c.p. Sierpowska et al. [2003]. Strong frequency-dependent correlations have been reported by Sierpowska et al. [2005]; Gabriel et al. [1996] between the electrical characteristics and the density of trabecular bone. The electric permittivity in function of bone mineral density and frequency is illustrated in Fig. 3.5.

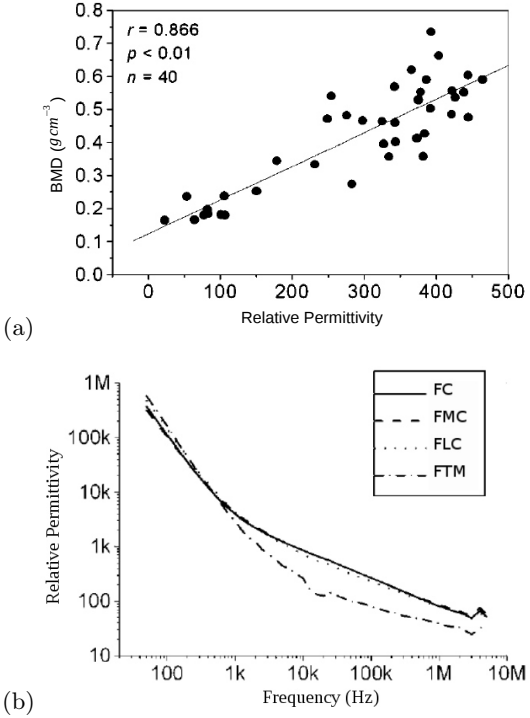

Figure 3.5: Bone density as a function of the relative permittivity (a), relative permittivity (dimensionless) as a function of frequency for various densities of bone tissue (b) (FC: Femoral head; FMC: femoral medial condyle, FLC: femoral lateral condyle and FTM: femoral greater trochanter.), Sierpowska et al. [2003].

The linear permittivity of a homogeneous material can be written with reference to vacuum as a relative permittivity ϵ_r. The actual permittivity is then

calculated by multiplying the relative permittivity with ϵ_0

$$\epsilon(\rho, f) = \epsilon_0 \epsilon_r(\rho, f) \ , \tag{3.110}$$

where $\epsilon_0 = 8.85 \times 10^{-12} F/m$ is the vacuum permittivity. An essential ingredient of electrically driven bone remodeling theories is a constitutive relation between the bone mineral density and electrical properties. The relative permittivity is written in dependecy of bone mineral density and frequency as

$$\epsilon_r(\rho, f) = \epsilon_p (\frac{\rho}{\rho_0})^m + \delta(f) \ . \tag{3.111}$$

Here ϵ_p is a constant for the power model of relative permittivity in dependency of bone density and $\delta(f)$ is a function of frequency which can be provided based on experimental data reported in Sierpowska et al. [2003]. Thus, the electrical energy density can be re-written as

$$\psi_{elec} = \frac{1}{2\rho_0} \epsilon_0 (\epsilon_P (\frac{\rho}{\rho_0})^{m-1} + (\frac{\rho}{\rho_0})^{-1} \delta(f)) E^2 \ . \tag{3.112}$$

Similarly to the arguments on the mechanical stimulation it is assumed that the exponent takes a value $m = 2$, which is in good agreement with experimental observations, e.g. Sierpowska et al. [2003].

3.5.2 Osseointegration at the Bone-dental Implant Interface

Osseointegration is described similarly as the fracture healing process of bone Kienapfel et al. [1999]. After surgery a thin bone-implant interface layer consisting of a mixture of blood and mushy bone phase develops surrounding dental prosthesis, which is quite soft and nearly incompressible.

Lutz and Nackenhorst [2011] introduced a modified Drucker-Prager plasticity model based on the mechanical properties of a thin bone-implant interface layer which has been implemented into a finite element framework. In the limit case of vanishing layer thickness this modeling approach has been interpreted as a weak form of frictional contact formulation. The Drucker-Prager yield criterion reads

$$f = \parallel \tilde{\boldsymbol{\sigma}} \parallel - \sqrt{2}(c - \alpha p) \leq 0 \ , \tag{3.113}$$

where $\tilde{\sigma}$ represents the deviatoric part of stress tensor, c is an adhesion parameter, α is the friction coefficient and p denotes the hydrostatic pressure. In order to mimic the osseointegration process, this initial yield criterion applied for the thin interface layer is modified as

$$f_{mod} = \parallel \tilde{\boldsymbol{\sigma}} \parallel - \sqrt{2}(c - \alpha p)(1 - \xi) - \sqrt{\frac{2}{3}} \sigma_F \xi \leq 0 \ . \tag{3.114}$$

Here, σ_F describes the yield strength and ξ an osseointegration variable is introduced

$$\xi = \frac{\rho - \rho_{min}}{\rho_{max} - \rho_{min}} \in [0, 1], \tag{3.115}$$

where ρ_{min} and ρ_{max} describe the minimum and maximum values of bone mineral density. It is easily seen that this representation of the yield surface describes a smooth transition from Drucker-Prager model to von Mises yield surface, c.p. Figure 3.6. In addition, the radius of the yield surface in deviatoric planes is shown in Figure 3.6 (b) for Drucker-Prager model $\sqrt{2}(c - \alpha p)$ and von Mises $\sqrt{\frac{2}{3}}\sigma_F$.

Since Poisson's ratio decreases during osseointegration process when the interface layer transition from a rather liquid phase to solid bone, Poisson's ratio is modeled by a functional dependency of osseointegration degree as

$$\nu = \nu_{max} - \xi(\nu_{max} - \nu_{min}) \,, \tag{3.116}$$

where ν_{max} and ν_{min} represent the value of Poisson's ratio of bone in post-operative and osseointegrated constitution, respectively.

The evolution equation for the plastic deviatoric strain, which here should be interpreted as relative tangential movement of host bone and implant during dynamic loading, is determined from a non-associated flow rule, i.e.

$$\dot{\tilde{\boldsymbol{\varepsilon}}}^{pl} = \dot{\lambda}\frac{\partial f_{mod}}{\partial \tilde{\boldsymbol{\sigma}}} = \dot{\lambda}\frac{\partial \parallel \tilde{\boldsymbol{\sigma}} \parallel}{\partial \tilde{\boldsymbol{\sigma}}} = \dot{\lambda}\boldsymbol{n}, \tag{3.117}$$

with the plastic multiplier λ and flow direction $\boldsymbol{n} = \frac{\tilde{\boldsymbol{\sigma}}}{\|\tilde{\boldsymbol{\sigma}}\|}$.

Well established radial return mapping scheme is applied for the temporal integration of the plastic strains, i.e. the tangential micromotion between implant and host bone. Following the procedure outlined in Lutz and Nackenhorst [2011], the trial stress state or elastic predictor which implies the trial state of yield criterion reads

$$\tilde{\boldsymbol{\sigma}}^{tr}_{n+1} = 2\mu(\tilde{\boldsymbol{\varepsilon}}_{n+1} - \tilde{\boldsymbol{\varepsilon}}^{pl}_{n}) \,, \tag{3.118}$$

$$f^{tr}_{n+1} = \parallel \tilde{\boldsymbol{\sigma}}^{tr}_{n+1} \parallel - \sqrt{2}(c - \alpha p)(1 - \xi) - \sqrt{\frac{2}{3}}\sigma_F \xi \leq 0 \,. \tag{3.119}$$

Herein μ represents shear modulus. The invalid trial stress is corrected and projected back to the yield surface as

$$\tilde{\boldsymbol{\sigma}}_{n+1} = \tilde{\boldsymbol{\sigma}}^{tr}_{n+1} - 2\mu\Delta\lambda\boldsymbol{n}_{n+1} \,, \tag{3.120}$$

$$\parallel \tilde{\boldsymbol{\sigma}}_{n+1} \parallel = \parallel \tilde{\boldsymbol{\sigma}}^{tr}_{n+1} \parallel - 2\mu\Delta\lambda \,. \tag{3.121}$$

The plastic multiplier $\Delta\lambda$ is obtained by inserting equation (3.121) into the yield function at step $n + 1$,

$$f_{n+1} = f^{tr}_{n+1} - 2\mu\Delta\lambda \stackrel{!}{=} 0 \,, \tag{3.122}$$

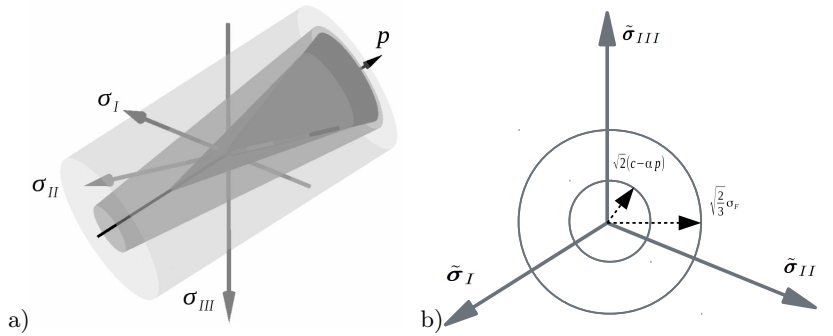

Figure 3.6: Illustration of Drucker-Prager yield surface converts into von Mises model: (a) principal stress space and (b) deviatoric planes.

i.e.

$$\Delta\lambda = \frac{f_{n+1}^{tr}}{2\mu} \,. \tag{3.123}$$

The algorithmic consistent tangent operator has been derived in order to certify the quadratic convergence of the Newton-Raphson scheme which is applied for the solution of the linearized equilibrium equation. The deviatoric part of the elasto-plastic tangent operator is written

$$\begin{aligned} \widetilde{\mathbb{C}}^{ep} &= \frac{\partial \tilde{\boldsymbol{\sigma}}_{\mathrm{n+1}}}{\partial \tilde{\boldsymbol{\varepsilon}}_{\mathrm{n+1}}} \\ &= 2\mu \, \frac{\partial}{\partial \tilde{\boldsymbol{\varepsilon}}_{\mathrm{n+1}}} \left(\tilde{\boldsymbol{\varepsilon}}_{\mathrm{n+1}} - \tilde{\boldsymbol{\varepsilon}}_{\mathrm{n}}^{\mathrm{pl}} - \Delta\lambda \, \boldsymbol{n}_{\mathrm{n+1}} \right) \\ &= 2\mu \, \left(\mathbb{I} - \frac{\partial \, \Delta\lambda}{\partial \tilde{\boldsymbol{\varepsilon}}_{\mathrm{n}} 1} \otimes \boldsymbol{n}_{\mathrm{n+1}} - \Delta\lambda \frac{\partial \boldsymbol{n}_{\mathrm{n+1}}}{\partial \tilde{\boldsymbol{\varepsilon}}_{\mathrm{n+1}}} \right) \,. \end{aligned} \tag{3.124}$$

The derivative of the normal $\boldsymbol{n}_{n+1}$ can be calculated using chain rules

$$\frac{\partial \boldsymbol{n}_{\mathrm{n+1}}}{\partial \tilde{\boldsymbol{\varepsilon}}_{\mathrm{n+1}}} = \frac{\partial \boldsymbol{n}_{n+1}^{tr}}{\partial \tilde{\boldsymbol{\varepsilon}}_{\mathrm{n+1}}} = \frac{\partial \boldsymbol{n}_{n+1}^{tr}}{\partial \tilde{\boldsymbol{\sigma}}_{n+1}^{tr}} \, \frac{\partial \tilde{\boldsymbol{\sigma}}_{n+1}^{tr}}{\partial \tilde{\boldsymbol{\varepsilon}}_{\mathrm{n+1}}} \tag{3.125}$$

with

$$\begin{aligned} \frac{\partial \boldsymbol{n}_{n+1}^{tr}}{\partial \tilde{\boldsymbol{\sigma}}_{n+1}^{tr}} &= \frac{\partial (\frac{\tilde{\boldsymbol{\sigma}}_{n+1}^{tr}}{||\tilde{\boldsymbol{\sigma}}_{n+1}^{tr}||})}{\tilde{\boldsymbol{\sigma}}_{n+1}^{tr}} = \frac{\mathbb{I}||\tilde{\boldsymbol{\sigma}}_{n+1}^{tr}|| - \boldsymbol{n}_{n+1}^{tr} \tilde{\boldsymbol{\sigma}}_{n+1}^{tr}}{(||\tilde{\boldsymbol{\sigma}}_{n+1}^{tr}||)^2} \\ &= \frac{1}{||\tilde{\boldsymbol{\sigma}}_{n+1}^{tr}||} \left(\mathbb{I} - \boldsymbol{n}_{n+1}^{tr} \otimes \boldsymbol{n}_{n+1}^{tr} \right) , \end{aligned} \tag{3.126}$$

and

$$\frac{\partial \tilde{\boldsymbol{\sigma}}^{tr}_{n+1}}{\partial \tilde{\boldsymbol{\varepsilon}}_{\mathrm{n+1}}} \;=\; 2\mu. \tag{3.127}$$

The derivative of the normal $\boldsymbol{n}_{n+1}$ is obtained

$$\frac{\partial \boldsymbol{n}_{\mathrm{n+1}}}{\partial \tilde{\boldsymbol{\varepsilon}}_{\mathrm{n+1}}} \;=\; \frac{2\mu}{||\tilde{\boldsymbol{\sigma}}^{tr}_{n+1}||}\left(\mathbb{I} - \boldsymbol{n}^{tr}_{n+1}\otimes \boldsymbol{n}^{tr}_{n+1}\right). \tag{3.128}$$

The derivative $\Delta\lambda$ is calculated as

$$\begin{aligned}
\frac{\partial\,\Delta\lambda}{\partial\,\tilde{\boldsymbol{\varepsilon}}_{\mathrm{n+1}}} \;&=\; \frac{\partial}{\partial\,\tilde{\boldsymbol{\varepsilon}}_{\mathrm{n+1}}}\;\frac{1}{2\mu}\left(\parallel \tilde{\boldsymbol{\sigma}}^{tr}_{n+1} \parallel - \sqrt{2}(c-\alpha p^{tr})(1-\xi) - \sqrt{\frac{2}{3}}\sigma_F\xi\right)\\
&=\; \frac{\partial}{\partial\,\tilde{\boldsymbol{\varepsilon}}_{\mathrm{n+1}}}\;\frac{1}{2\mu}\left(||\tilde{\boldsymbol{\sigma}}^{tr}_{n+1}|| + \sqrt{2}\alpha(1-\xi)\;\frac{1}{3}\mathrm{tr}(\boldsymbol{\sigma}^{tr}_{n+1})\right)\\
&=\; \frac{1}{2\mu}\left(\frac{\partial\,||\tilde{\boldsymbol{\sigma}}^{tr}_{n+1}||}{\partial\,\tilde{\boldsymbol{\sigma}}_{\mathrm{n+1}}}\;\frac{\partial\,\tilde{\boldsymbol{\sigma}}_{\mathrm{n+1}}}{\partial\,\tilde{\boldsymbol{\varepsilon}}_{\mathrm{n+1}}} \;+\; \frac{\sqrt{2}}{3}\alpha(1-\xi)\,\mathbf{1}\cdot\cdot\frac{\partial\,\boldsymbol{\sigma}^{tr}_{n+1}}{\partial\,\tilde{\boldsymbol{\varepsilon}}_{\mathrm{n+1}}}\right).
\end{aligned} \tag{3.129}$$

The derivative of two more term is drived with

$$\begin{aligned}
\frac{\partial\,||\tilde{\boldsymbol{\sigma}}^{tr}_{n+1}||}{\partial\,\tilde{\boldsymbol{\sigma}}_{\mathrm{n+1}}}\;\frac{\partial\,\tilde{\boldsymbol{\sigma}}_{\mathrm{n+1}}}{\partial\,\tilde{\boldsymbol{\varepsilon}}_{\mathrm{n+1}}} \;&=\; \frac{\tilde{\boldsymbol{\sigma}}^{tr}_{n+1}}{||\tilde{\boldsymbol{\sigma}}^{tr}_{n+1}||}\cdot\cdot 2\mu\left(\frac{\partial\,\tilde{\boldsymbol{\varepsilon}}_{\mathrm{n+1}}}{\partial\,\tilde{\boldsymbol{\varepsilon}}_{\mathrm{n+1}}} - \frac{\partial\,\tilde{\boldsymbol{\varepsilon}}^{\mathrm{pl}}_{\mathrm{n}}}{\partial\,\tilde{\boldsymbol{\varepsilon}}_{\mathrm{n+1}}}\right)\\
&=\; 2\mu\,\boldsymbol{n}^{tr}_{n+1}
\end{aligned} \tag{3.130}$$

and

$$\begin{aligned}
\frac{\partial\,\boldsymbol{\sigma}^{tr}_{n+1}}{\partial\,\tilde{\boldsymbol{\varepsilon}}_{\mathrm{n+1}}} \;&=\; \frac{\partial}{\partial\,\tilde{\boldsymbol{\varepsilon}}_{\mathrm{n+1}}}\left[\kappa\left(\mathrm{tr}(\boldsymbol{\varepsilon}^{vol}_{n+1}+\tilde{\boldsymbol{\varepsilon}}_{\mathrm{n+1}})\right)\mathbf{1} \;+\; 2\mu\left(\tilde{\boldsymbol{\varepsilon}}_{\mathrm{n+1}} - \tilde{\boldsymbol{\varepsilon}}^{\mathrm{pl}}_{\mathrm{n}}\right)\right]\\
&=\; \frac{\partial}{\partial\,\tilde{\boldsymbol{\varepsilon}}_{\mathrm{n+1}}}\left[\kappa\left(\mathrm{tr}(\tilde{\boldsymbol{\varepsilon}}_{\mathrm{n+1}})\right)\;\mathbf{1} \;+\; 2\mu\,\tilde{\boldsymbol{\varepsilon}}_{\mathrm{n+1}}\right]\\
&=\; \kappa\mathbf{1}\otimes\mathbf{1} \;+\; 2\mu\,\mathbb{I} \;=\; \mathbb{C}^{el}\;,
\end{aligned} \tag{3.131}$$

which κ is Bulk modulus, $\mathbb{C}^{el}$ denotes linear elastic material tensor with regard to trial stress state and $.^{vol}$ represent volumetric part of the tensors. Now the derivative $\Delta\lambda$ is rewritten as

$$\begin{aligned}
\frac{\partial\,\Delta\lambda}{\partial\,\tilde{\boldsymbol{\varepsilon}}_{\mathrm{n}}1} \;&=\; \frac{1}{2\mu}\left(2\mu\,\boldsymbol{n}^{tr}_{n+1} \;+\; \frac{\sqrt{2}}{3}\alpha(1-\xi)\,\mathbf{1}\cdot\cdot\mathbb{C}^{el}\right)\\
&=\; \boldsymbol{n}^{tr}_{n+1} \;+\; \frac{1}{3\sqrt{2}\mu}\;\alpha(1-\xi)\,\mathbf{1}\cdot\cdot\mathbb{C}^{el}
\end{aligned} \tag{3.132}$$

Finally, the deviatoric part of the elasto-plastic tangent operator reads

$$\widetilde{\mathbb{C}}^{ep} = 2\mu \left(\mathbb{I} - \left[\boldsymbol{n}^{tr}_{n+1} + \frac{1}{3\sqrt{2}\mu} \alpha(1-\xi)\, \mathbf{1} \cdot\cdot \mathbb{C}^{el} \right] \otimes \boldsymbol{n}^{tr}_{n+1} - \frac{2\mu\Delta\lambda}{||\tilde{\boldsymbol{\sigma}}^{tr}_{n+1}||} \left[\mathbb{I} - \boldsymbol{n}^{tr}_{n+1} \otimes \boldsymbol{n}^{tr}_{n+1} \right] \right) \tag{3.133}$$

The complete elasto-plastic tangent operator consist of volumetric and deviatoric part is written as

$$\mathbb{C}^{ep} = \mathbb{C}^{el}_{vol} + \widetilde{\mathbb{C}}^{ep} \cdot\cdot \mathbb{P} = \kappa \mathbf{1} \otimes \mathbf{1} + 2\mu \left(\tilde{C}^{ep}_{vM} - (1-\xi) \widehat{\boldsymbol{n}} \otimes \boldsymbol{n}^{tr}_{n+1} \right) , \tag{3.134}$$

in which deviatoric von Mises elasto-plastic tangent is written as

$$\tilde{\mathbb{C}}^{ep}_{vM} = \left[1 - \Delta\lambda \frac{2\mu}{\| \tilde{\sigma}_{n+1} \|} \right] \left[\mathbb{P} - \boldsymbol{n}^{tr}_{n+1} \otimes \boldsymbol{n}^{tr}_{n+1} \right] , \tag{3.135}$$

with the projection tensor

$$\mathbb{P} = \mathbb{I} - \frac{1}{3} \mathbf{1} \otimes \mathbf{1}, \tag{3.136}$$

and the abbreviation

$$\widehat{\boldsymbol{n}} = \frac{1}{3\sqrt{2}\mu} \alpha(1-\xi) \mathbf{1} \cdot\cdot \mathbb{C}^{el} . \tag{3.137}$$

In the case of detachment within the interface, the stress state is projected onto the apex of the yield surface,

$$\boldsymbol{\sigma}_{apex} = \frac{1}{\alpha(1-\xi)} [c(1-\xi) + \frac{1}{\sqrt{3}} \sigma_F \xi] \mathbf{1} , \tag{3.138}$$

with the second order unit tensor $\mathbf{1}$. In this case the corresponding tangent operator is equal to zero,

$$\mathbb{C}^{apex}_{n+1} = \mathbb{O} . \tag{3.139}$$

3.6 Phenomenological Behavior of Piezoelectric Materials

The purpose of this section is to present a general framework for the analysis and design of engineering systems that incorporate piezoelectric materials. Some general information about piezoelectric materials are reviewed, how do they work?, how are they made?. The piezoelectric effect were first discovered in 1880 by Jacques and Pierre Curie. They found out that when a mechanical stress is applied on these materials, electricity is produced and the magnitude of electric potential is proportional to the stress. The inverse effect was discovered one year later through the mathematical aspect of the theory.

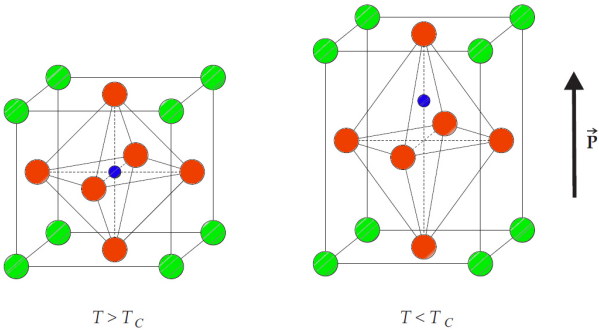

Figure 3.7: Crystal structure of perovskite: no piezoelectric effect ($T > T_C$), piezoelectric effect ($T < T_C$).

The discovery of piezoelectricity caused significant interest within the European scientific community. These materials were applied for the first time during the World War I with piezoelectric ultrasonic transducers. Nowadays, piezoelasticity is widely used in everyday life, for instance, car's airbag sensor, cell phones, printers and medical devices.

The nature of piezoelectric materials is connected to the substantial quantity of electric dipoles within these materials. The dipole vector $\vec{P}$ has a direction and a value in dependency with the electrical charges around. Piezoelectric materials can be natural or man-made. The most well known natural piezoelectric material is quartz, but manufactured piezoelectric materials are more applicable and mostly ceramics. The phenomenon of piezoelectricity occurs in dielectric materials, for which the unit cell is asymmetric. This commonly introduced by crystalline structures.

There are 32 crystal classes in nature, from which only 20 of them possess the piezoelectric requirements. A piezoelectric ceramic is a mass of perovskite crystals which can be produced under poling process. Some typical piezoelectric ceramics are made by poling, e.g. lead-zirconate-titanate (Pb(Zr,Ti)O3) called PZT, lead-titanate (PbTiO2), lead-zirconate (PbZrO3) and barium-titanate (BaTiO3). Electroactive polymers (EAP) are another group of piezoelectric materials from which the most important one is polyvinylidine flouride (PVDF). Piezo technology is extensively used in cutting edge technology such as medical technology, mechanical and automotive engineering or semiconductor technology.

In order to utilize the piezoelectric effect in medical devices it is necessary to gain deeper chemical insight into the piezoelectric structure. First the behaviour of the material on a microscopic scale should be considered. The unit

cell transforms to different geometries depending on temperature. A critical temperature is defined, called Curie temperature T_c. Above the Curie temperature ($T > T_c$) the unit cell is in the cubic phase and no piezoelectric effect is observed, as demonstrated in Fig. 3.7.

However, the electric dipole moment occurs when the temperature is lower than the Curie temperature ($T < T_c$). A region of local alignment is formed by adjoining dipoles which are called Weiss domains. It should be noted that the direction of polarization among polar domains is random, as illustrated in Fig. 3.8 (a). DC electric field is applied in order to align the domain, which is referred to as the poling process (Fig. 3.8 (b)). After the poling treatment, the

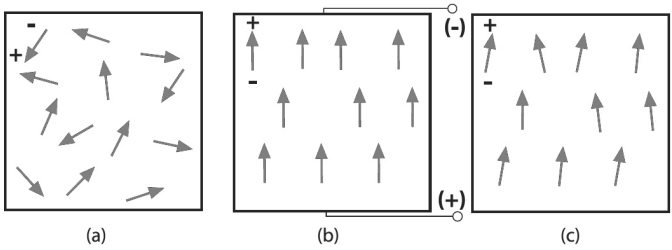

Figure 3.8: (a) Random polar domain, (b) aligned polarization direction under DC electric field, (c) removed electric field and locked dipoles.

electric field is removed and dipoles remain in line with the polarization direction (Fig. 3.8 (c)). Now a permanent polarization exists in the piezoelectric element.

3.6.1 Piezoelectric Effects

Polarization in piezoelectric materials can be induced not only by an electric field, but also by application of mechanical loads. Mechanical stresses on a poled piezoelectric element can change the dipole moment which leads to the generation of a potential difference. This effect is referred to direct or generator effect in the literature.

Properties of a poled piezoelectric element can be described with regard to mechanical loading and polarization direction. Compression parallel to polarization direction, or tension in a transverse direction of the polarization, generates an electric field $\boldsymbol{E}$ in parallel to polarization direction (Fig. 3.9 (a)

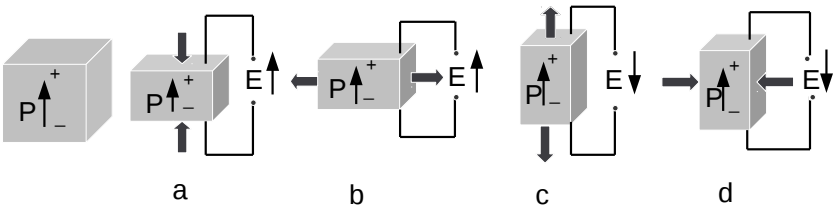

Figure 3.9: Reaction of a poled piezoelectric element under compression and tension.

and (b)). Tension parallel to polarization direction, or compression in a transverse direction of the polarization, generates an electric field perpendicular to the polarization direction (Fig. 3.9 (c) and (d)). Conversly, the application of an electric field to a piezoelectric body leads to deformations. This effect is called inverse piezoelectric effect which can be used for various actuator types. Butterfly-shaped curves of the strain-electric-field diagram of piezoelectric material (PZT) is illustrated in Fig. 3.10, which shows in the following steps:

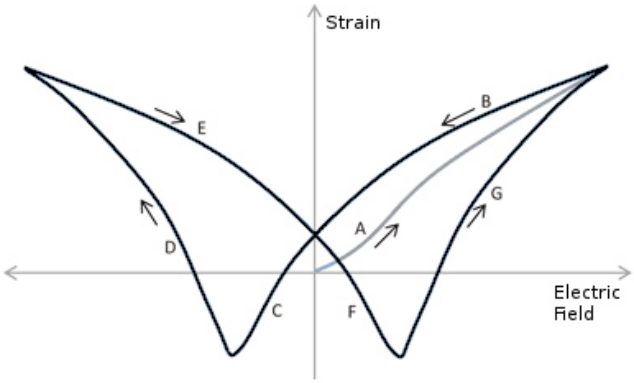

Figure 3.10: Butterfly-shaped curves of the strain-electric-field diagram of piezoelectric material

A: The strain increases with electric field and the nonlinear behaviour can be observed for high intensity of the electric field $\boldsymbol{E}$. Therefore, the linear behavior of strain field takes place only for low values of $\boldsymbol{E}$.

B: The material remains in the new direction of polarization when the strain decreases with the electric field.

C: The original orientation of dipoles is gradually reversed as the electric field becomes negative. When they completely reverse the direction, the material is polarized in the opposite direction. The electric field at the point of reversed polarization is known as the coercive field.

D: The piezo material expands again, after polarization reversal, until the physical strain limit.

E: The same hysteretic behavior along curve B takes place when the electric field is reversed.

F: The dipoles reorient again to their original polarization as the electric field reaches the coercive limit.

G: The strain increases with the applied electric field to its physical limit.

3.7 Piezoelectric Constitutive Equations

In this section constitutive equations are introduced which describe electromechanical properties of piezoelectric materials. Piezoelectric materials behave linearly at low electric fields and at low mechanical stress levels. However, they may indicate nonlinearity at high electric field or high mechanical stress level.

In this study we restrict ourselves to a linear first order modeling approach. The total free energy for small fields is introduced in the form

$$W = \frac{1}{2}\varepsilon_{ij}\varepsilon_{kl}C_{ijkl} - \frac{1}{2}E_iE_k\epsilon_{ik} - \varepsilon_{kl}E_ie_{ikl} \ . \tag{3.140}$$

The material constants in the constitutive matrices read, Yang [2005a]

$$C_{ijkl} = \frac{\partial^2 W}{\partial\varepsilon_{ij}\partial\varepsilon_{kl}} = \frac{\partial\sigma_{ij}}{\partial\varepsilon_{kl}} \ , \tag{3.141}$$

$$e_{ikl} = -\frac{\partial^2 W}{\partial\varepsilon_{ij}\partial E_i} = \frac{\partial D_i}{\partial\varepsilon_{kl}} = -(\frac{\partial\sigma_{ik}}{\partial E_l})^T \ , \tag{3.142}$$

$$\epsilon_{ik} = -\frac{\partial^2 W}{\partial E_i\partial E_k} = \frac{\partial D_k}{\partial E_i} \ . \tag{3.143}$$

The final form of linear constitutive equations for both converse and direct piezoelectric effects are expressed by

$$\sigma_{ij} = C^E_{ijkl}\varepsilon_{kl} - e_{kij}E_k \tag{3.144}$$

$$D_i = e_{ikl}\varepsilon_{kl} + \epsilon^s_{ij}E_j \ , \tag{3.145}$$

where C^E_{ijkl} is the elastic stiffness tensor at constant electric field, e_{kij} is the piezoelectric stress constant and ϵ^s_{ij} is the dielectric permittivity tensor at constant strain. The indexes $i, j = 1, 2, 3$ and $l, k = 1, 2, 3$ refer to different directions within the material coordinate system. Due to the symmetries of the strain and stress tensor, one can deduce

$$\begin{aligned} C^E_{ijkl} &= C^E_{jikl} \\ C^E_{ijkl} &= C^E_{jilk} \\ C^E_{ijkl} &= C^E_{klij} \\ e_{kij} &= e_{kji} \\ \epsilon^s_{ij} &= \epsilon^s_{ji} \end{aligned} \tag{3.146}$$

Since the piezoelectric layer is assumed as transversely isotropic material and is poled along the thickness, many of the parameters in the above constants matrices will be either zero, or can be expressed in terms of other parameters. subsequently, in matrix form, can be written as

$$C^E = \begin{bmatrix} C^E_{11} & C^E_{12} & C^E_{13} & 0 & 0 & 0 \\ C^E_{12} & C^E_{11} & C^E_{13} & 0 & 0 & 0 \\ C^E_{13} & C^E_{13} & C^E_{33} & 0 & 0 & 0 \\ 0 & 0 & 0 & C^E_{44} & 0 & 0 \\ 0 & 0 & 0 & 0 & C^E_{44} & 0 \\ 0 & 0 & 0 & 0 & 0 & \frac{1}{2}(C^E_{11} - C^E_{12}) \end{bmatrix} \tag{3.147}$$

$$e = \begin{bmatrix} 0 & 0 & 0 & 0 & e_{15} & 0 \\ 0 & 0 & 0 & e_{15} & 0 & 0 \\ e_{31} & e_{31} & e_{33} & 0 & 0 & 0 \end{bmatrix} \tag{3.148}$$

$$\epsilon^s = \begin{bmatrix} \epsilon^s_{11} & 0 & 0 \\ 0 & \epsilon^s_{22} & 0 \\ 0 & 0 & \epsilon^s_{33} \end{bmatrix} \tag{3.149}$$

Here e_{31} represents the transversal effect when the loading direction is perpendicular to the polarization direction. The longitudinal effect is represented by e_{33} if loading is applied parallel to polarization direction and constant e_{15} is related to shear effect. Thus the number of piezoelectric stress constant reduces to three independent variables which characterize the longitudinal, transversal and shear effects.

The constitutive equations, 3.144 and 3.145, can be rewritten in a matrix notation

$$\boldsymbol{\varepsilon} = S^E\boldsymbol{\sigma} + d\boldsymbol{E} \tag{3.150}$$

$$\boldsymbol{D} = d\boldsymbol{\sigma} + \epsilon^{\sigma}\boldsymbol{E}. \tag{3.151}$$

where S^E is compliance tensor at constant electric field, d is piezoelectric strain constant and ϵ^{σ} is dielectric permittivity tensor at constant stress. The first equation indicates that part of a mechanical strain applied to the material is transformed to electrical field. Likewise, the second one shows that part of an electrical field applied to the material is transformed into mechanical stress. The first equation in the absence of electric field $\boldsymbol{E}$ takes the form $\boldsymbol{\varepsilon} = S^E\boldsymbol{\sigma}$ which is Hooke's Law. Similarly, in the absence of mechanical stress the second equation describes the pure electrical behaviour of the material. The effectiveness indicator of the energy conversion for both direct and convers piezoelectric effect is described by an electromechanical coupling coefficient K

$$K = \frac{U_c}{\sqrt{U_m U_e}}, \tag{3.152}$$

with

$$U_m = \frac{1}{2}S^E\boldsymbol{\sigma}^2, \tag{3.153}$$

$$U_e = \frac{1}{2}\epsilon^{\sigma}\boldsymbol{E}^2 \tag{3.154}$$

and

$$U_c = \frac{1}{2}\boldsymbol{\sigma}d\boldsymbol{E}. \tag{3.155}$$

Where U_m is mechanical energy, U_e is electric energy and U_c represent coupling energy. Electromechanical coupling coefficient can be rewritten

$$k^2 = \frac{d^2}{S^E\epsilon^{\sigma}}\ . \tag{3.156}$$

It should be noted that other formulations of the constitutive equations can be written, e.g.

$$\boldsymbol{\varepsilon} = S^D\boldsymbol{\sigma} + g\boldsymbol{D} \tag{3.157}$$

$$\boldsymbol{E} = -g\boldsymbol{\sigma} + \beta^{\sigma}\boldsymbol{D}, \tag{3.158}$$

or

$$\boldsymbol{\sigma} = C^D\boldsymbol{\varepsilon} - h\boldsymbol{D} \tag{3.159}$$

$$\boldsymbol{E} = -h\boldsymbol{\varepsilon} + \beta^s\boldsymbol{D}, \tag{3.160}$$

where C and S are matrices with elasticity constants, ϵ and β matrices with dielectric constants, d, e, g and h are matrices with piezoelectric constants. The relationships between dielectric, elastic, and piezoelectric constants can

be retrieved

$$[C^E][S^E] = [C^D][S^D] \tag{3.161}$$
$$[\beta^s][\epsilon^s] = [\beta^\sigma][\epsilon^\sigma] \tag{3.162}$$
$$[C^D] = [C^E] + [e][h] \tag{3.163}$$
$$[S^D] = [S^E] - [d][g] \tag{3.164}$$
$$[\epsilon^\sigma] = [\epsilon^s] + [d][e] \tag{3.165}$$
$$[\beta^\sigma] = [\beta^s] - [g][h] \tag{3.166}$$
$$[e] = [d][C^E] \tag{3.167}$$
$$[d] = [\epsilon^\sigma][g] \tag{3.168}$$
$$[g] = [h][S^D] \tag{3.169}$$
$$[h] = [\beta^S][e] \tag{3.170}$$

These alternative forms for the constitutive relations of piezoelectric materials are particularly applicable in order to estimate or measure a specific quantity in special conditions, at zero stress or zero electric field.

4 Finite Element Modeling of Electro-Mechanical Coupling

From the mathematical point of view, the Finite Element Method (FEM) is a numerical procedure in order to solve the partial differential equations of physical systems. Since exact analytic solution due to the complexity of the boundary conditions are only possible for limited cases, numerical methods such as the FEM aim to provide an approximation to solve the problem.

In this chapter, the formulation of a finite element approach for the analysis of piezoelectric materials is briefly explained. The finite element formulation is derived consistently from virtual work principle by formulating appropriate electrical, mechanical and coupling potentials. In a first step, variational principle are introduced. In the following, the typical finite element discretization for the electrostatic and mechanical field equations is outlined. The straightforward solution is considered for the linear case, while an incremental procedure is required for the nonlinear case. In a subsequent step, a piezoelectric patch test is investigated in order to verify numerical results.

For more detailed and in-depth expressions, the interested reader may consult Bathe [2001]; Wriggers [2009]; Zienkiewicz et al. [2005]; Gaudenzi [2009].

4.1 Variational Principles

In order to determine a finite element formulation for a boundary value problem, a variational formulation is derived which can be interpreted as a weak form of equilibrium. The principle of virtual work for instance provides a variational principle for displacement-based finite element formulations in structural mechanics. The principle of virtual work states that"a structure is in equilibrium under a set of external loads if after imposing to the structure arbitrary (virtual) displacements compatible with the boundary conditions, the work performed by the external loads on the virtual displacements equals the work performed by the actual stresses on the strains induced by the virtual displacements". In the context of electromechanical problems, besides to virtual displacements $\delta\boldsymbol{u}$ the virtual potential $\delta\boldsymbol{\phi}$ have to be considered. The

total boundary value problem for a static mechanical problem is described by

$$\begin{aligned} \operatorname{div}\boldsymbol{\sigma} &= \mathbf{0} && \text{in } \mathcal{B}, \\ \boldsymbol{t} = \boldsymbol{\sigma}\cdot\boldsymbol{n} &= \bar{\boldsymbol{t}} && \text{on } \partial_t\mathcal{B}, \ (\textit{Natural B.C.}) \\ \boldsymbol{u} &= \bar{\boldsymbol{u}} && \text{on } \partial_u\mathcal{B}, \ (\textit{Essential B.C.}) \end{aligned} \tag{4.1}$$

with boundary conditions on the surface $\partial\mathcal{B}$ and neglecting volume forces. From the conservation law of equations 3.92 and Natural boundary conditions $\boldsymbol{t}$ the equation of virtual work for every possible choice of the virtual displacements $\delta\boldsymbol{u}$ can be derived as follows

$$\int_{\mathcal{B}} \operatorname{div}(\boldsymbol{\sigma})\cdot\delta\boldsymbol{u}\,\mathrm{d}V + \int_{\partial\mathcal{B}} (\boldsymbol{t}-\boldsymbol{\sigma}\cdot\boldsymbol{n})\cdot\delta\boldsymbol{u}\,\mathrm{d}a = 0\,. \tag{4.2}$$

Eventually, equation 4.2 is rewritten as

$$\int_{\mathcal{B}} \boldsymbol{\sigma}\cdot\cdot\,\delta\boldsymbol{\varepsilon}\,\mathrm{d}V = \int_{\partial\mathcal{B}} \boldsymbol{t}\cdot\delta\boldsymbol{u}\,\mathrm{d}a\,. \tag{4.3}$$

Similarly, the total boundary value problem for an electrostatic problem is written

$$\begin{aligned} \operatorname{div}\boldsymbol{D} &= \mathbf{0} && \text{in } \mathcal{B}, \\ \boldsymbol{q} = -\boldsymbol{D}\cdot\boldsymbol{n} &= \bar{\boldsymbol{q}} && \text{on } \partial_q\mathcal{B}, \ (\textit{Natural B.C.}) \\ \boldsymbol{\phi} &= \bar{\boldsymbol{\phi}} && \text{on } \partial_\phi\mathcal{B}. \ (\textit{Essential B.C.}) \end{aligned} \tag{4.4}$$

In analogy with the principle of virtual work an equation of virtual electric potential is expressed using equation 3.105 and natural electrical boundary condition for every choice of the virtual electric potential $\delta\boldsymbol{\phi}$

$$\int_{\mathcal{B}} \operatorname{div}(\boldsymbol{D})\cdot\delta\boldsymbol{\phi}\,\mathrm{d}V + \int_{\partial\mathcal{B}} (\boldsymbol{q}-\boldsymbol{D}\cdot\boldsymbol{n})\cdot\delta\boldsymbol{\phi}\,\mathrm{d}a = 0, \tag{4.5}$$

which is reformulated into

$$\int_{\mathcal{B}} \boldsymbol{D}\cdot\delta\boldsymbol{E}\,\mathrm{d}V = -\int_{\partial\mathcal{B}} \boldsymbol{q}\cdot\delta\boldsymbol{\phi}\,\mathrm{d}a\,. \tag{4.6}$$

For the piezoelectric bodies above mechanical and electrical principles are coupled by means of the constitutive relations.

4.2 Finite Element Discretization

In section 3.7, continuum constitutive relations of a piezoelectric material have been derived. Substituting equations 3.144 and 3.145 into equations 4.3 and

4.6, the following set of equations is obtained,

$$\int_{\mathcal{B}} \boldsymbol{\varepsilon}^T \mathbb{C} \boldsymbol{\varepsilon} \, \mathrm{d}V - \int_{\mathcal{B}} \boldsymbol{\varepsilon}^T \boldsymbol{e} \boldsymbol{E} \, \mathrm{d}V = \int_{\partial\mathcal{B}} \boldsymbol{u}^T \boldsymbol{t} \, \mathrm{d}a, \tag{4.7}$$

$$\int_{\mathcal{B}} \boldsymbol{E}^T \boldsymbol{e} \boldsymbol{\varepsilon} \, \mathrm{d}V + \int_{\mathcal{B}} \boldsymbol{E}^T \boldsymbol{\epsilon} \boldsymbol{E} \, \mathrm{d}V = - \int_{\partial\mathcal{B}} \boldsymbol{q} \boldsymbol{\phi} \, \mathrm{d}a. \tag{4.8}$$

The finite element method is utilized to discretize the electrostatic and mechanical field equations simultaneously. In first step, the body of interest is divided into non-overlapping elements n_{el}

$$\mathcal{B} \approx \mathcal{B}_h = \bigcup_{e=1}^{n_{el}} \Omega_e, \tag{4.9}$$

where Ω_e represents each element domain. The position vectors of the material points are discretized as follows

$$\boldsymbol{X}(\boldsymbol{\xi}) \approx \sum_{I=1}^{n_\mathrm{n}} N_I(\boldsymbol{\xi}) \, \boldsymbol{X}_I, \tag{4.10}$$

where the shape functions N_I are defined in terms of coordinates ξ and have to fulfill the geometric constraint

$$\sum_{I=1}^{n_\mathrm{n}} N_I(\boldsymbol{\xi}) \; = 1. \tag{4.11}$$

The electric potential ϕ is introduced as fourth nodal degree of freedom beside the displacement field u in the three spatial directions. For every finite element of the considered body we assume

$$\boldsymbol{u}(\boldsymbol{\xi}) \approx \sum_{I=1}^{n_\mathrm{n}} N_I(\boldsymbol{\xi}) \, \boldsymbol{u}_I \quad , \quad \delta\boldsymbol{u}(\boldsymbol{\xi}) \approx \sum_{I=1}^{n_\mathrm{n}} N_I(\boldsymbol{\xi}) \, \delta\boldsymbol{u}_I \quad , \quad \Delta\boldsymbol{u}(\boldsymbol{\xi}) \approx \sum_{I=1}^{n_\mathrm{n}} N_I(\boldsymbol{\xi}) \, \Delta\boldsymbol{u}_I \quad , \tag{4.12}$$

$$\boldsymbol{\phi}(\boldsymbol{\xi}) \approx \sum_{I=1}^{n_\mathrm{n}} N_I(\boldsymbol{\xi}) \, \boldsymbol{\phi}_I \quad , \quad \delta\boldsymbol{\phi}(\boldsymbol{\xi}) \approx \sum_{I=1}^{n_\mathrm{n}} N_I(\boldsymbol{\xi}) \, \delta\boldsymbol{\phi}_I \quad , \quad \Delta\boldsymbol{\phi}(\boldsymbol{\xi}) \approx \sum_{I=1}^{n_\mathrm{n}} N_I(\boldsymbol{\xi}) \, \Delta\boldsymbol{\phi}_I \quad , \tag{4.13}$$

with summation of all number of elements n_n. These relationships can be written in matrix form

$$\boldsymbol{u} \approx \boldsymbol{N}_u \, \hat{\boldsymbol{u}}, \tag{4.14}$$

$$\boldsymbol{\phi} \approx \boldsymbol{N}_\phi \, \hat{\boldsymbol{\phi}}. \tag{4.15}$$

In the following, the expressions of the electric field and strain field, with regard to equations 3.93 and 3.106, can be written

$$\boldsymbol{\varepsilon} = \boldsymbol{B}_u \, \hat{\boldsymbol{u}}, \tag{4.16}$$

$$\boldsymbol{E} = -\boldsymbol{B}_\phi \hat{\boldsymbol{\phi}}. \tag{4.17}$$

The matrices $\boldsymbol{B}_u$ and $\boldsymbol{B}_\phi$ are the derivatives of the shape functions for the mechanical displacements and electric potentials, respectively, and are expressed by

$$\boldsymbol{B}_u = \begin{bmatrix} \partial_x & 0 & 0 \\ 0 & \partial_x & 0 \\ 0 & 0 & \partial_x \\ 0 & \partial_z & \partial_y \\ \partial_z & 0 & \partial_x \\ \partial_y & \partial_x & 0 \end{bmatrix} \begin{bmatrix} \boldsymbol{N}_u \end{bmatrix}, \tag{4.18}$$

$$\boldsymbol{B}_\phi = \begin{bmatrix} \partial_x \\ \partial_y \\ \partial_z \end{bmatrix} \begin{bmatrix} \boldsymbol{N}_\phi \end{bmatrix}. \tag{4.19}$$

Following the classical procedure for finite element modeling and summing over all the elements, the mechanical and electrical equilibrium equations for linear piezoelectricity read as

$$\bigcup_{e=1}^{n_{el}} \int_{\mathcal{B}} \boldsymbol{B}_u^T \mathbb{C} \boldsymbol{B}_u \, \mathrm{d}V \, \hat{\boldsymbol{u}} + \bigcup_{e=1}^{n_{el}} \int_{\mathcal{B}} \boldsymbol{B}_u^T \boldsymbol{e} \boldsymbol{B}_\phi \, \mathrm{d}V \hat{\boldsymbol{\phi}} = \bigcup_{e=1}^{n_{el}} \int_{\partial\mathcal{B}} \boldsymbol{N}_u \boldsymbol{t} \, \mathrm{d}a, \tag{4.20}$$

and

$$\bigcup_{e=1}^{n_{el}} \int_{\mathcal{B}} \boldsymbol{B}_\phi^T \boldsymbol{e} \boldsymbol{B}_u \, \mathrm{d}V \, \hat{\boldsymbol{u}} - \bigcup_{e=1}^{n_{el}} \int_{\mathcal{B}} \boldsymbol{B}_\phi^T \boldsymbol{\epsilon} \boldsymbol{B}_\phi \, \mathrm{d}V \hat{\boldsymbol{\phi}} = \bigcup_{e=1}^{n_{el}} \int_{\partial\mathcal{B}} \boldsymbol{N}_\phi \boldsymbol{q} \, \mathrm{d}a. \tag{4.21}$$

The finite element expressions of the converse and the direct piezoelectric effect can be written in the following compact form

$$\boldsymbol{K}_{uu} \hat{\boldsymbol{u}} + \boldsymbol{K}_{u\phi} \hat{\boldsymbol{\phi}} = \boldsymbol{F}_{ext} \tag{4.22}$$

$$\boldsymbol{K}_{\phi u} \hat{\boldsymbol{u}} + \boldsymbol{K}_{\phi\phi} \hat{\boldsymbol{\phi}} = \boldsymbol{Q}_{ext} \tag{4.23}$$

with

$$\boldsymbol{K}_{uu} = \bigcup_{e=1}^{n_{el}} \int_{\mathcal{B}} \boldsymbol{B}_u^T \mathbb{C} \boldsymbol{B}_u \, \mathrm{d}V \tag{4.24}$$

$$\boldsymbol{K}_{u\phi} = \boldsymbol{K}_{\phi u}^T = \bigcup_{e=1}^{n_{el}} \int_{\mathcal{B}} \boldsymbol{B}_u^T \boldsymbol{e} \boldsymbol{B}_\phi \, \mathrm{d}V, \tag{4.25}$$

$$\boldsymbol{K}_{\phi\phi} = -\bigcup_{e=1}^{n_{el}} \int_{\mathcal{B}} \boldsymbol{B}_\phi^T \boldsymbol{\epsilon} \boldsymbol{B}_\phi \, \mathrm{d}V, \tag{4.26}$$

$$\boldsymbol{F}_{ext} = \bigcup_{e=1}^{n_{el}} \int_{\partial\mathcal{B}} \boldsymbol{N}_u \boldsymbol{t} \, \mathrm{d}a, \tag{4.27}$$

and

$$\boldsymbol{Q}_{ext} = \bigcup_{e=1}^{n_{el}} \int_{\partial\mathcal{B}} \boldsymbol{N}_{\phi}\, \boldsymbol{q}\, \mathrm{d}a. \tag{4.28}$$

Herein $\boldsymbol{K}_{uu}$ is the global elastic stiffness matrix, $\boldsymbol{K}_{u\phi}$ and $\boldsymbol{K}_{\phi u}$ denote the direct and converse piezoelectric stiffness matrices and $\boldsymbol{K}_{\phi\phi}$ is the global dielectric matrix. $\boldsymbol{F}_{ext}$ is the global nodal force loading vector, $\boldsymbol{Q}_{ext}$ is the surface density charge vector.

4.3 Finite Element Solution

The finite element solution is then obtained by solving the following equation

$$\begin{bmatrix} \boldsymbol{K}_{uu} & \boldsymbol{K}_{u\phi} \\ \boldsymbol{K}_{\phi u} & \boldsymbol{K}_{\phi\phi} \end{bmatrix} \begin{bmatrix} \boldsymbol{u} \\ \boldsymbol{\phi} \end{bmatrix} = \begin{bmatrix} \boldsymbol{F}_{ext} \\ \boldsymbol{Q}_{ext} \end{bmatrix} \tag{4.29}$$

Once the unknown variables, mechanical displacement $\boldsymbol{u}$ and electric potentioal $\boldsymbol{\phi}$, are obtaind, the other expressions $\boldsymbol{\varepsilon}$, $\boldsymbol{E}$, $\boldsymbol{\sigma}$ and $\boldsymbol{D}$ can also be calculated from Eq.4.17 and 4.16 and from the constitutive equations. The approximate solution found in this way can be improved either by using shape functions with higher order terms or increasing the number of elements. A study of finite element modeling for piezoelectric and adaptive structures has been undertaken by Benjeddou [2000], who also developed with Trindade and Ohayon [1999] a beam finite element for shear actuation. In some cases it is possible to solve equations 4.22 and 4.23, separately.

Therefore, the finite element version of actuator equation is obtained by

$$\hat{\boldsymbol{u}} = \boldsymbol{K}_{uu}^{-1}(\boldsymbol{F}_{ext} - \boldsymbol{K}_{u\phi}\hat{\boldsymbol{\phi}}). \tag{4.30}$$

Subsequently, when the displacement field is known, the finite element version of the sensor equation is written by

$$\hat{\boldsymbol{\phi}} = \boldsymbol{K}_{\phi\phi}^{-1}(\boldsymbol{Q}_{ext} - \boldsymbol{K}_{\phi u}\hat{\boldsymbol{u}}). \tag{4.31}$$

However, in general the full coupling between these two equations has to be taken into account. Therefore, an iterative approach has been set up to obtain the fully coupled solution. The procedure is briefly outlined below.

(1) Solve equation 4.30 assuming that $\hat{\boldsymbol{\phi}} = 0$, then calcute $\hat{\boldsymbol{u}}$, $\boldsymbol{\varepsilon}$ and $\boldsymbol{\sigma}$.

(2) Substitute the obtained value of $\hat{\boldsymbol{u}}$ into equation 4.31, then calculate value of $\hat{\boldsymbol{\phi}}$, $\boldsymbol{E}$ and $\boldsymbol{D}$.

(3) Substitute again the obtained value of $\hat{\boldsymbol{\phi}}$ into equation 4.30 and calculate $\hat{\boldsymbol{u}}$, $\boldsymbol{\varepsilon}$ and $\boldsymbol{\sigma}$.

(4) Compare the values of $\boldsymbol{u}$ by evaluating the following tolerance condition:

$$(|\,\hat{\boldsymbol{u}}^{(3)} - \hat{\boldsymbol{u}}^{(1)}\,|)/\,|\,\hat{\boldsymbol{u}}^{(1)}\,| \leq \beta_1, \tag{4.32}$$

where β_1 is tolerance parameter.

(5) Substitute again the obtained value of $\hat{\boldsymbol{u}}$ into equation 4.31 and calculate the values of $\hat{\boldsymbol{\phi}}$, $\boldsymbol{E}$ and $\boldsymbol{D}$.

(6) Compare the values of $\boldsymbol{\phi}$ by evaluating the following tolerance condition:

$$(|\,\hat{\boldsymbol{\phi}}^{(5)} - \hat{\boldsymbol{\phi}}^{(2)}\,|)/\,|\,\hat{\boldsymbol{\phi}}^{(2)}\,| \leq \beta_2, \tag{4.33}$$

where β_2 is tolerance parameter.

The solution procedure will converge after reasonable number of iterations. With this iterative approach both classic solid mechanics problems and field problems can be solved. This approach can also be extended for both geometric and material nonlinearity.

4.4 The Case of Nonlinear Constitutive Relations

An iterative approach for the solution is implemented in order to obtain mechanical and electrical equilibrium at each loop over incremental load steps. An incremental load stepping process is utilized because of the time dependent loading conditions and the non-linear constitutive response. The non-linear equations are solved by an iterative approach where the equilibrium condition is computed at each time step applying Newton-Raphson method. In this section, the incremental equilibrium equations are developed in order to establish a general solution scheme for nonlinear problems. In order to calculate the value of displacements at time $t + \Delta t$, the mechanical equilibrium is written

$$\int_{\mathcal{B}}^{t+\Delta t} \boldsymbol{\varepsilon}^T \mathbb{C}\, \boldsymbol{\varepsilon}\, \mathrm{d}V - \int_{\mathcal{B}}^{t+\Delta t} \boldsymbol{\varepsilon}^T \boldsymbol{e}\, \boldsymbol{E}\, \mathrm{d}V = \int_{\partial\mathcal{B}}^{t+\Delta t} \boldsymbol{u}^T \boldsymbol{t}\, \mathrm{d}a - \int_{\mathcal{B}}^{t} \boldsymbol{\sigma}\, \boldsymbol{\varepsilon}\, \mathrm{d}V. \tag{4.34}$$

A similar expression can be written for the electrical equilibrium

$$\int_{\mathcal{B}}^{t+\Delta t} \boldsymbol{E}^T \boldsymbol{e}\, \boldsymbol{\varepsilon}\, \mathrm{d}V + \int_{\mathcal{B}}^{t+\Delta t} \boldsymbol{E}^T \boldsymbol{\epsilon}\, \boldsymbol{E}\, \mathrm{d}V = -\int_{\partial\mathcal{B}}^{t+\Delta t} \boldsymbol{q}\, \boldsymbol{\phi}\, \mathrm{d}a - \int_{\mathcal{B}}^{t} \boldsymbol{D}\, \boldsymbol{E}\, \mathrm{d}V. \tag{4.35}$$

The general solution is determined by summing all the increments calculated for each time step. The final form of the obtained linearized finite element system reads

$$\begin{bmatrix} \boldsymbol{K}_{uu} & \boldsymbol{K}_{u\phi} \\ \boldsymbol{K}_{\phi u} & \boldsymbol{K}_{\phi\phi} \end{bmatrix}^t \begin{bmatrix} \boldsymbol{u}_n \\ \boldsymbol{\phi}_n \end{bmatrix} = \begin{bmatrix} \boldsymbol{F}_{ext} \\ \boldsymbol{Q}_{ext} \end{bmatrix}^{t+\Delta t} - \begin{bmatrix} \boldsymbol{F}_{int} \\ \boldsymbol{Q}_{int} \end{bmatrix}^t \tag{4.36}$$

with

$$\boldsymbol{F}_{int} = \bigcup_{e=1}^{n_{el}} \int_{\partial\mathcal{B}} \boldsymbol{B}_u^T \boldsymbol{\sigma} \, \mathrm{d}V, \tag{4.37}$$

and

$$\boldsymbol{Q}_{int} = \bigcup_{e=1}^{n_{el}} \int_{\partial\mathcal{B}} \boldsymbol{B}_\phi^T \boldsymbol{D} \, \mathrm{d}V, \tag{4.38}$$

where $\boldsymbol{F}_{int}$ represents the internal force vector and $\boldsymbol{Q}_{int}$ the internal density charge vector.

4.5 Verification of Coupled Electro-Mechanical Model

In this section, a numerical example for piezoelectric elements is proposed to verify the coupled electro-mechanical formulation and the related implementation. Therefore, a simple piezoelectric body is investigated as possible sensor and actuator.

4.5.1 Sensor

A three dimensional square cube has been generated with Ansys software in order to run the Matlab FEM code. This square cube has been discretized by 10 node tetrahedral element with 85 elements. A uniform surface load equal to 60.0 kN/cm is applied on the nodes along one of the cube's face. Contribution of nodal force which undergoes a uniform surface load analytically has been calculated. The polarization in z direction of the cube is assumed. Furthermore, in order to allow for a clear derivation of analytical results, Pois-

Elastic modulus (N/mm^2)	Piezoelectric Constants (C/m^2)	Electric permitivity (F/m^2)
$E = 65$	e_{31}=$e_{32} = -6.5$ $e_{33} = 23.3$	$\epsilon_{11} = \epsilon_{22} = 15.53e^{-9}$ $\epsilon_{33} = 15.50e^{-9}$

Table 4.1: Mechanical and electrical properties of piezoelectric body

son ratio is set to zero. This simplification is admissible here, as the decisive

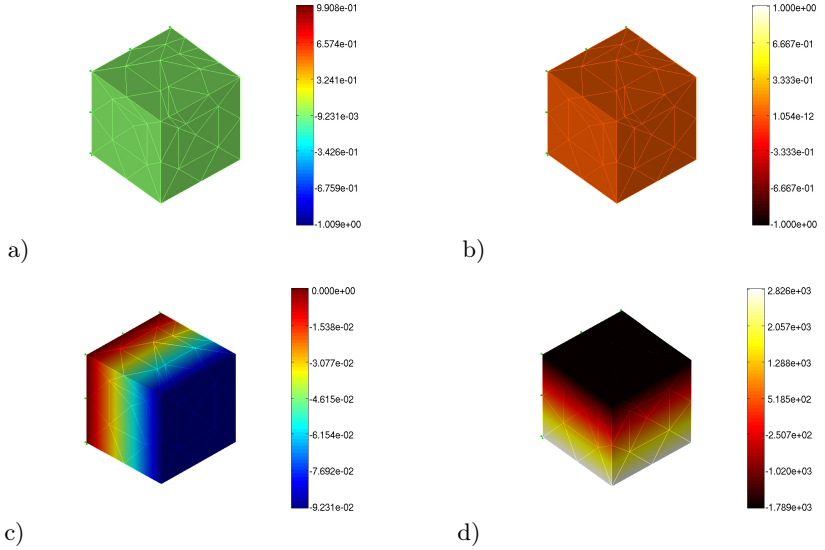

Figure 4.1: Sensor: a) Constant strain field ε_{11} b) Constant electric field E_3 c) Linear displacement d) Linear electrical potential difference.

coupling effects under consideration are not dependent on Poissons effect. The mechanical and electrical properties required for the finite element analysis are given in table 4.1.

Since no electrical potential or electrical charge has been applied as an electrical boundary conditions, all electric displacement components are set to zero. The linear constitutive equations for the piezoelectric model in x-direction are obtained as follows

$$\sigma_{11} = E\,\varepsilon_{11} - e_{31}\,E_3 \tag{4.39}$$

$$0 = e_{31}\,\varepsilon_{11} + \epsilon_{33}\,E_3\ . \tag{4.40}$$

Solving this system of equation leads to a constant strain $\varepsilon_{11} = 92.8 \times 10^{-4}$ and an electrical field in Z direction $E_3 = 4.98 \times 10^4\ V/m$. The same result is obtained with the numerical model. The constant fields of electrical and strain fields as illustrated on Fig. 4.1 (a) and (b). Furthermore, linear displacement in the same direction of loading and linear electrical potentioal in line with the polarization direction are illustrated in Fig. 4.1 (c) and (d). The comparison of analytical and numerical results is shown in table 4.2. All piezoelectric elements exactly match with the analytical result.

	u(m)	$\phi(V)$	$E_3(V/m)$	$S_{11}(N/m^2)$
Analytical solution	9.28×10^{-4}	4.986×10^3	4.986×10^4	6×10^6
Numerical results	9.28×10^{-4}	4.986×10^3	4.986×10^4	6×10^6

Table 4.2: Sensor: Comparison of analytical and numerical results.

4.5.2 Actuator

In next step, the inverse piezoelectric effect is investigated. Therefore, an electrical potential has been applied at the top and bottom surfaces of the cube as boundary conditions with $\phi_t = -2.364 \times 10^3$ V and $\phi_b = 2.622 \times 10^3$ V. This results in an electrical field $E = \frac{\phi_b - \phi_t}{t} = 4.986 \times 10^4\ V/m$, where t represents the distance between top and bottom surface. Since no external forces are applied, the stress σ_{11} remains zero. Thus the governing equations can be stated as:

$$0 = E\,\varepsilon_{11} - e_{31}\,E_3 \tag{4.41}$$

$$D_3 = e_{31}\,\varepsilon_{11} + \epsilon_{33}\,E_3 \tag{4.42}$$

Substituting the material parameters and the electric field value, one obtains $\boldsymbol{\varepsilon}_{11} = 0.498 \times 10^{-4}$ and $D_3 = 6.96 \times 10^{-6}\ C/m^2$. The longitudinal displacement at the free edge is $u = 4.98 \times 10^{-6}\ m$. The analytical result of the displacement, strain field and electrical displacement have been compared which is shown in table 4.3.

	u(m)	$E_{11}(V/m)$	$D_3(C/m^2)$
Analytical solution	4.98×10^{-6}	0.498×10^{-4}	6.96×10^{-6}
Numerical results	4.98×10^{-6}	0.498×10^{-4}	6.96×10^{-6}

Table 4.3: Actuator: Comparison of analytical and numerical results.

The linear state of the electrical potential and displacement leads to a correct representation of the constant electric and strain field, respectively, which it can be observed in Fig. 4.2.

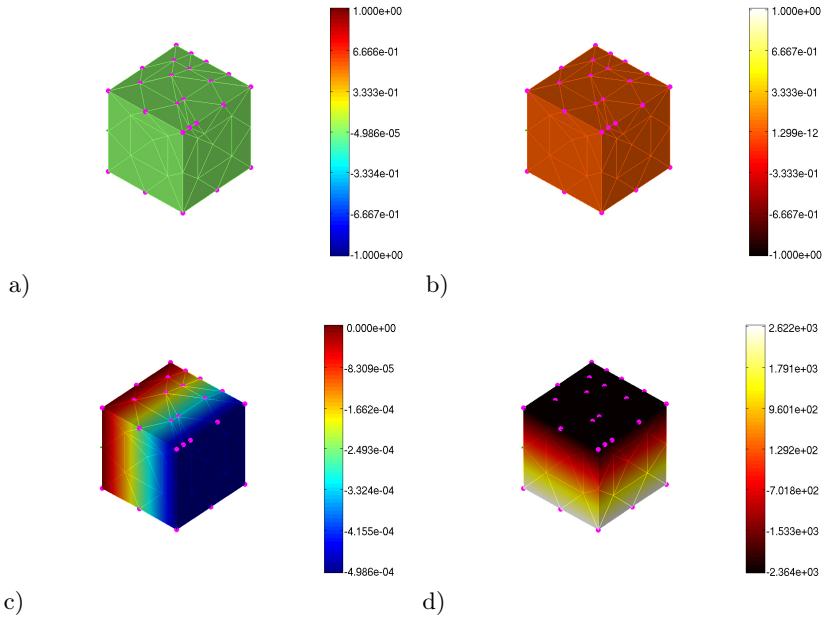

Figure 4.2: Actuator: a) Constant strain field ε_{11}, b) Constant electric field E_3, c) Linear displacement d) Linear electrical potential difference.

5 Finite Element Modeling of Teeth Implants

The biomechanical investigation of dental implants necessarily demands the application of three dimensional finite element models. Accordingly, a model for the jawbone has been extracted from a high resolution CT data. In a first step the surface geometry of a three-dimensional data is extracted. This process is called segmentation. In second step a triangle surface mesh is generated from the segmentation data. Afterwards, based on these data a CAD model is created with shape reconstruction techniques. In a subsequent step the prosthesis which consists of a conical part with a screw thread, an abutment and a crown is placed virtually into the mandible model. Furthermore, an interface layer for the simulation of osseointegration is generated.

In the following, these steps and the methods which have been applied in this work are described. Since the methods of image processing are not the goal of this thesis, they are only described briefly for a better understand the procedure. More detailed descriptions of the methods of digital image processing one may refere to Jähne [2005].

5.1 Segmentation

Image segmentation is the process of subdividing a digital image into its constituent regions or objects. This process is started by using CT data set of a 63 years old male patient. The patient's skull is segmented using image processing techniques provided by MATLAB, as sketched in Fig. 5.1 (a). Subsequently, the entire data set is converted into a three dimensional image using thresholding. Thresholding describes an operation by which a binary image is generated from a grayscale image. For this reason, a threshold value for the grayscale is specified, which divides the image into black and white background and foreground pixels. The threshold value can automatically be determined by Matlab. The lower mandible depicted in Fig. 5.1 (b) was highlighted dark for reasons of clarity. Then, the extraction of the lower jaw from the result of the thresholding process is simple to carry out.

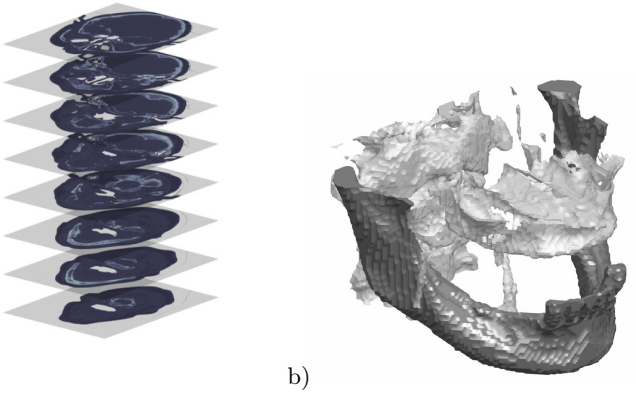

a) b)

Figure 5.1: Model generation from CT-data (a), 3D thresholding a skull data set (b).

5.2 Reconstruction of Surface and CAD Models

The next step for the generation of geometric models is the generation of surface models from the segmentation data. The segmentation data are composed of a binary and three dimensional data of the region of interest (ROI), i.e., the region of the mandible. With this knowledge an isosurface between the region of interest and the surrounding areas can simply be provided using the functionalities of Matlab. The lower mandible is reconstructed from a triangle surface model Fig. 5.2 (a).

Afterwards, the generation of a CAD model of the mandible is necessary for finite element simulations. The surface data is processed using a Non-Uniform Rational B-Splines (NURBS) technique to generate CAD surfaces which enable for Boolean operations on virtual endoprostheses implantation. However, the reconstructed model appears to be highly inconsistent with the physical model because of the irregular structure of the mandible. Therefore, professional reverse engineering software is suggested to create a CAD model, as shown in Fig. 5.2 (b).

Now the three dimensional CAD model of the dental prosthesis is created. The implant geometry is one factor which can effect on the primary stability and osseointegration under immediate loading. A cylindrical and threaded dental implant is selected for this study. The dimensions of conical part, abutment and crown have been measured based on a real sample the CAD models are shown in Fig. 5.2 (c). The CAD model of mandible with prosthesis is depicted

in Fig. 5.2 (d).

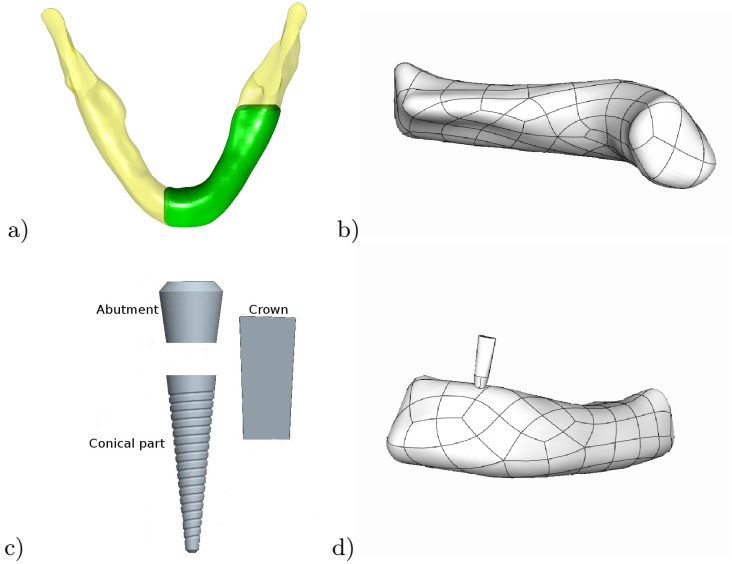

Figure 5.2: a) View of the total mandible, green color part represents the left half of mandible, b) CAD model of mandible, c) CAD model of the implant, d) The implant is placed virtually into the mandible model

5.3 Finite Element Models

In this step, the 3D CAD model is discretized for the finite element model. In order to achieve the results with high accuracy, a fine mesh is generated surrounding dental implant. The finite element model of the mandible and the implant consists of 16,329 nodes and 92,072 linear tetrahedral elements. The threaded part of implant is intended to allow the postoperative osseointegration. Without considering the interface layer, mandible and implant would have a perfect osseointegration which is physiologically not correct. Therefore, a bio-active interface layer is modeled with osseointegration capability in order to simulate the physiological behavior of the interface. The interface layer is generated fully automatically with an in-house Matlab code; it consists of

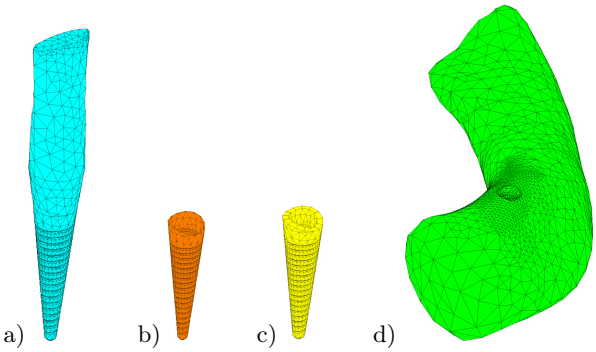

Figure 5.3: Finite element model: implant (a), piezoelectric coating (b), bio-active interface layer (c) and mandible (d).

1,775 linear wedge interface elements.

An exploded view of the finite element models of implant, piezoelectric coating, interface layer and mandible is depicted in Fig. 5.3. The thin layer of the polyvinylidene fluoride (PVDF) film coated conical part of the implant with a thickness of 0.1 mm is shown by orange color. The bio-active interface elements with a thickness of 0.5 mm are depicted in yellow color.

5.4 Projection of CT Intensities to the Finite Element Model

For the computational study it is necessary to reconstruct the information of the material properties of the real mandible from the CT-data. To do so, the Hounsfield units from CT data set are projected on to the finite element model. This step consists on mapping the bone mineral density distribution information of the host bone onto the postoperative state from which the elastic moduli for the mandible part of the finite element model are computed by Eq. 3.98. The mechanical properties adopted here are specified in terms of Young's modulus, Poisson's ratio, mass density and physiological target values for all model groups are summarized in table 5.1.

Since blood and mushy bone are generated in the bone-implant interface immediately after surgery, Poisson's ratio is introduced for nearly incompressible behavior and the simulation process is started with relatively low adhesion in the interface. The material properties of the dental implant are chosen for titanium.

Table 5.1: Material parameters for different parts of the jawbone-implant intractive system

Parts	Elastic, modulus (N/mm^2)	Poisson's ratio	Density, (g/cm^3)	Physiological target value (Nm/g)
Bone	$E_0 = 2,000$	$\nu = 0.29$	$\rho_0 = 1$	
Implant	$E = 105000$	$\nu = 0.31$		
Interface	$E_{start} = 1.5$	ν_{min}= 0.29 ν_{max}= 0.43	ρ_{min}= 0.0277 ρ_{max}= 2.8	$\psi_{ref_m} = 0.0004$ $\psi_{ref_e} = 0.000003$
PVDF film	$E = 6000$	$\nu = 0.29$	$\rho = 1780$	

5.5 Boundary Conditions and Simulation Approach

Homogeneous Dirichlet boundary conditions are applied to the medial and dorsal ends of mandible. The real physiological situation is fitted and local disturbances are omitted due to St.Venant's principle. Physiological chewing conditions are applied to the head to the implanted tooth. Direction and magnitude of the loads have been adopted from literature, e.g. Canay et al. [1996]; Ronold et al. [2003]; Meijer et al. [1993]; Merdji et al. [2012]. Barbier et al. [1998] reported that the magnitude of the applied horizontal load was five times smaller than that of the vertical load.

Typical load level experienced during the mastication reported in the coronal-apical (vertical), lingualbuccal(transverse) and mesial-distal (mesiodistal) directions have been reported by Richter [1998]. Dynamic loads in three aforementioned directions are applied on the occlusale face of the crown at low frequency as sketched in Fig. 5.4 (b). The loading induced by the jawbone muscles onto implant have been neglected because of its minor meaning for the bone-implant interface conditions.

The time history of masticatory dynamic load is demonstrated in Fig. 5.4 (a) for a time sequence of 10 s. A non-linear quasi-static finite element analysis is performed while chewing force sequence is discretized into 10 timesteps. An incremental load stepping process is utilized because of the time dependent loading conditions and the non-linear constitutive response. The non-linear equations are solved by an iterative approach where the equilibrium condition is computed in each time step applying Newton-Raphson method. The values of micromotion and energy density, from mechanical and electrical stimulus, are calculated for the interface layer elements. In a subsequent step the time dependent process of osseointegration prediction is performed with regard to

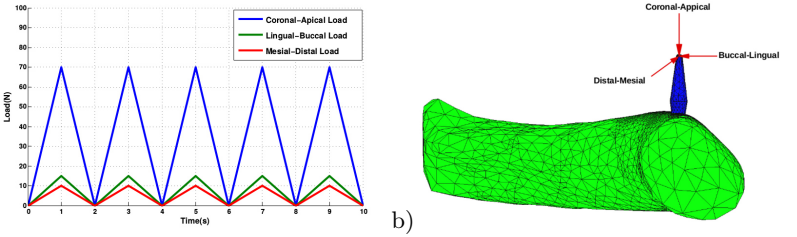

a) b)

Figure 5.4: a) Time dependent loading for normal chewing b) loading components in coronal-apical, lingual-buccal and mesial-distal directions.

ingrowing restriction from micromotion threshold. This procedure has been implemented into a MATLAB-based finite element environment.

6 Numerical Studies on Implant Osseointegration

The application of the methods for electromechanically stimulated osseointegration is demonstrated in this chapter. The effect of electromechanical stimulus on the osseointegration process in the bone-implant interface is investigated.

In a first step, electromechanical stimulation is studied based on the electrical characteristics of bone tissue. Subsequently, the computed results are compared with pure mechanical stimulus. Then, the effect of variation of micromotion threshold on the osseointegration process is studied. Furthermore, extensive parametric studies have been carried out for different values of piezoelectric constants in order to investigate a suitable range to improve the osseointegration capabilities of dental implants.

6.1 Electromechanically Stimulated Osseointegration

6.1.1 Electrical Properties of Bone tissue

In this study a combined electrical and mechanical stimulus was implemented to determine osseointegration of bone-implant interface when the dental prosthesis system is subjected to periodic dynamic load. In a first comparative study, electrical properties of bone cells were assigned to the bio-active interface only without considering piezoelectric coating in order to evaluate the effect of bone cell piezoelasticity on osseointegration separately.

Some authors, e.g. (see Fotiadis et al. [1999]; Gjelsvik [1973b]; Qin and Ye [2004b]; Ramtani [2008]), reported that bones behave in the same way as a crystal with hexagonal symmetry. The related piezoelectric constitutive tensor is defined by four independent variables and the dielectric tensor is represented as a diagonal matrix with two constants. The material data used here are adopted from Fotiadis et al. [1999] are summarized in table 6.1. The entries

Table 6.1: Electrical characteristics of Bio-active interface and PVDF film

Parts	Piezoelectric constant, $(N/Vmm) \times 10^{-6}$	Dielectric constant, $(N/V^2) \times 10^{-9}$
Bio-active interface	$e_{31} = 1.5$ $e_{33} = 1.87$ $e_{14} = 17.88$ $e_{15} = 3.57$	$\epsilon_{11} = 88.54$ $\epsilon_{33} = 106.24$
PVDF film	$e_{31} = 43.5$ $e_{32} = -28.5$ $e_{33} = -193.6$	$\epsilon_{11} = 0.1$

of piezoelectric constants and electric permitivity matrix is reperesnted

$$e = \begin{bmatrix} 0 & 0 & 0 & e_{14} & e_{15} & 0 \\ 0 & 0 & 0 & e_{15} & -e_{14} & 0 \\ e_{31} & e_{31} & e_{33} & 0 & 0 & 0 \end{bmatrix}, \epsilon = \begin{bmatrix} \epsilon_{11} & 0 & 0 \\ 0 & \epsilon_{11} & 0 \\ 0 & 0 & \epsilon_{33} \end{bmatrix} \tag{6.1}$$

The osseointegration in the bone implant interface strongly depends on the initial micromotion conditions as discussed in the introduction. For these principle studies a threshold of 100 μm has been applied. The osseointegration progress considering the electromechanical stimulus of the bio-active interface is depicted in Fig.6.1 for five different time instant. It can be seen that with proceeding time the bone-implant interface becomes more bony which is indicated by red color. A comparison between the computed result for the osseointegration process based on electromechanical and pure mechanical stimulation in the bone implant interface layer at the beginning, in the middle, and at the end of the simulation process is shown in Fig. 6.2.

From these studies one observes that osseointegration augmented by electromechanical stimulation started faster than with pure mechanical stimulation already from the first step. With ongoing osseointegration to middle and final step the interface layer becomes more bony and stable. The amount of osseointegration for electromechanical stimulation is more pronounced than for pure mechanical during the hole osseointegration process.

6.1.2 Micromotion Limit

In a second study the variation of the micromotion limit is investigated as a remarkable factor which can affect the initial post surgery behavior of a dental prosthesis. The final state of osseointegration obtained with limit values of 50,

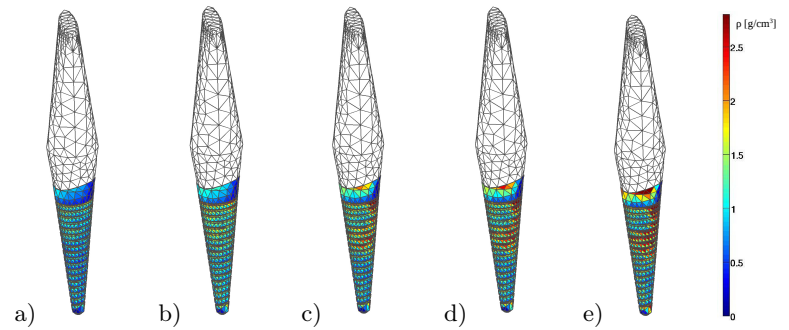

Figure 6.1: Electromechanical stimulation on the osseointegration prediction in the interface with 100 μm micromotion threshold from timesteps 1 (a), 3 (b), 5 (c), 7 (d) and (e) 10.

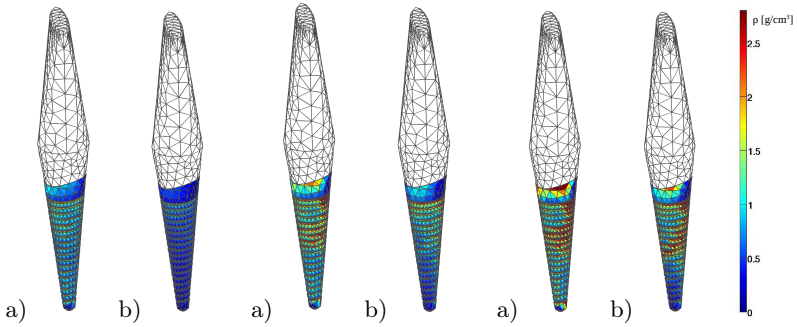

Figure 6.2: Comparison of a) electromechanical and b) mechanical stimulation on the osseointegration prediction in the interface with 100 μm micromotion threshold from timesteps 1, 5 and 10 (left to right).

75 and 100 μm are shown in Fig. 6.3. With increasing micromotion threshold varied from 50 to 100 μm the osseointegration increases considerably.

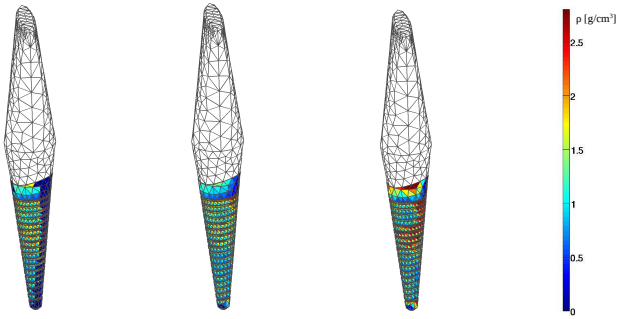

Figure 6.3: Final state of the osseointegration prediction considering electromechanical stimulation with 50, 75 and 100 μm micromotion threshold (left to right).

6.1.3 Additional Piezoelectric Coating

It has been discussed so far, that electrical stimulus within the bone itself can improve bone growth and enhance faster healing. In this second step, the influence of an additional piezoelectric coating of the implant is investigated. According to Fotiadis et al. [1999] and Chopra [2014], the electrical properties of both bone tissue and typical PVDF film are displayed in table 6.1.

Since a PVDF film is modeled under small strains, the present study proposes an approach to adapt transversely isotropic materials. The longitudinal and transverse effects on PVDF film have been considered where normal stresses are applied in parallel and transverse direction to polarization. Accordingly, piezoelectric constants reduce to three non-zero components only,

$$e = \begin{bmatrix} 0 & 0 & 0 & 0 & 0 & 0 \\ 0 & 0 & 0 & 0 & 0 & 0 \\ e_{31} & e_{32} & e_{33} & 0 & 0 & 0 \end{bmatrix}, \epsilon = \begin{bmatrix} \epsilon_{11} & 0 & 0 \\ 0 & \epsilon_{11} & 0 \\ 0 & 0 & \epsilon_{11} \end{bmatrix}. \tag{6.2}$$

The electric field strength produced by PVDF coating due to normal chewing conditions is of significant importance. As rather low field intensity doesn't affect on bone cell proliferation while quite excessive fields might cause cell necrosis. As discussed in the introduction, a window of electric field strength

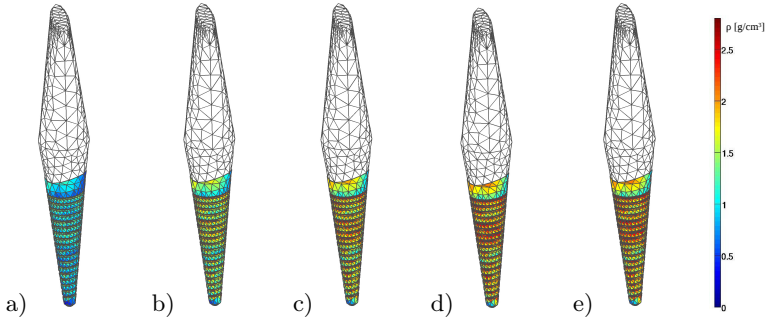

Figure 6.4: The osseointegration prediction considering additional piezoelectric layer with 100 μm micromotion threshold from timesteps 1 (a), 3 (b), 5 (c), 7 (d) and (e) 10.

between $10^{-5} - 10^{-3}$ V/mm has been reported by Brighton et al. [1992] to be beneficial for cell proliferation. Piezoelectric constants of PVDF film are thus important for the control of the magnitude of electric fields. In particular, the value e_{33} is nearly five times larger than the two other constants and therefore has the most important contribution in electric field production.

6.2 Parametric Study

A parametric study has been carried out in order to achieve a best value of e_{33} to provide an electric field in the aforementioned range to improve the osseointegration capabilities of teeth implants. The variation of the electrical field depending on the piezoelectric constant is shown in Fig.6.5, plotted in a dimensionless logarithmic scale.

The tolerable domain of the induced electrical field with regard to variation of e_{33} is shown by green color, while less field strength (blue) does not affect the cell activity at all and higher field strength (red) could affect apoptosis. In comparison with the specific data for the PVDF layer (table 6.1) it is concluded that this material would not be suitable for coating of bone dental implants. It is concluded that new coating materials and/or novel manufacturing techniques have to be developed for the improvement of osseointegration properties of dental implants by advanced electrical stimulation.

Nonetheless, in order to demonstrate the potential of electromechanical stimulation of primal osseointegration of teeth implants a comparative study suitable piezoelectric constants has been performed. A threshold value of 100 μm and a constant of $e_{33} = -193.6 \times 10^{-12}$ N/Vmm has been applied for these principle investigations. The results for the time sequence are depicted in Fig. 6.4

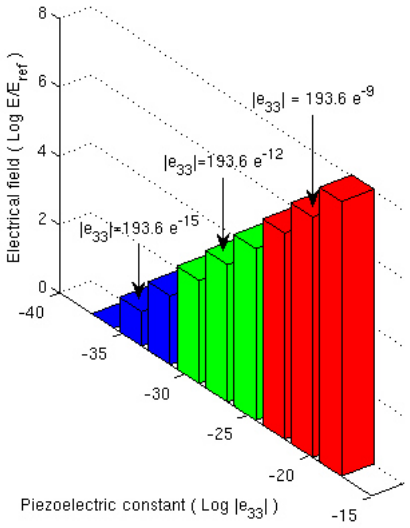

Figure 6.5: Dimensionless induced electrical field in dependecy of e_{33} ($E_{ref} = 10^{-8}\ V/mm$)

which have to be compared with Fig. 6.2.

The evolution of density in bio-active interface at each time instant has been compared between pure mechanical stimulation, bio-active interface with electrical properties of bone tissue and additional PVDF layer, which is illustrated in Fig.6.6. Two key points could be derived from this Figure. First, as expected the density change profile goes asymptotically to a saturated and steady state value. This could be interpreted as a complete healing process. Second, the presence of PVDF layer enhances the osseointegration process. It means that it leads to increased areas of osseointegration in comparison with the case in which such a layer doesn't exist. A comparison of average density between electromechanical stimulation of bio-active interface and pure mechanical stimulation at the final step indicates 14.5% more bony ingrowth. From the additional active electrical stimulation from the PVDF layer an improvement of osseointegration of an amount of approximately 24.4% compared to pure mechanical stimulation is predicted.

Since mechanical stresses play an important role in bone remodeling and the electric field produced in piezoelectric coating, a evaluation of the stress distributions in the bone, bio-active interface and PVDF layer is needed. Therefore,

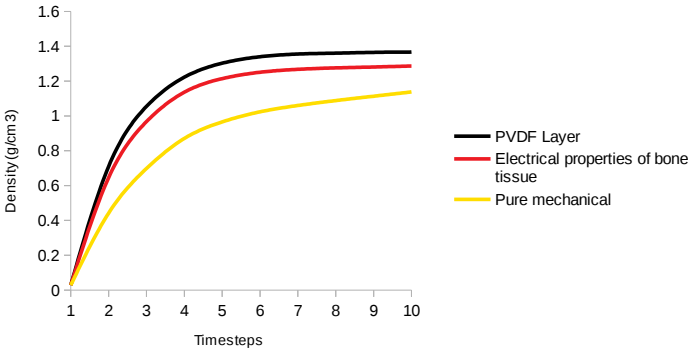

Figure 6.6: Comparison of evolution of density in bio-active interface with pure mechanical stimulation, electrical properties of bone tissue and additional PVDF layer from timesteps 1 to 10.

the mean and maximum von Mises stress distribution under combined dynamic load from timesteps 1 to 10 are displayed in Fig.6.7.

From Fig.6.7 (a) one can find that there is an apparent transition in the role of PVDF layer. In other words, at the primary timesteps the stress level in the PVDF layer is considerable but it gradually decreases. This is due to the larger contribution of the PVDF layer to the mechanical stiffness of the system prior to the development of osseointegration.

Once the osseointegration progresses the mechanical load applied on PVDF layer decreases and its role as an auxiliary mechanical structure fades out. It can be seen that with proceeding time, the mean value of von Mises stress in the interface layer increases. This result confirmed that the abilty of the bio-active interface layer to carry mechanical load increases due to the ongoing mineralization. Subsequently, the mean value of von Mises stress in the PVDF layer decreases to reach a constant value.

The description of maximum von Mises stress at each timesteps is depicted in Fig.6.7 (b). The highest von Mises stresses occure in the mandible structure. A second stress peak is observed at the PVDF layer, but its value was much lower than in the mandible bone. A third peak is observed at the bio-active interface layer which however is not so pronounced.

Since electromechanical stimulation could simultaneously contribute to bone formation, the mean value of both strain and electric energy density in the bone-implant interface layer at each timesteps is illustrated in Fig.6.8. However, based on energy densities one should argue carefully. At the first glance,

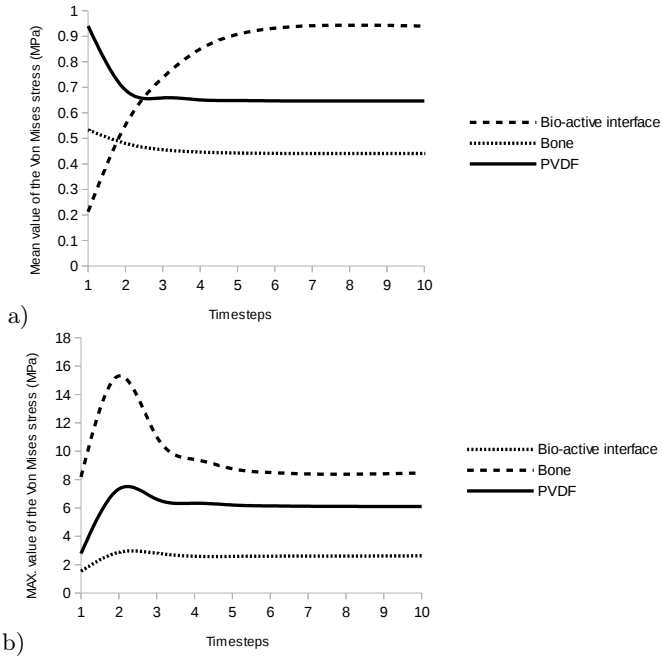

Figure 6.7: Mean (a) and maximum (b) value of Von Mises stress for Bio-active interface, mandible bone and PVDF layer from timesteps 1 to 10.

a decrease of energy density appears unusual.

One needs to pay attention to the point that not only the stress and strain change in the bio-active interface, but also the material tangent stiffness varies during the osseointegration process. That's why the energy density has a descending behaviour in time. In addition, it can be observed that the mean value of electric energy density (EED) is much less than strain energy density (SED). In other words, the electrical part of energy is not dominant in terms of the total energy of the system. In fact, it plays the role of stimuli for osseointegration process rather than a mechanism which absorbs and stores the energy of the system. That is the reason why the electrical physiological target value is distinguished from the mechanical in equation 3.87.

In the following the distribution of electric potential and electrical field with considering suitable piezoelectric constants on the PVDF layer are discussed. The maximum, minimum and mean values of the electric potential are displayed in Fig. 6.9. The oscillatory behavior of the electric potential was expected because of masticatory dynamic loading conditions. In other words,

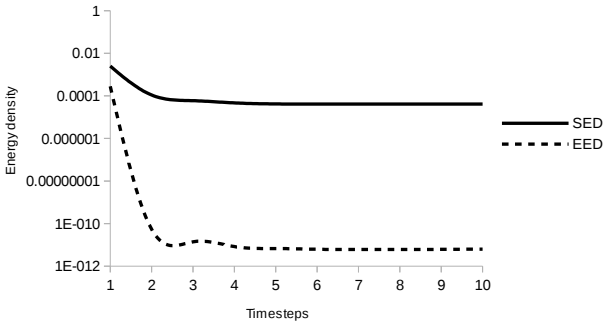

Figure 6.8: The mean value of strain and electric energy density of bio-active interface layer from timesteps 1 to 10.

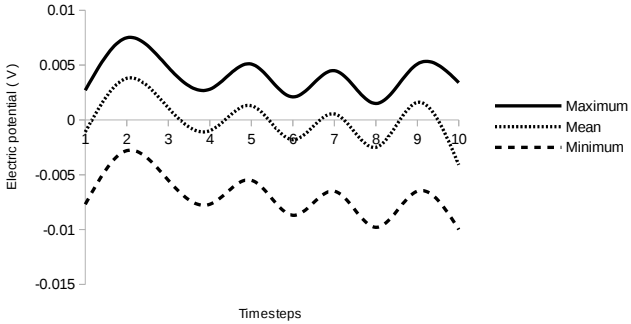

Figure 6.9: Electric potential distribution in PVDF layer from timesteps 1 to 10.

the induced voltage (electric potential) follows the dynamics of the mechanical load. However, the interesting point is that such an ossilatory response is not observed in the mechanical response, i.e. stress and energy of the system. One can make this reasoning that the osseointegration process is of accumulative ones which flattens any fluctuating input and finally results in a smooth output. The mean value of electric potential generated in PVDF layer varies between -0.004 and 0.004 V from timesteps 1 to 10.

As discussed before, the magnitude of the electric field which is produced by means of the electric potential difference plays an important role on bone formation, as rather low field intensity doesn't affect on bone cell proliferation while quite excessive fields might cause cell necrosis. Therefore, the mean value of electric field which is produced in the PVDF layer is depicted in Fig.6.10.

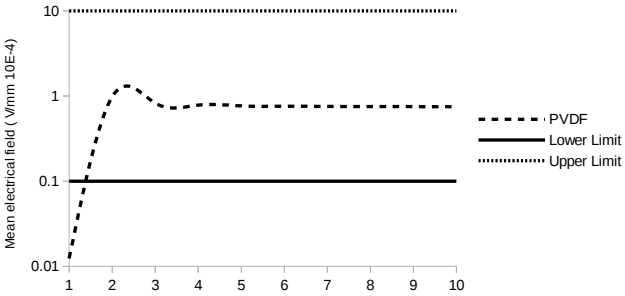

Figure 6.10: Mean value of electrical field in PVDF layer from timesteps 1 to 10.

It can be seen that the mean value of electric field is in tolerable domain during the timesteps. It should be noted that the piezoelectric constants have been taken in such a way that the total induced electrical field doesn't exceed the tolerable domain. This is an important outcome from the manufacturing point of view. It means that a numerical study prior to manufacturing process insures the feasibility and applicability of such a piezoelectric interface surrounding the dental implants.

7 Conclusion and Future Research

The primal osseointegration of dental prostheses is introduced as the most important parameter for the long term durability of implants. Experimental studies as discussed in literature indicate that bone formation at the bone-implant interface can be improved using electrical stimulation. Therefore, an electromechanical bone remodeling theory was developed in order to investigate the influence of piezo-electrical stimulation on osseointegration process. A certain amount of initial relative motion is discussed as significant factor for the failure of initial bony ingrowth. Bone formation is prohibited when the micromotion increases a certain threshold limit. In this study a computational simulation has been caried out in order to evaluate the influence of electromechanical stimulation on the ingrowth behaviour in a bio-active interface layer. A soft, thin bone-implant interface layer has been modeled in order to simulate the osseointegration starting with a mixture of liquid phase and bony fragments which appears immediately after surgery. This layer has the ability to adopt piezoelectric properties of bone for electromechanical stimulation. Therefore, the hypothesis of electromechanical bone remodeling has been combined with a Drucker-Prager interface model which describes the mechanical behaviour of the interface. Furthermore, an additional piezoelectric coating was modeled surrounding the dental implant which provides a surface electrical charge in order to electrical interactions with the physiological environment.

In the following, numerical studies have been performed based on a 3D model of lower mandible and implant under dynamic chewing loads. A comparison was made between electromechanical and pure mechanical stimulation on the osseointegration process. It was shown that an electrical stimulus can increase cell migration speed and accelerate the osseointegration process because of natural electrical properties of bone. As still an accepted value of micromotion threshold limit has not been reported, limit values of 50, 75 and 100 μm have been studied. It was shown that the amount of osseointegration increases for higher micromotion threshold.

Since electrical properties of bone tissue lead to an increase in bone formation, an additional piezoelectric coating has been studied in order to recruit a larger number of bone cells to attach to the implant surface. For this rea-

son the PVDF film has been utilized as a biocompatible material which is widely used in medical applications. However, the magnitude of electric field should be controled while exessive electric field strength leads to cell necrosis. As e.g. Brighton et al. [1992] reported that electric field strength of $10^{-5} - 10^{-3}\ V/mm$ can increase the rate of bone formation and fields less than $10^{-5} V/mm$ don't have affect on bone formation. The parametric study shown in Fig. 6.5 demonstrates the range of values for e_{33}. With green color the tolerable domain for electrical fields is shown. Numerical results indicate 24.4 % more bone formation considering additional piezoelectric coating in comparison with pure mechanical stimulation. Consequently, electric field which is produced by piezoelectric coating accelerates formation of new bone tissue at the bone-dental implant interface and reduces the time of the healing process.

Despite the fact, that a couple of unsure data and model assumptions have been considered for these investigation, the findings should be judged qualitatively only. Nonetheless, by this study the potential contribution of computational mechanics simulations on the development of sophisticated bone implants has been demonstrated. For quantitative answers further goal oriented experimental investigations and perhaps probabilistic modeling approaches are needed.

References

Aaron RK., S. M. (1991). Electrical stimulation of osteonecrosis of the femoral head. *Semin Arthroplasty*, 2:214–221.

Abdul-Kadir, M. R., Hansen, U., Klabunde, R., Lucas, D., and Amis, A. (2008). Finite element modelling of primary hip stem stability: the effect of interference fit. *J Biomech*, 41(3):587–594.

Ahn, A. and Grodzinsky, A. (2009). Relevance of collagen piezoelectricity to "wolff's law": a critical review. *Medical engineering and physics*, 31(7):733–41.

Albrektsson, T. and Johansson, C. (2001). Osteoinduction, osteoconduction and osseointegration. *Eur Spine J*, 10 Suppl 2:S96–101.

Ambard, D. and Swider, P. (2006). A predictive mechano-biological model of the bone-implant healing. *European Journal of Mechanics Series a Solids*, 25(6):927–937.

An, Y. and Draughn, R. (1999). Mechanical testing of bone and the bone-implant interface. *book*.

Aschero, G., Gizdulich, P., Mango, F., and Romano, S. (1996). Converse piezoelectric effect detected in fresh cow femur bone. *Journal of Biomechanics*, 29(9):1169 – 1174.

Austman, R. L., Milner, J. S., Holdsworth, D. W., and Dunning, C. E. (2008). The effect of the density-modulus relationship selected to apply material properties in a finite element model of long bone. *J Biomech*, 41:3171–3176.

Balke, H. (2010). Einführung in die Technische Mechanik: Festigkeitslehre. *Springer*.

Barbier, L., Sloten, J., Krzesinski, G., and van der Perre, E. (1998). Finite element analysis of non-axial versus axial loading of oral implants in the mandible of the dog. *Journal of Oral Rehabilitation*, 25(11):847–858.

Basset, C. A. L., P. R. J. and Becker, R. O. (1964). Effects of electric current on bone in vivo. *Nature*, 204:652–654.

Bathe, K.-J. (2001). *Finite-Elemente-Methoden*. Springer, Berlin, 2. auflage edition.

Beck, B., Qin, Y., Rubin, C., McLeod, K., and Otter, M. (1997). The relationship of streaming potential magnitude to strain and periosteal modeling 567. *Medicine and Science In Sports and Exercise*, 29.

Behari, J. (2009). *Biophysical bone behavior principles and applications*. Singapore ; John Wiley & Sons, c2009.

Benjeddou, A. (2000). Advances in piezoelectric Ænite element modeling of adaptive structural elements: a survey. *Computers and Structures*, 76:347–363.

Besson, J., Cailletaud, G., Chaboche, J., and Forest, S. (2010). Non-linear mechanics of materials. *Springer, Solid Mechanics and Its Applications*, 167.

Brighton, C. (1981). The treatment of non-unions with electricity. *J Bone Joint Surg Am*, 63:847–851.

Brighton, C., Black, J., Friedenberg, Z. B., Esterhai, J. L., Day, L. J., and Connolly, J. F. (1981). A multicenter study of the treatment of non-union with constant direct current. *J Bone Joint Surg*, 63(1):2–13.

Brighton, C., Okereke, E., Pollack, S., and Clark, C. (1992). In vitro bone-cell response to a capacitively coupled electrical field. the role of field strength, pulse pattern, and duty cycle. *Clin Orthop Relat Res*, (285):255–62.

Brighton, C., Tadduni, G., and Pollack, S. (1985). Treatment of sciatic denervation disuse osteoporosis in the rat tibia with capacitively coupled electrical stimulation. dose response and duty cycle. *Bone Joint Surg Am*, 67:1022–1028.

Brighton, C., Wang, W., Seldes, R., Zhang, G., and Pollack, S. (2001). Signal transduction in electrically stimulated bone cells. *Bone Joint Surg Am*, 83:1514–1523.

Bystrov, V. S., Seyedhosseini, E., Kopyl, S., Bdikin, I. K., and Kholkin, A. L. (2014). Piezoelectricity and ferroelectricity in biomaterials: Molecular modeling and piezoresponse force microscopy measurements. *J. Appl. Phys.*, 116.

Büchler, P., Pioletti, D. P., and Rakotomanana, L. R. (2003). Biphasic constitutive laws for biological interface evolution. *Biomech Model Mechanobiol*, 1(4):239–249.

Callegari, B. and Belangero, D. (2004). Analysis of the interface formed among the poli (viniilidene) fluoride (piezoelectric and non-piezoelectric) and the bone tissue of rats. *Acta ortop. bras.*, 12(3).

Canay, S., Hersek, N., Akpinar, I., and Asik, Z. (1996). Comparison of stress distribution around vertical and angled implants with finite-element analysis. *Quintessence Int.*, 27(9):591–598.

Carter, D., Fyhrie, D., and Whalen, R. (1987). Trabecular bone density and loading history: regulation of connective tissue biology by mechanical energy. *J Biomech*, 20:785–794.

Carter, D. R. and Hayes, W. C. (1977). The compressive behavior of bone as a two-phase porous structure. *J Bone Joint Surg Am*, 59(7):954–962.

Carter, D. R., Orr, T. E., and Fyhrie, D. P. (1989). Relationships between loading history and femoral cancellous bone architecture. *J Biomech*, 22(3):231–244.

Chopra, I. (2014). *Smart structures theory*. Cambridge, UK; Cambridge University Press.

Ciombor, D. M. and Aaron, R. K. (2005). The role of electrical stimulation in bone repair. *Foot and Ankle Clinics*, 10(4):579 – 593.

Cowin, S. C. (1986). Wolff's law of trabecular architecture at remodeling equilibrium. *J Biomech Eng*, 108(1):83–88.

Cowin, S. C. and Hegedus, D. H. (1976). Bone remodeling i: theory of adaptive elasticity. *Journal of Elasticity*, 6(3):313–326.

Cowin, S. C. and Nachlinger, R. R. (1978). Bone remodeling iii: uniqueness and stability in adaptive elasticity theory. *Journal of Elasticity*, 8(3):285–295.

Crowley, J. M. (1986). Fundamentals of applied electromechanics. *Wiley and sons*.

Davies, J. (2003). Understanding peri-implant endosseous healing. *J Dent Educ*, 67(8):932–49.

de Pepp, G. M. (2011). Human embryonic stem cells for bone engineering applications. *PHD Thesis, University of Gothenbur*.

Demiray, H. (1983). Electro-mechanical remodelling of bones. *International Journal of Engineering Science*, 21(9):1117 – 1126.

Doblaré, M. and García, J. M. (2002). Anisotropic bone remodelling model based on a continuum damage-repair theory. *J Biomech*, 35(1):1–17.

Einhorn, T. (1998). The cell and molecular biology of fracture healing. *Clin Orthop Relat Res.*, 355:7–21.

Fernandez-Tresguerres-Hernandez-Gil, I., Alobera-Gracia, M., and del Canto-Pingarron, M. (2006). Physiological bases of bone regeneration ii. the remodeling process. *Med Oral Patol Oral Cir Bucal.*, 11:151–157.

Fotiadis, D., Foutsitzi, G., and Massalas, C. (1999). Wave propagation modeling in human long bones. *Acta Mechanica*, 137:65–81.

Friedenberg, Z. and Brighton, C. (1966). Bioelectric potentials in bone. *J Bone Joint Surg Am*, 48:915–23.

Friedenberg, Z. and Smith, H. (1969). Electrical potentials in intact and fractured tibia. *Clinical Orthopaedics and Related Research*, 63:222–225.

Frost, H. M. (1988). Vital biomechanics: Proposed general concepts for skeletal adaptations to mechanical usage. *Calcified Tissue International*, 42(3):145–156.

Fukada, E. and Yasuda, I. (1957). On the piezoelectric effect of bone. *Journal of the Physical Society of Japan*, 12(10):1158–1162.

Fyhrie, D. P. and Carter, D. R. (1986). A unifying principle relating stress to trabecular bone morphology. *Journal of Orthopaedic Research*, 4(3):304–317.

Gabriel, C., Gabriel, S., and Corthout, E. (1996). The dielectric properties of biological tissues: I. literature survey. *Physics in Medicine and Biology*, 41(11):2231–2249.

Garzón-Alvarado, D., Ramírez-Martínez, A., and Cardozo de Martínez, C. (2012). Numerical test concerning bone mass apposition under electrical and mechanical stimulus. *Theor Biol Med Model*, 9(14).

Gaudenzi, P. (2009). *Smart Structures: Physical Behaviour, Mathematical Modelling and Applications*. Wiley.

Giannunzio, G., Speerli, R., and Guglielmotti, M. (2008). Electrical field effect on peri-implant osteogenesis: a histologic and histomorphometric study. *Implant Dentistry*, 17(1):118–126.

Gjelsvik, A. (1973a). Bone remodeling and piezoelectricity — {I}. *Journal of Biomechanics*, 6(2):69–77.

Gjelsvik, A. (1973b). Bone remodeling and piezoelectricity — {II}. *Journal of Biomechanics*, 6(2):187–193.

Gross, D. and Williams, W. (1982). Streaming potential and the electromechanical response of physiologically-moist bone. *J Biomech*, 15(4):277–295.

Hansson, S. (2003). A conical implant–abutment interface at the level of the marginal bone improves the distribution of stresses in the supporting bone. *Clin Oral Implants Res*, 14:286–293.

Hart, R. T., D.-D. T. and Heiple, K. G. (1984). Mathematical modeling and numerical solutions for functionally dependent bone remodeling. *Calcified Tissue International*, 36(1):S104–S109.

Hegedus, D. H. and Cowin, S. C. (1975). Bone remodeling ii: small strain adaptive elasticity. *Journal of Elasticity*, 6(4):337–352.

Hernandez, C., Hazelwood, S., and Martin, R. (1999). The relationship between basic multicellular unit activation and origination in cancellous bone. *Bone*, 25(5):585 – 587.

Holzapfel, G. A. (2000). Nonlinear solid mechanics: A continuum approach for engineering. *Wiley*, 1 edition.

Huiskes, R., Weinans, H., Grootenboer, H., Dalstra, M., Fudala, B., and Slooff, T. (1967). Adaptive bone-remodeling theory applied to prosthetic-design analysis. *J Biomech.*, 20:1135–1150.

Hwang, K., Song, J., Jo, J., Yang, H., Park, Y., Ong, J., and Rawls, H. (2002). Effect of poling conditions on growth of calcium phosphate crystal in ferroelectric batio3 ceramics. *J Mater Sci Mater Med*, 13:133–138.

Ikeda, T. (1990). Fundamentals of piezoelectricity. *Oxford University Press*.

Jacobs, C. R., Simo, J. C., Beaupré, G. S., and Carter, D. R. (1997). Adaptive bone remodeling incorporating simultaneous density and anisotropy considerations. *J Biomech*, 30(6):603–613.

Jianqing, F., Huipin, Y., and Xingdong, Z. (1997). Promotion of osteogenesis by a piezoelectric biological ceramic. *Biomaterials*, 18:1531–1534.

Johnson, M., Chakkalakal, D., Harper, R., and Katz, J. (1982). Comparison of the electromechanical effects in wet and dry bone. *J Biomech*, 13:437–442.

Jähne, B. (2005). *Digitale Bildverarbeitung*. Springer.

Keyak, J. H. and Falkinstein, Y. (2003). Comparison of in situ and in vitro ct scan-based finite element model predictions of proximal femoral fracture load. *Med Eng Phys*, 25:781–787.

Kienapfel, H., Sprey, C., Wilke, A., and Griss, P. (1999). Implant fixation by bone ingrowth. *J Arthroplasty*, 14(3):355–368.

Krstin, N., Nackenhorst, U., and Lammering, R. (2000). Zur konstitutiven beschreibung des anisotropen beanspruchungsadaptiven knochenumbaus. *Technische Mechanik*, 20:31–40.

Kummer, B. (1972). Biomechanics of bone: Mechanical properties, functional structure, functional adaptation. *In Biomechanics: its Foundations and Objectives. Edited by Fung YC, Perrone N, Anliker M. Englewood Cliffs: Prentice-Hall;*, pages 237–272.

Linde, F., Nørgaard, P., Hvid, I., Odgaard, A., and Søballe, K. (1991). Mechanical properties of trabecular bone. dependency on strain rate. *J Biomech*, 24:803–809.

Lutz, A. and Nackenhorst, U. (2011). Numerical investigations on the osseointegration of uncemented endoprostheses based on bio-active interface theory. *Computational Mechanics*, 50(3):367–381.

Martin, R. (2007). Targeted bone remodeling involves {BMU} steering as well as activation. *Bone*, 40(6):1574 – 1580.

Maugin, G. A. (1988). Continuum mechanics of electromagnetic solids. *World Scientific*.

Meijer, H., Starmans, F., Steen, W., and Bosman, F. (1993). A three-dimensional, finite-element analysis of bone around dental implants in an edentulous human mandible. *Arch. Oral Biol.*, 38(6):491–496.

Merdji, A., Bachir Bouiadjra, B., Ould Chikh, B., Mootanah, R., Aminallah, L., and Serier, B. (2012). Stress distribution in dental prosthesis under an occlusal combined dynamic loading. *Materials and Design*, 36:705–7013.

Moreo, P., JM, G.-A., and Doblaré, M. (2009). Bone ingrowth on the surface of endosseous implants. part 1: Mathematical model. *J Theor Biol*, 260(1):1–12.

Moreo, P., Pérez, M., García-Aznar, J., and Doblaré, M. (2007). Modelling the mechanical behaviour of living bony interfaces. *Computer Methods in Applied Mechanics and Engineering*, 196(35-36):3300–3314.

Morgan, E. F., Bayraktar, H. H., and Keaveny, T. M. (2003). Trabecular bone modulus-density relationships depend on anatomic site. *J Biomech*, 36:897–904.

Mycielska, M. E. and Djamgoz, M. B. A. (2004). Cellular mechanisms of direct-current electric field effects: galvanotaxis and metastatic disease. *Journal of Cell Science*, 117(9):1631–1639.

Nackenhorst, U. (2006). Computational methods for studies on the biomechanics of bones. *Foundation of Civil and Environmental Engineering*, 7:251–271.

Olsson, A. (2005). Piezoelectric coatings on implants. *Diploma Work, Linköping University*.

Papavasiliou, G., Kamposiora, P., Bayne, S. C., and Felton, D. A. (1997). 3d-fea of osseointegration percentages and patterns on implant-bone interfacial stresses. *J Dent*, 25(6):485–491.

Park, J. B. and Kenner, C. H. (1975). Effect of electrical stimulation on the tensile strength of the porous implant and bone interface. *Biumat. Med. Dev. Artif. Org.*, 3(2):233–243.

Park, J. B., Young, S. ., Kenner, G. H., von Recum, A. F., Myers, B. R., R., R., and Moore (1978). Dental implant fixation by electrically mediated process. 11. tissue ingrowth. *Biomat. Med. Dev. Artif. Org.*, 6(4):291–303.

Pauwels, F. (1965). Gesammelte abhandlungen zur funktionellen anatomie des bewegungsapparates. *Springer*, pages 543–549.

Pilliar, R. M., Lee, J. M., and Maniatopoulos, C. (1986). Observations on the effect of movement on bone ingrowth into porous-surfaced implants. *Clin Orthop Relat Res*, (208):108–113.

Polimeni, G., Xiropaidis, A., and Wikesj, U. E. (2006). Biology and principles of periodontal wound healing/regeneration. *Periodontology 2000*, 41(1):30–47.

Qin, Q. H. and Ye, J. Q. (2004a). Thermoelectroelastic solutions for internal bone remodeling under axial and transverse loads. *International Journal of Solids and Structures*, 41(9):2447–2460.

Qin, Q. H. and Ye, J. Q. (2004b). Thermoelectroelastic solutions for internal bone remodeling under axial and transverse loads. *International Journal of Solids and Structures*, 41(9):2447–2460.

Qu, C., Qin, Q.-H., and Kang, Y. (2006). A hypothetical mechanism of bone remodeling and modeling under electromagnetic loads. *Biomaterials*, 27(21):4050–4057.

Qu, C.-Y. and Yu, S.-W. (2011). The damage and healing of bone in the disuse state under mechanical and electro-magnetic loadings. *Procedia Engineering*, 10:171 – 176. 11th International Conference on the Mechanical Behavior of Materials (ICM11).

Ramtani, S. (2008). Electro-mechanics of bone remodelling. *Internat. J. Engrg. Sci.*, 46(11):1173–1182.

Rangert, B., Krogh, P., Langer, B., and Roekel, N. (1995). Bending overload and implant fracture: a retrospective clinical analysis. *Int J Oral Maxillofac Implants*, 10:326–334.

Rebeca, M. F. (2010). Numerical analysis and simulations in bone remodeling models. *PHD Thesis*.

Rho, J. Y., Hobatho, M. C., and Ashman, R. B. (1995). Relations of mechanical properties to density and ct numbers in human bone. *Med Eng Phys*, 17:347–355.

Rho, J.-Y., Kuhn-Spearing, L., and Zioupos, P. (1998). Mechanical properties and the hierarchical structure of bone. *Medical Engineering and Physics*, 20(2):92 – 102.

Richter, E. (1998). In vivo horizontal bending moments on implants. *Int J Oral Maxillofac Implants*, 13(2):232–44.

Ronold, H. J., Lyngstadaas, S. P., and Ellingsen, J. E. (2003). Analysing the optimal value for titanium implant roughness in bone attachment using a tensile test. *Biomaterials*, 24(25):4559–4564.

Rungsiyakull, C., Li, Q., Sun, G., Li, W., and Swain, M. V. (2010). Surface morphology optimization for osseointegration of coated implants. *Biomaterials*, 31(27):7196–7204.

Salman, N. N., Park, J. B., Kenner, G. H., F., A., and von Recum (1978). Electrical stimulation on bone growth into porous metal. *31st ACEMB*, page 21–25.

Salzstein, R. and Pollack, S. (1987). Electromechanical potentials in cortical bone—ii. experimental analysis. *Journal of Biomechanics*, 20(3):271 – 280.

Shayesteh, Y., Eslami, B., Dehghan, M., Vaziri, H., Alikhassi, M., Mangoli, A., and Khojasteh, A. (2007). The effect of a constant electrical field on osseointegration after immediate implantation in dog mandibles: a preliminary study. *Journal of Prosthodontics*, 16(5):337–342.

Shore, M. E., Xu, M.-q., Shah, B. P., Janoff, B. H., Hahn, V. G., Deardorff, A. M., Sovinsky, L., Spinner, B. N., Zasloff, A. M., Wozney, M. J., and Kaplan, S. F. (1998). The human bone morphogenetic protein 4 (bmp-4) gene: Molecular structure and transcriptional regulation. *Calcified Tissue International*, 63(3):221–229.

Sierpowska, J., Hakulinen, M., Töyräs, J., Day, J., Weinans, H., Jurvelin, J., and Lappalainen, R. (2005). Prediction of mechanical properties of human trabecular bone by electrical measurements. *Physiol Meas*, 26(2):S119–31.

Sierpowska, J., Tyrs, J., Hakulinen, M., Saarakkala, S., Jurvelin, J., and Lappalainen, R. (2003). Electrical and dielectric properties of bovine trabecular bone - relationships with mechanical properties and mineral density. *Physics in Medicine and Biology*, 48(6):775–786.

Singh, S. and Saha, S. (1984). Electrical properties of bone. a review. *Clin Orthop Relat Res*, (186):249–71.

Snyder, S. M. and Schneider, E. (1991). Estimation of mechanical properties of cortical bone by computed tomography. *J Orthop Res*, 9:422–431.

Song, J., Cho, T., Pan, H., Song, Y., Kim, I., and Lee, T. (2009). An electronic device for accelerating bone formation in tissues surrounding a dental implant. *Bioelectromagnetics*, 30:374–384.

Szmukler-Moncler, S., Salama, H., Reingewirtz, Y., and Dubruille, J. H. (1998). Timing of loading and effect of micromotion on bone-dental implant interface: review of experimental literature. *J Biomed Mater Res*, 43(2):192–203.

Theodore, L. (1968). A possible mechanism for the effect of electrical potentials on apatite formation in bone*. *Clinical Orthopaedics and Related Research*, 56:261–274.

Trindade, M. and Ohayon, R. (1999). New shear actuated smart structure beam finite element. *Computers and Structures*, 37:378–383.

Truesdell, C. and Noll, W. (1960). The nonlinear field theories of mechanics. *Springer*.

Wang, Z., Clark, C., and Brighton, C. (2001). Up-regulation of bone morphogenetic proteins in cultured murine bone cells with use of specific electric fields. *Bone Joint Surg Am*, 88:1053–1065.

Weinans, H., Huiskes, R., and Grootenboer, H. J. (1992). The behavior of adaptive bone-remodeling simulation models. *J Biomech*, 25(12):1425–1441.

Weinstein, A. M., Klawitter, J. J., Cleveland, T. W., and Amoss, D. C. (1976). Electrical stimulation of bone growth into porous al2o3. *J. Biomed. Muter. Res.*, 10:231–247.

Wirtz, D. C., Schiffers, N., Pandorf, T., Radermacher, K., Weichert, D., and Forst, R. (2000). Critical evaluation of known bone material properties to realize anisotropic fe-simulation of the proximal femur. *J Biomech*, 33(10):1325–1330.

Wolff, J. (1892). *Das Gesetz der Transformation der Knochen*. Berlin.

Wriggers, P. (2009). *Nonlinear Finite Element Methods*. Springer, Berlin.

Yang, J. (2005a). *An introduction to the theory of piezoelectricity*. New York : Springer.

Yang, J. (2005b). An introduction to the theory of piezoelectricity. *Advances in Mechanics and Mathematics*, 9.

Yonemori, K., Matsunaga, S., Ishidou, Y., Maeda, S., and Yoshida, H. (1996). Early effects of electrical stimulation on osteogenesis. *Bone*, 19(2):173 – 180.

Zienkiewicz, O., Taylor, R., and Zhu, J. (2005). *Finite Element Method - Its Basis and Fundamentals*. Butterworth Heinemann.

Curriculum Vitae

Personal Information

Name: Seyedalireza Shirazibeheshtiha

Date of birth: 08.08.1984

Place of birth: Tehran, Iran

Address: Süntelstr. 11, 30419 Hannover, Germany

Mobile: +491779633019

E-mail: shirazibeheshtiha@mario.uni-hannover.de

Education

01/2004–06/2008	Bachelor of Science in Mechanical Engineering, Semnan University, Semnan, Iran.
09/2008–09/2011	Master of Science in Mechanical Engineering, Bu-Ali Sina University, Hamedan, Iran.

Professional Experience

08/2013–present	Research Assistant at Institute of Mechanics and Computational Mechanics, Leibniz Universität Hannover, Germany

Awards and Achievements

04/2013-06/2016	Full scholarship of MARIO Doctoral Program, Leibniz University of Hanover.

February 23, 2017

Forschungs- und Seminarberichte

Institut für Baumechanik und Numerische Mechanik
Gottfried Wilhelm Leibniz Universität Hannover

Bisher in dieser Schriftenreihe erschienene Berichte:

S 73/1	Seminar über Thermodynamik und Kontinuumsmechanik, Hannover 1973
F 75/1	"Die Spannungsberechnung im Rahmen der Finite–Element–Methode", R. Ahmad, Dissertation, April 1975
F 76/1	"Zur Theorie und Anwendung der Stoffgleichungen elastisch–plastisch–viskoser Werkstoffe", H. Mentlein, Dissertation, April 1976
F 77/1	Seminar über lineare und geometrisch nichtlineare Schalentheorie einschließlich Stabilitätstheorie, Hannover 1978
F 77/2	"Beitrag zur Berechnung von Gründungsplatten mit Hilfe der Finite–Element–Methode", H. Meyer, Dissertation, Juli 1977
F 77/3	"Zur Berechnung der Eigenfrequenzen und Eigenschwingungsformen räumlich vorgekrümmter und vorverwundener Stäbe" J. Möhlenkamp, Dissertation, Dezember 1977
F 77/4	"Zur Theorie und Berechnung geometrisch und physikalisch nichtlinearer Kontinua mit Anwendung der Methode der finiten Elemente", J. Paulun, Dissertation, Dezember 1977
F 78/1	2. Seminar über Thermodynamik und Kontinuumsmechanik, Hannover 1978
F 79/1	"Theoretische und numerische Behandlung geometrisch nichtlinearer viskoplastischer Kontinua", K.–D. Klee, Dissertation, Februar 1979
F 79/2	"Zur Konstruierbarkeit von Variationsfunktionalen für nichtlineare Probleme der Kontinuumsmechanik", J. Siefer, Dissertation, Oktober 1979

F 80/1 “Theoretische und numerische Behandlung gerader Stäbe mit endlichen Drehungen",
M. Kessel, Dissertation, Februar 1980

F 81/1 “Zur Berechnung von Kontakt– und Stoßproblemen elastischer Körper mit Hilfe der Finite–Element–Methode",
P. Wriggers, Dissertation, Januar 1981

F 81/2 “Stoffgleichungen für Steinsalze unter mechanischer und thermischer Beanspruchung",
J. Olschewski, E. Stein, W. Wagner, D. Wetjen, geänderte Fassung eines Zwischenberichtes zum BMFT–Forschungsvorhaben KWA 1608/5

F 82/1 “Konvergenz und Fehlerabschätzung bei der Methode der Finiten Elemente",
R. Rohrbach, E. Stein, Abschlußbericht eines VW–Forschungsvorhabens, Februar 1982

F 82/2 “Alternative Spannungsberechnung in Finite–Element–Verschiebungsmodellen",
C. Klöhn, Dissertation, November 1982

F 83/1 Seminar über nichtlineare Stabtheorie,
Hannover 1983

F 83/2 “Beiträge zur nichtlinearen Theorie und inkrementellen Finite–Element–Berechnung dünner elastischer Schalen",
A. Berg, Dissertation, Juli 1983

F 83/3 “Elastoplastische Plattenbiegung bei kleinen Verzerrungen und großen Drehungen",
J. Paulun, Habilitation, September 1983

F 83/4 “Geometrisch nichtlineare FE–Berechnung von Faltwerken mit plastisch / viskoplastischem Deformationsverhalten",
M. Krog, Dissertation, Dezember 1983

F 85/1 Verleihung der Ehrendoktorwürde des Fachbereichs Bauingenieur– und Vermessungswesen der Universität Hannover an die Herren Prof. Dr. Drs. h.c. J.H. Argyris, Dr.–Ing. H. Wittmeyer

F 85/2 “Eine geometrisch nichtlineare Theorie schubelastischer Schalen mit Anwendung auf Finite–Element–Berechnungen von Durchschlag– und Kontaktproblemen",
W. Wagner, Dissertation, März 1985

F 85/3 “Geometrisch/physikalisch nichtlineare Probleme – Struktur und Algorithmen – ",
GAMM–Seminar im Februar 1985 in Hannover

F 87/1 “Finite–Elemente-Berechnungen ebener Stabtragwerke mit Fließgelenken und großen Verschiebungen",
R. Kahn, Dissertation, Oktober 1987

F 88/1 “Theorie und Numerik schubelastischer Schalen mit endlichen Drehungen unter Verwendung der Biot–Spannungen",
F. Gruttmann, Dissertation, Juni 1988

F 88/2 “Optimale Formgebung von Stabtragwerken mit Nichtlinearitäten in der Zielfunktion und in den Restriktionen unter Verwendung der Finite–Element–Methode",
V. Berkhahn, Dissertation, Oktober 1988

F 88/3 “Beiträge zur Theorie und Numerik großer plastischer und kleiner elastischer Deformationen mit Schädigungseinfluß",
R. Lammering, Dissertation, November 1988

F 88/4 “Konsistente Linearisierungen in der Kontinuumsmechanik und ihrer Anwendung auf die Finite–Elemente–Methode",
P. Wriggers, Habilitation, November 1988

F 88/5 “Mathematische Formulierung und numerische Methoden für Kontaktprobleme auf der Grundlage von Extremalprinzipien",
D. Bischoff, Habilitation, Dezember 1988

F 88/6 “Zur numerischen Behandlung thermomechanischer Prozesse",
C. Miehe, Dissertation, Dezember 1988

F 89/1 “Zur Stabilität und Konvergenz gemischter finiter Elemente in der linearen Elastizitätstheorie",
R. Rolfes, Dissertation, Juni 1989

F 89/2 “Traglastberechnungen von Faltwerken mit elastoplastischen Deformationen",
K.–H. Lambertz, Dissertation, November 1989

F 89/3 “Transientes Kriechen und Kriechbruch im Steinsalz",
U. Heemann, Dissertation, November 1989

F 89/4 “Materialgesetze zum Verhalten von Betonkonstruktionen bei harten Stößen",
E. Stein, P. Wriggers, T. Vu Van & T. Wedemeier, Dezember 1989

F 89/5 “Lineare Konstruktion und Anwendungen von Begleitmatrizen",
C. Carstensen, Dissertation, Dezember 1989

F 90/1 “Zur Berechnung prismatischer Stahlbetonbalken mit verschiedenen Querschnittformen für allgemeine Beanspruchungen",
H. N. Lucero–Cimas, Dissertation, April 1990

F 90/2 “Zur Behandlung von Stoß– Kontaktproblemen mit Reibung unter Verwendung der Finite–Element–Methode",
T. Vu Van, Dissertation, Juni 1990

F 90/3 “Netzadaption und Mehrgitterverfahren für die numerische Behandlung von Faltwerken",
L. Plank, Dissertation, September 1990

F 90/4 “Beiträge zur Theorie und Numerik finiter inelastischer Deformationen",
N. Müller–Hoeppe, Dissertation, Oktober 1990

F 90/5 “Beiträge zur Theorie und Numerik von Materialien mit innerer Reibung am Beispiel des Werkstoffes Beton",
T. Wedemeier, Dissertation, Oktober 1990

F 91/1 “Zur Behandlung von Stabilitätsproblemen der Elastostatik mit der Methode der Finiten Elemente",
W. Wagner, Habilitation, April 1991

F 91/2 “Mehrgitterverfahren und Netzadaption für lineare und nichtlineare statische Finite–Elemente–Berechnungen von Flächentragwerken",
W. Rust, Dissertation, Oktober 1991

F 91/3 “Finite Elemente Formulierung im Trefftzschen Sinne für dreidimensionale anisotrop–elastische Faserverbundstrukturen",
K. Peters, Dissertation, Dezember 1991

F 92/1 “Einspielen und dessen numerische Behandlung von Flächentragwerken aus ideal plastischem bzw. kinematisch verfestigendem Material",
G. Zhang, Dissertation, Februar 1992

F 92/2 “Strukturoptimierung stabilitätsgefährdeter Systeme mittels analytischer Gradientenermittlung",
A. Becker, Dissertation, April 1992

F 92/3 “Duale Methoden für nichtlineare Optimierungsprobleme in der Strukturmechanik",
R. Mahnken, Dissertation, April 1992

F 93/1 “Kanonische Modelle multiplikativer Elasto–Plastizität. Thermodynamische Formulierung und numerische Implementation",
C. Miehe, Habilitation, Dezember 1993

F 93/2 “Theorie und Numerik zur Berechnung und Optimierung von Strukturen aus isotropen, hyperelastischen Materialien",
F.–J. Barthold, Dissertation, Dezember 1993

F 94/1 “Adaptive Verfeinerung von Finite–Element–Netzen für Stabilitätsprobleme von Fläschentragwerken",
E. Stein, B. Seifert, W. Rust, Forschungsbericht, Oktober 1994

F 95/1 “Adaptive Verfahren für die Formoptimierung von Flächentragwerken unter Berücksichtigung der CAD–FEM–Kopplung",
A. Falk, Dissertation, Juni 1995

F 96/1 “Theorie und Numerik dünnwandiger Faserverbundstrukturen",
F. Gruttmann, Habilitation, Januar 1996

F 96/2 “Zur Theorie und Numerik finiter elastoplastischer Deformationen von Schalenstrukturen",
B. Seifert, Dissertation, März 1996

F 96/3 “Theoretische und algorithmische Konzepte zur phänomenologischen Beschreibung anisotropen Materialverhaltens",
J. Schröder, Dissertation, März 1996

F 96/4 “Statische und dynamische Berechnungen von Schalen endlicher elastischer Deformationen mit gemischten finiten Elementen",
P. Betsch, Dissertation, März 1996

F 96/5 “Kopplung von Finiten Elementen und Randelementen für ebene Elastoplastizität mit Impelementierung auf Parallelrechnern",
M. Kreienmeyer, Dissertation, März 1996

F 96/6 “Theorie und Numerik dimensions– und modeladaptiver Finite–Elemente–Methoden von Fläschentragwerken",
S. Ohnimus, Dissertation, Juni 1996

F 96/7 “Adaptive Finite Elemente Methoden für MIMD-Parallelrechner zur Behandlung von Strukturproblemen mit Anwendung auf Stabilitätsprobleme",
O. Klaas, Dissertation, Juli 1996

F 96/8 “Institutsbericht 1971–1996 aus Anlaß des 25–jährigen Dienstjubiläums von Prof. Dr.–Ing. Dr.–Ing. E.h. Dr. h.c. mult. Erwin Stein",
Dezember 1996

F 97/1 “Modellierung und Numerik duktiler kristalliner Werkstoffe",
P. Steinmann, Habilitation, August 1997

F 97/2 “Formoptimierung in der Strukturdynamik",
L. Meyer, Dissertation, September 1997

F 97/3 “Modellbildung und Numerik für Versagensprozesse in Gründungen von Caisonwellenbrechern",
M. Lengnick, Dissertation, November 1997

F 98/1 “Adaptive gemischte finite Elemente in der nichtlinearen Elastostatik und deren Kopplung mit Randelementen",
U. Brink, Dissertation, Februar 1998

F 98/2 “Theoretische und numerische Aspekte zur Parameteridentifikation und Modellierung bei metallischen Werkstoffen",
R. Mahnken, Habilitation, Juli 1998

F 98/3 “Lokalisierung und Stabilität der Deformation wassergesättigter bindiger und granularer Böden",
J. M. Panesso, Dissertation, August 1998

F 98/4 “Theoretische und numerische Methoden in der angewandten Mechanik mit Praxisbeispielen",
R. Mahnken (Hrsg.), Festschrift anlässlich der Emeritierung von Prof. Dr.–Ing. Dr.–Ing. E.h. h.c. mult. Erwin Stein, November 1998

F 99/1 “Eine h–adaptive Finite–Element–Methode für elasto–plastische Schalenproblem in unilateralem Kontakt",
C.–S. Han, Dissertation, Juli 1999

F 00/1 “Ein diskontinuierliches Finite–Element-Modell für Lokalisierungsversagen in metallischen und granularen Materialien",
C. Leppin, Dissertation, März 2000

F 00/2 “Untersuchungen von Strömungen in zeitlich veränderlichen Gebieten mit der Methode der Finiten Elementen",
H. Braess, Dissertation, März 2000

F 00/3 “Theoretische und algorithmische Beiträge zur Berechnung von Faserverbundschalen",
J. Tessmer, Dissertation, März 2000

F 00/4 “Theorie und Finite–Element–Methode für die Schädigungsbeschreibung in Beton und Stahlbeton",
D. Tikhomirov, Dissertation, August 2000

F 01/1 “A C1 - continuous formulation for finite deformation contact",
L. Krstulovic–Opara, Dissertation, Januar 2001

F 01/2 “Strain Localisation Analysis for Fully and Partially Saturated Geomaterials",
H. Zhang, Dissertation, Januar 2001

F 01/3 “Meso–makromechanische Modellierung von Faserverbundwerkstoffen mit Schädigung",
C. Döbert, Dissertation, April 2001

F 01/4 “Thermomechanische Modellierung gummiartiger Polymerstrukturen",
S. Reese, Habilitation, April 2001

F 01/5 “Thermomechanisches Verhalten von Gummimaterialien während der Vulkanisation – Theorie und Numerik –",
M. André, Dissertation, April 2001

F 01/6 “Adaptive FEM für elastoplastische Deformationen – Algorithmen und Visualisierung",
M. Schmidt, Dissertation, Juni 2001

F 01/7 “Verteilte Algorithmen für h–, p– und d–adaptive Berechnungen in der nichtlinearen Strukturmechanik",
R. Niekamp, Dissertation, Juni 2001

F 01/8 “Theorie und Numerik zur Berechnung und Optimierung von Strukturen mit elastoplastischen Deformationen",
K. Wiechmann, Dissertation, Juli 2001

F 01/9 “Direct Computation of Instability Points with Inequality using the Finite Element Method",
H. Tschöpe, Dissertation, September 2001

F 01/10 “Theorie und Numerik residualer Fehlerschätzer für die Finite–Elemente–Methode unter Verwendung äquilibrierter Randspannungen",
S. Ohnimus, Habilitation, September 2001

F 02/1 “Adaptive Algorithmen für thermo–mechanisch gekoppelte Kontaktprobleme",
A. Rieger, Dissertation, August 2002

F 02/2 “Consistent coupling of shell– and beam–models for thermo–elastic problems",
K. Chavan, Dissertation, September 2002

F 03/1 “Error–controlled adaptive finite element methods in large strain hyperelasticity and fracture mechanics",
M. Rüter, Dissertation, Mai 2003

F 03/2 “Formulierung und Simulation der Kontaktvorgänge in der Baugrund–Tragwerks–Interaktion",
A. Haraldsson, Dissertation, Juni 2003

F 03/3 “Concepts for Nonlinear Orthotropic Material Modeling with Applications to Membrane Structures",
T. Raible, Dissertation, Juni 2003

F 04/1 “On Single– and Multi–Material arbitrary Lagrangian–Eulerian Approaches with Application to Micromechanical Problems at Finite Deformations",
D. Freßmann, Dissertation, Oktober 2004

F 04/2 “Computational Homogenization of Microheterogeneous Materials at Finite Strains Including Damage",
S. Löhnert, Dissertation, Oktober 2004

F 05/01 “Numerical Micro–Meso Modeling of Mechanosensation driven Osteonal Remodeling in Cortical Bone",
C. Lenz, Dissertation, Juli 2005

F 05/02 “Mortar Type Methods Applied to Nonlinear Contact Mechanics",
K.A. Fischer, Dissertation, Juli 2005

F 05/3 “Models, Algorithms and Software Concepts for Contact and Fragmentation in Computational Solid Mechanics",
C. Hahn, Dissertation, November 2005

F 06/1 “Computational Homogenization of Concrete",
S. Moftah, Dissertation, Januar 2006

F 06/2 Reduction Methods in Finite Element Analysis of Nonlinear Structural Dynamics",
H. Spiess, Dissertation, Februar 2006

F 06/3 “Theoretische und algorithmische Konzepte zur Beschreibung des beanspruchungsadaptiven Knochenwachstums",
B. Ebbecke, Dissertation, März 2006

F 06/4 “Experimentelle Untersuchungen an elastomeren Werkstoffen",
M. Dämgen, Dissertation, Dezember 2006

F 07/1 “Numerische Konzepte zur Behandlung inelastischer Effekte beim reibungsbehafteten Rollkontakt",
M. Ziefle, Dissertation, Februar 2007

F 07/2 “Begleitbuch zur Leibniz–Ausstellung",
Hrsg: E. Stein, P. Wriggers, 2007

F 07/3 “Modellierung und Simulation der hochfrequenten Dynamik rollender Reifen",
M. Brinkmeier, Dissertation, Juni 2007

F 07/4 “Computational Homogenization of micro–structural Damage due to Frost in Hardened Cement Paste",
M. Hain, Dissertation, Juli 2007

F 07/5 “Elektromechanisch gekoppelte Kontaktmodellierung auf Mikroebene",
T. Helmich, Dissertation, August 2007

F 07/6 “Dreidimensionales Diskretes Elemente Modell für Superellipsoide",
C. Lillie, Dissertation, Oktober 2007

F 07/7 “Adaptive Methods for Continuous and Discontinuous Damage Modeling in Fracturing Solids",
S.H. Reese, Dissertation, Oktober 2007

F 08/1 “Student Projects of Micromechanics",
Hrsg: U. Nackenhorst, August 2008

F 09/1 “Theory and Computation of Mono– and Poly– crystalline Cyclic Martensitic Phase Transformations",
G. Sagar, Dissertation, August 2009

F 09/2 “Student projects of Micromechanics",
D. Balzani and U. Nackenhorst, Course Volume, Oktober 2009

F 09/3 “Multiscale Coupling based on the Quasicontinuum Framework, with Application to Contact Problems",
W. Shan, Dissertation, November 2009

F 10/1 “A Multiscale Computational Approach for Microcrack Evolution in Cortical Bone and Related Mechanical Stimulation of Bone Cells",
D. Kardas, Dissertation, September 2010

F 12/1 “Ein physikalisch motiviertes Reifen–Fahrbahnmodell für die Gesamtfahrzeugsimulation",
R. Chiarello, Dissertation, Februar 2012

F 13/1 “Thermomechanical Analysis of Tire Rubber Compounds in Rolling Contact",
A. Suwannachit, Dissertation, September 2012

F 13/2 “Towards a Finite Element Model for Fluid Flow in the Human Hip Joint",
K. Fietz, Dissertation, September 2013

F 14/1 “Micro-Mechanically Based Damage Analysis of Ultra High Performance Fibre Reinforced Concrete Structures with Uncertainties",
A. Hürkamp, Dissertation, Dezember 2013

F 14/2 “Numerical Solution of High–Dimensional Fokker–Planck Equations with Discontinuous Galerkin Methods",
F. Loerke, Dissertation, Dezember 2013

F 14/3 “Numerische Simulation probabilistischer Schädigungsmodelle mit der Stochastischen Finite Elemente Methode",
P. Jablonski, Dissertation, September 2014

F 15/1 “On a Finite Element Approach for the Solution of a Mechanically Stimulated Biochemical Fracture Healing Model",
A. Sapotnick, Dissertation, November 2015.

F 15/2 “Simulation of Elastic-Plastic Material Behaviour with Uncertain Material Parameters. A Spectral Stochastic Finite Element Method Approach",
S. Fink, Dissertation, November 2015.

F 15/3 “A Fully Micro-mechanically Motivated Material Law for Filled Elastomer”,
O. Stegen, Dissertation, Februar 2016.

F 16/1 “A Modified Adaptive Harmony Search Algorithm Approach on Structural Identification and Damage Detection”,
M. Jahjouh, Dissertation, March 2016.